Structural Explorations into Singlet Fission Chromophores for Solar Photochemistry with Femtosecond Stimulated Raman Spectroscopy

A THESIS

SUBMITTED TO THE FACULTY OF THE

UNIVERSITY OF MINNESOTA

BY

Kajari Bera

IN PARTIAL FULFILLMENT OF THE REQUIREMENTS

FOR THE DEGREE OF

DOCTOR OF PHILOSOPHY

Advisor: Renee R. Frontiera

October, 2020

Acknowledgements

THANK YOU

- Those two words probably are not enough to express how grateful I am to all those around me who have helped me to reach where I am at present both personally and professionally. I hope I have been able to make you all know your importance in my life and how much I treasure you all.

First and foremost, I want to express my sincere gratitude to my advisor Prof. Renee Frontiera for providing me the opportunity to work on a project that aligned with my interests. Renee, I am so grateful to you for choosing me as one of your prospective grad students out of many, back in 2015. I have learnt so much from our one-to-one discussions. I have always looked up to you for stimulating my (and others) scientific knowledge. Your guidance and the liberty to work on my own terms have helped me enrich my experiences and expertise. Thank you for believing me with rubrene, which opened the door for me to have such a satisfactory scientific journey during my PhD progress. Thank you for your trust in me and your constant guidance and encouragement throughout this journey.

I want to thank my thesis committee members, Prof. Ken Leopold, Prof.

David Blank and Prof. Russell Holmes for agreeing to serve on my committee and guiding me whenever needed in the past years. I would like to extend my thanks to Prof. Christopher Douglas for the collaboration and the enlightening exchanges on spectroscopy and synthetic chemistry. I would like to take this opportunity to thank all the teachers and mentors I had in the past starting from my elementary school for their support, motivation, teachings and advises to instill the love and passion of science in me.

My group, the entire incredibly awesome Frontiera clan, past and present. I am thankful to those before me who laid up the groundwork of setting up the lab and then transferring their knowledge for me to add to that, as small as that might have been. Those five years have been filled with constant inspiration, motivation and kindness from you all. I will always cherish the endless talks and discussions with all of you when we were physically in lab together. The desserts from our bakers, doughnuts on my desk by my secret saviors, jenga, game-nights and all the teasing I have received from you all have made this journey extraordinary. This cannot pass by without mentioning how much I adore you all for staying connected during this pandemic and supporting each other. I am really grateful to the friendships that I have made in the lab and hope to carry them along forever.

To all my friends, from here and worldwide. This long journey has definitely been enjoyable due to the constant presence of all my friends. The late-night phone-calls, nationwide and overseas, are truly memorable, and have helped me to keep going. Siu, thank you for not only sharing your birthday with me but also being the best lab member whom I could depend on reliably without a second

thought and always being there to listen to my banters. Adeline, you are always my go-to-person for all kinds of situations. All the memories we made during our innumerable walks and hikes are very fond to me. Avik, Irfana & Neha, although you have been far geographically, but never from my mind. Thank you for always enlightening me with all the random things. Your presence has made my journey smooth.

I want to acknowledge mom, dad and my brother, Saikat for their unconditional love and support. Thank you *ma* and *papa* for being the strong pillars that I could lean upon throughout my life. I hope to keep making you both proud of me, now and in future. *Bhai*, no matter how much you annoy me, you will always be my sweet little brother whom I will reprimand for eating outside. I want to thank my extended family members who have supported me throughout my journey of life. Last but certainly not the least, I want to thank my new husband Amartya. Thank you for your endless love and belief in me during this journey and keeping my madness in check with your soberness. I am so happy having to spend my life with you and for the new addition of loving mom and dad-in-law, to my family. I love you all equally.

I am wrapping up my thesis at a time when we are surrounded by the COVID-19 pandemic and do not know how the world is going to look in the future. Our willingness to stay and support each other makes me hopeful that just like life, we will always find light after the darkest of times. - Love, Kajari!

Dedication

This thesis is dedicated to my dad and mom, Swapan K. Bera and Barnali Bera, for being my inspiration to pursue a doctoral degree. This is for both of you!

Abstract

Understanding physical, chemical or biological changes require monitoring the molecular vibrations aka nuclear coordinates on the timescale of their movements, which is hundreds of femtoseconds. Thus, ultrafast spectroscopic techniques capable of providing molecular conformational changes on the femtosecond timescale are desirable to provide in-depth knowledge of any photophysical process. This thesis discusses the strength of using a structurally sensitive ultrafast spectroscopic technique, femtosecond stimulated Raman spectroscopy (FSRS) to understand the photophysics in a chemical process called singlet fission.

Thin films and single crystals which may undergo singlet fission are promising for solar energy conversion strategies as they can generate two charge carriers by the absorption of only one photon. A major bottleneck in the singlet fission field is the challenge of designing or discovering new molecules with enhanced photophysical properties, while not altering other parameters such as crystal packing or solubility which can hinder overall device performance. Chemical modifications to acenes may lead to singlet fission-based photovoltaics with improved solar energy conversion efficiencies, but identifying how molecular structural changes impact the rate and yield of fission is challenging to model and predict. Traditionally, spectroscopic measurements have not provided much insight for rational design of new chromophores, but rather have been used to understand why an existing system works well. To this end, I have used FSRS to examine the excited state structural dynamics in organic chromophores undergoing singlet fission and have

provided a predictive model for molecular designing guidelines to obtain efficient singlet fission systems for their use in solar energy based devices.

Specifically, I have used ultrafast FSRS to monitor the changes in the molecular structure in rubrene during singlet fission and observed that singlet fission in crystalline rubrene is associated with a loss of electron density in the tetracene backbone. Armed with this knowledge and a hypothesis to improve singlet fission rate by reducing electron density in the tetracene core, I screened rubrene derivatives to study their excited state dynamics using FSRS. From a series of derivatives, I screened two new rubrene derivatives with electron withdrawing substituents, FM-rubrene & F-rubrene, to prime the system for singlet fission, without impacting intermolecular interactions. Using these rationally designed rubrene derivatives I found that both the rate and yield of singlet fission are significantly improved, proving that spectroscopic insight is crucial to successfully designing new chromophores. This shows that the long-held promise of spectroscopy-informed small molecule design for organic optoelectronic materials can be realized in rubrene-based singlet fission materials.

As the first graduate student to use FSRS in a microscope to look at crystals, I realized that distinguishing Raman from non-Raman features can be complicated in molecular crystals, where the narrowband transient vibronic couplings due to less heterogeneous broadening can overwhelm the excited state Raman bands. To overcome this, we redesigned the ultrafast FSRS experimental setup to help ease the data extraction and interpretation associated with this technique. By adding a pair of mirrors and a slit to the existing grating filter setup, we generated an additional Raman excitation pulse that identifies Raman peaks from a pool of

non-Raman peaks.

In this thesis, I present the successful implementation of FSRS to provide unprecedented structural dynamics in organic semiconducting materials with the aim to achieve better performing singlet fission based-photovoltaic devices and the experimental modifications made to support FSRS as a more user-friendly technique for its widespread adoption to understand chemical reactions.

Contents

List of Tables

List of Figures

List of Abbreviations

FSRS	Femtosecond stimulated Raman spectroscopy
SF	Singlet fission
COORS	Common old ordinary Raman spectroscopy
IR	Infrared
RR	Resonance Raman
ISRS	Impulsive stimulated Raman spectroscopy
TR-PL	Time-resolved photoluminescence
TR-2PPE	Time-resolved two-photon photoemission
TR-EPR	Time-resolved electron paramagnetic resonance
TAM	Transient absorption microscopy
SO-FSRS	Spatially offset FSRS
TDI	Terrylene-3,4:11,12-bis(dicarboximide)
PIA	Photoinduced absorption
ES	Electronic spectroscopy
NOPA	Non-collinear parametric amplifier
BBO	Beta barium borate
TA	Transient absorption

DFT	Density functional theory
NBO	Natural bond orbital
ESP	Electrostatic potential
HOMO	Highest occupied molecular orbital
SOMO	Singly occupied molecular orbital
SERDS	Shifted excitation Raman difference spectroscopy
VSFG	Vibrational sum frequency generation
DTTC	3,3′-diethylthiatricarbocyanine
HPLC	High Performance Liquid Chromatography
XRD	X-ray diffraction
DBIB	1,3-Diphenylisobenzofuran
FWHM	Full width at half maximum
PVT	Physical vapor transport

Chapter 1

Introduction

1.1 Motivation

The pursuit of new, efficient and diverse approaches to produce clean energy is becoming increasingly crucial as the global energy demand continues to increase. An integrated network of renewable energy sources (solar, wind, hydroelectric, geothermal etc.) and energy storage (fuels, batteries etc.) is necessary to deliver reliable and steady supply of energy to meet the global needs. According to the U.S. energy consumption estimations in 2019 by Lawrence Livermore national laboratory, the largest increases in energy supply came from wind and solar energy, with jumps of 10% and 8%, respectively for the second time in a row. Solar energy, estimated to supply annual energy of about four order of magnitudes more than the global energy demand in an entire year, thus is an enormous source of energy and possess great potential to harness in renewable energy technologies. Photovoltaic devices play an important role in power generation, and therefore, the efficiency of the solar energy conversion becomes important in the search for

commercially viable solar cells. However, the fundamental limit of the efficiency of a single junction photovoltaic device is $\sim 32\%$ due to various energy loss pathways, first laid out by Shockley and Quiesser in 1961, [1] and thus requires alternative strategies to identify materials and processes that can be used to overcome this limitation.

Singlet fission is a photophysical process where an absorption of a photon generates a pair of charge carriers on the ultrafast timescale of femto- to picoseconds. [2, 3] The generation of multiple charge carries at the expense of only one photon has potential to be used in photovoltaic and photocatalytic processes. Photovoltaic devices based on chromophores undergoing singlet fission in theory can increase the solar energy conversion efficiency in a single p-n junction solar cell from $\sim 32\%$ to $\sim 45\%$. However, the commercial solar cells based on singlet fission has displayed a conversion efficiency of only $\sim 5.1\%$, [4] which is far less than theoretically claimed. A major obstacle to the successful implementation is the lack of chromophores that can undergo efficient singlet fission while still being photo- and air-stable and solution processible. Chemical modifications to acenes could lead to singlet fission photovoltaics with long operating lifetimes but identifying how molecular structural changes impact the rate and yield of fission is challenging. This calls for an interest towards understanding the underlying mechanism of the singlet fission process on the ultrafast timescale with an aim to design new class of molecules to make singlet fission commercially viable. Therefore, to provide insights into the molecular changes during singlet fission needs the use of ultrafast techniques capable of monitoring the nuclear motions on the rapid timescale of femtoseconds.

Femtosecond stimulated Raman spectroscopy (FSRS) is a structurally sensitive ultrafast vibrational spectroscopic technique that can capture molecular snapshots to map out the evolution of the molecular structure over the course of the chemical reaction. [5] Since its first inception back in 1994, FSRS has evolved and has stood out as a strong ultrafast spectroscopic technique capable of providing vibrational and structural information with high spectral ($<$15 cm^{-1}) and temporal (sub-50 fs) resolution. FSRS has been previously used to provide structural insights during various ultrafast photophysical processes such as isomerization of rhodopsin for vision, excited state proton transfer in green fluorescent protein to list a few. As FSRS can monitor the molecular conformational changes on the ultrafast timescale of singlet fission process, it is a well-suited technique to study the photophysical process of singlet fission and provide essential information to modify the structural properties of chromophores to improve the commercialization of devices based on singlet fission.

1.2 Outline

This thesis focusses on the application of an ultrafast spectroscopic technique, femtosecond stimulated Raman spectroscopy, to provide unprecedented structural information during singlet fission. Additionally, this thesis demonstrates the advancement made to the experimental setup of FSRS to simplify the complex data interpretation associated with this ultrafast technique.

Chapter 2 provides a review of the importance and role of vibrational studies to understand the singlet fission process. It highlights the various experimental techniques that are commonly used to study singlet fission and then goes more

in-depth discussion about the unique contribution of infrared and Raman based spectroscopic techniques to the singlet fission community. Although vibrational spectroscopic techniques are still in their infancy to study singlet fission, this chapter provides a future direction for the application of vibrational spectroscopy in the field of singlet fission.

Chapter 3 describes the application of FSRS to study the structural changes in crystalline rubrene molecules during the ultrafast singlet fission process. This study reveals that the structure of the rubrene molecules changes such that the electron density moves away from the core of the molecule during the singlet fission process. The results suggest that the rubrene derivatives that have less electron density in its central core will facilitate the singlet fission process. This is an unique study that makes the path to formulate designing guidelines for efficient singlet fission process.

Chapter 4 demonstrates the long-held promise of using ultrafast spectroscopic technique to guide the designing principles for efficient singlet fission chromophores. This chapter describes the structural evolution in rubrene derivatives, FM-rubrene and F-rubrene, using FSRS and proves that the electron deficient rubrene derivatives undergoes an order of magnitude faster singlet fission than in rubrene. This novel study provides ultrafast spectroscopy assisted guidelines to chemically modify existing chromophores for the rational designing of singlet fission based devices, which goes beyond just the energetics criteria.

Chapter 5 is an instrument focused study to simplify the complexity of data interpretation associated with FSRS. Discerning Raman modes from a pool of

background in the FSR data is a challenge that has limited the widespread adoption of FSRS. This chapter describes how by adding just a pair of mirrors and a slit can result in generating excitation Raman pump pulse at two frequencies that simplifies to distinguish Raman from other non-Raman features in FSRS.

Chapter 6 discusses numerous future directions in regards to studying various physiochemical properties in organic molecular crystals using common old ordinary Raman spectroscopy (COORS) and FSRS. It describes utilizing low-frequency Raman modes to identify crystal structure within a series of chemically substituted molecules as highly pure phases and specific crystalline packing structures are usually desirable for high performing optoelectronic devices. Additionally, this chapter elaborates on new molecular systems to study the effect of polymorphism in deciding the fate of the initially photoexcited wavepacket for their use as singlet fission chromophores for device applications.

Chapter 2

Advancements in Singlet Fission Chromophore Design Enabled by Vibrational Spectroscopies

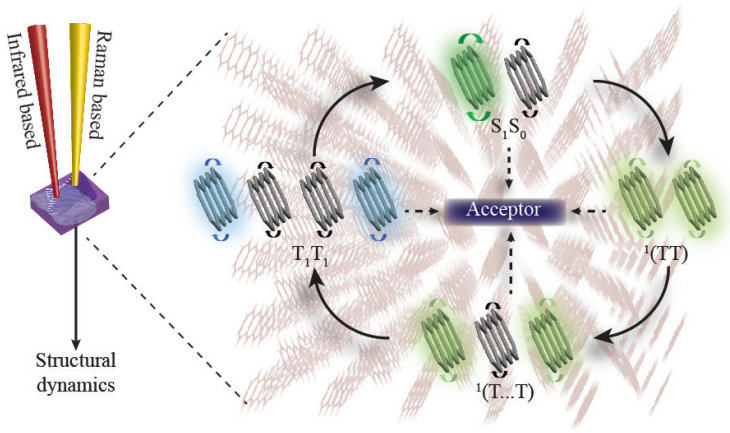

2.1 Overview

Singlet fission leads to the formation of two separate triplet T_1 excitons from an initial singlet S_1 exciton through ^{1}(TT) and ^{1}(T...T), multiexcitonic intermediates that retain singlet character. Its ability to achieve external quantum efficiencies higher than 100% made it an attractive candidate for optoelectronic device applications. However, singlet fission has not been applied widely despite having been investigated by a myriad of spectroscopic methods, in part due to our poor understanding on how to optimize molecular structure and packing in chromophores well-suited to large-scale production. Vibrational spectroscopies provide a solution because they directly probe nuclear motions, allowing us to monitor evolving structural changes in molecules undergoing singlet fission, thus providing us with roadmaps to design molecules suitable for optoelectronic applications. This chapter reviews the contributions and analyzes the future directions of vibrational spectroscopies to the advancement in our knowledge about the mechanisms and rational designing of chromophores undergoing efficient singlet fission.

2.2 Introduction

Singlet fission (SF), a photophysical process where an initially excited singlet state S_1 evolves into two low-lying triplet states T_1, has been shown to attain external quantum efficiencies higher than 100% in photovoltaic devices. [6] Although this phenomenon had first been observed in the early 1960's, [7,8] it only regained interest in the past decade after it was proven to overcome the Shockley-Queisser limit in 2006, [1, 9] showing promise for future applications in photovoltaics and

photocatalytic processes. However, working solar cells based on SF has delivered a maximum power conversion efficiency of only 5.1% as opposed to the theoretical limit of 45%. [4] Some challenges to improve efficiency include poor environmental stability and high energy losses during charge generation and transport in the currently known classes of SF chromophores. Therefore, we need rational designing principles to develop SF materials that are capable of achieving the power conversion efficiency much closer to the theoretical limit.

Following light absorption, SF is generally accepted as a three-step process which involves the formation of two intermediates:

$$S_0 + S_1 \leftrightarrow {}^1(TT) \rightarrow {}^1(T...T) \rightarrow T_1 + T_1 \tag{2.1}$$

where both ^{1}(TT) and ^{1}(T...T) are multiexcitonic intermediates that retain singlet character, making SF a spin-allowed process. The correlated triplet pair, ^{1}(TT), consists of two excited triplet states that are electronically coupled and spin correlated. When ^{1}(TT) loses its electronic coupling but still retains its spin coherence, it forms ^{1}(T...T), the separated correlated triplet pair. Eventually, ^{1}(T...T) loses its spin coherence to generate two individual triplet states T_1, which can be harvested for optoelectronic applications. The detailed mechanism of SF dynamics, and the electronic energetics and molecular packing and coupling requirements for chromophores to undergo efficient SF have been covered by many reviews over the past decade. [2, 3, 10–16]

The major hindrance to the optimization of SF based photovoltaics is the scarcity of known molecules undergoing efficient SF that are photochemically stable, solution processible and oriented in the correct geometries in their crystalline

forms. The most commonly studied SF chromophores are acenes and their derivatives, although carotenoids and polymers have also been investigated for their SF properties. [2] However, identifying new classes of molecules capable of undergoing SF is challenging in part due to the limited knowledge about material design principles, such as modifying existing molecules for desired crystal packing structure and ideal chemical substituents, for chromophores undergoing near unity SF efficiency. Additionally, the photophysics of SF mechanism is not fully understood and widely debated: whether the generation of ^{1}(TT) from S_1, follows a direct mechanism where the S_1 state couples with a neighboring S_0 state to directly form ^{1}(TT) with no observable intermediates, [17, 18] or a charge-transfer mediated mechanism where an observable charge-transfer intermediate is formed before it generates ^{1}(TT). [16, 19] Thus, the limited number of SF chromophores compounded with the complex convolution of the spin dynamics and the interactions between the electronic and vibrational states during SF, makes it difficult to achieve consensus on a generic SF theory and molecular design principles. A promising approach would be to determine how exactly nuclear coordinates impact the mechanism and yield of SF, and thus, vibrational spectroscopies which probe structural changes following light absorption are uniquely well-suited to lead to advances in the SF field. This chapter emphasizes the unique contributions and strengths of vibrational techniques to enhance our understanding of the designing principles for SF based chromophores.

Historically, SF has been examined through a combination of electronic, photoemission, magnetic and computational techniques. Ultrafast vibrational techniques are a relatively recent addition to the experimental toolbox for investigating

SF. Thus far, these techniques include time-resolved mid-infrared and infrared (IR) spectroscopy, resonance Raman (RR) spectroscopy, impulsive stimulated Raman spectroscopy (ISRS), and femtosecond stimulated Raman spectroscopy (FSRS). Since vibrational motions are determined by the interplay of the nuclear coordinates and are highly sensitive to local environments, vibrational spectral features, such as bandwidth, frequencies and intensity, evolve as the molecules transit from the S_0 state to S_1, ^{1}(TT), ^{1}(T...T) and T_1 states. This can give vibrational techniques an edge over electronic spectroscopies for studying SF because electronic features tend to be broad and overlapped due to the isoenergetic nature of the excitonic states and the existence of equilibrium between them. Time-resolved vibrational spectroscopies are particularly powerful tools to study photochemical and photophysical processes because they can directly determine the nuclear motions driving SF and hence provide unique information about the structure, dynamics and properties of short-lived species. A better understanding of the molecular structural changes will in turn guide the strategic design of SF materials for efficient photovoltaic systems.

In this chapter, we review the significant contributions of vibrational spectroscopies to our understanding of the SF process, with a focus on translating mechanistic insight into practical design considerations for new chromophores. We describe key examples from the literature, starting with acene studies using IR and mid-IR time-resolved spectroscopy, followed by detailing the importance and role of vibronic coherence in SF, and then moving through Raman based studies which helped in formulating design guidelines for efficient SF chromophores. We conclude with comments on promising future applications of vibrational spectroscopy

to guide SF materials design, including magneto-vibrational spectroscopies, terahertz approaches, and microscopic techniques to map vibrational contributions to exciton transport.

Before we detail the specific contributions vibrational spectroscopies have made in understanding SF, we briefly describe the key highlights from electronic, magnetic, and computational studies. Electronic spectroscopies such as time-resolved photoluminescence (TR-PL), transient absorption (TA), two-dimensional electronic spectroscopy (2DES) and time-resolved two-photon photoemission (TR-2PPE) have been used to study SF. TR-PL provides information about the bright states, [20] TA can probe both bright and dark states, [21–23] 2DES identifies quantum coherent superposition of electronic states and couplings [24] and TR-2PPE provides the energies of the excitonic states during the SF process. [25, 26] In addition to optical techniques, the magnetic field-based techniques, such as time-resolved electron paramagnetic resonance (TR-EPR) provide insights about the spin dephasing and the triplet and quintet states involved during SF. [27, 28] While each technique is specific in the information it can provide, all techniques complement each other and supports each other to unravel the complex and complicated view of the SF process.

In Figure 2.1, we summarized how each experimental technique has guided our knowledge about the mechanisms and energetics of each step in the SF process, from the generation of the ^{1}(TT) state to the harvesting of triplets. Step 1 refers

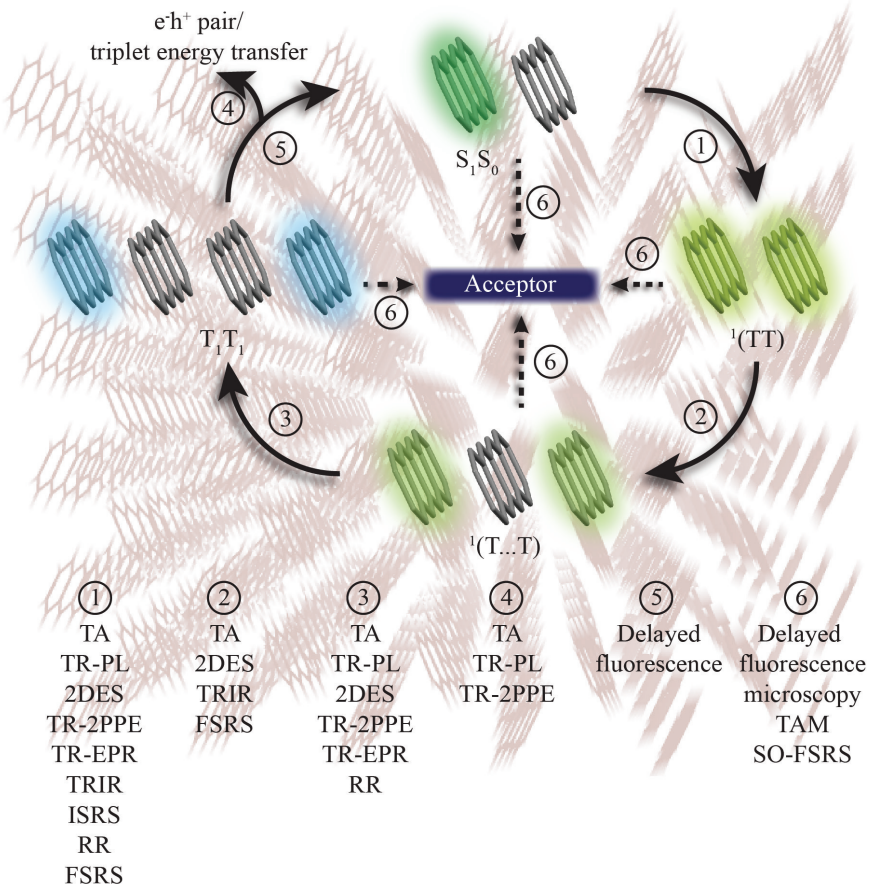

Figure 2.1: Schematic depicting SF & spectroscopic techniques that have been applied to understand corresponding steps in SF. 1) Formation of correlated triplet pair,^{1}(TT) that retains an overall singlet character. 2) Formation of the ^{1}(T...T) state after ^{1}(TT) loses its electronic coherence. 3) Formation of the individual triplet states after the ^{1}(T...T) loses its spin coherence. 4) Generation of free electron and hole charge carriers after the triplets are harvested at an acceptor substrate. 5) Triplet-triplet annihilation to form singlet states. 6) Exciton transport within the crystal or film so that the excited states can eventually reach an acceptor substrate. Acronyms: TA – transient absorption. TR-PL – time-resolved photoluminescence. TR-2PPE – time-resolved two-photon photoemission. 2DES – two-dimensional electronic spectroscopy. TR-EPR – time-resolved electron paramagnetic resonance. TRIR – time-resolved infrared spectroscopy. ISRS – impulsive stimulated Raman spectroscopy. RR – resonance Raman spectroscopy. FSRS – femtosecond stimulated Raman spectroscopy. TAM – transient absorption microscopy. SO-FSRS – spatially offset FSRS.

to the formation of ^{1}(TT) from S_1. As this step is easily photoinitiated, it has been characterized by a wide range of electronic, magnetic and vibrational techniques. Step 2 refers to the separation of ^{1}(TT) to form ^{1}(T...T). Our understanding of ^{1}(T...T) as a distinct intermediate is relatively recent, and thus this step of the SF process has only been studied by TA, 2DES, TRIR and FSRS. Step 3 refers to the formation of individual triplets T_1 and is the second most commonly studied step because SF is not considered complete until individual triplets are formed. After the individual triplets are formed, they can either be harvested by triplet energy transfer or electron hole pair generation (step 4), or undergo triplet-triplet annihilation to reform the excited singlet S_1 or hot S_0 states (step 5). Step 4 requires the presence of an acceptor material and has only been studied by TA, TR-PL and TR-2PPE to date. Meanwhile, step 5 has only been studied by delayed fluorescence which specifically probes the fluorescence of the singlets formed by triplet-triplet annihilation. Step 6 refers to the movement of singlet and triplet excitons towards an acceptor material, where these photoinduced charged species can be harvested, and it can occur simultaneously with all other steps of SF. Although exciton transport is not a process unique to SF, understanding and improving efficiency of exciton movement is crucial for SF-based optoelectronic applications.

Besides experimental techniques, computational studies also help us interpret complex experimental results, predict what molecules can undergo SF and investigate role of molecular structure in facilitating SF as detailed in these reviews. [29, 30] For example, Morrison et al. found that the strong coupling of

intramolecular modes in the range of 1400–1600 cm^{-1} to the $S_1 \rightarrow {}^1(TT)$ transition helped to explain the temperature independence of SF rates in tetracene. [31] In another study, Shizu et al. found that twisting between tetracene dimers led to stronger vibronic coupling which in turn led to higher rates of formation of ${}^1(TT)$. [32] These computational studies highlight the importance of understanding the roles of molecular structure and vibrations in facilitating SF, advocating for more experimental probe into the structural evolution of molecules during SF.

2.3 Structural Dynamics During Singlet Fission

2.3.1 IR-based techniques

Time-resolved IR spectroscopy can be used to monitor the structural changes within molecules by tracking the vibrational features that are sensitive to the identity of electronic states. Ultrafast TRIR has been used to study the dynamics of the intermediates, ${}^1(TT)$ and ${}^1(T...T)$, formed during SF in a variety of acenes such as hexacene, TIPS-pentacene, tetracene derivatives and xanthene-based dimers. By probing transient structures with molecular specificity, TRIR has been used to identify structural intermediates, as well as distinguish between direct and mediated SF mechanisms.

To examine the structural dynamics of the intermediate electronic states in SF, Deng et al. used femtosecond transient infrared (fsIR) spectroscopy to observe unique vibrational signatures corresponding to S_1 and ${}^1(TT)$ states in addition to a transient spectral evolution of the ring stretching modes of hexacene at ~ 1600 cm^{-1}. [33] Complementing their experimental results with ab initio calculations,

they identified the reaction coordinate and learned that the direct $S_1 \rightarrow {}^1(TT)$ transition is predominantly driven by a few ring stretching normal modes around 1600 cm^{-1}. This novel study provide insights into the specific nuclear motions that drive the evolution of the excited state potential energy surface during SF in hexacene.

In addition to identifying the vibrational motions that results in shuttling the molecules into the $^1(TT)$ states, mid-IR transient absorption has also provided insights into the much-debated one step or two-step mediated mechanism for the formation of $^1(TT)$ during SF. For efficient harvesting of $^1(TT)$, it is necessary to examine the dynamics of its formation during the SF process. However, due to spectral overlap between the $^1(TT)$ and the separated triplets, it is challenging to study the dynamics unique to that of the $^1(TT)$ intermediate. To address this, Chen et al. employed ultrafast mid-IR spectroscopy to characterize the spectral features of the $^1(TT)$ state in a covalently linked slip-stacked terrylene-3,4:11,12-bis(dicarboximide) (TDI) dimers. [34] Their fsIR spectroscopy results identified the spectral feature of $^1(TT)$, which displayed some characters of the T_1 and charge transfer states in the carbonyl stretch and the C=C stretch regions respectively. The simultaneous presence of vibrational characteristics of both the triplet and charge transfer states indicated the formation of $^1(TT)$ in TDI dimers via a charge transfer-mediated SF process. In a similar study, Margulies et al. used time-resolved spectroscopy in the vis-NIR and IR regions to elucidate the effect of chemical substituents on SF in a series of cyano-substituted tetracenes. [35] They observed distinct vibrational frequencies for the CN stretch mode in the singlet and triplet states. By monitoring the dynamics of the vibrational band of the

cyano group (CN), they found evidence of charge transfer species mediating ^{1}(TT) formation in one system. Therefore, these vibrational dynamical studies suggest the first step in SF is the charge transfer mediated mechanism of ^{1}(TT) formation as opposed to the direct mechanism. The direct observation of a charge transfer intermediates using vibrational spectroscopies highlights the role of the two-step charge transfer mechanism for efficient SF. These investigations demonstrate that the distinct narrow vibrational features are sensitive to the electronic states of the chromophores and can be used to assign dynamics corresponding to each electronic state, unique to vibrational spectroscopy.

Ultrafast mid-IR spectroscopy has also been employed to provide mechanistic information during the subsequent steps of the SF process. Grieco et al. used ultrafast mid-IR transient absorption and ns-to-µs time-resolved IR spectroscopy to identify the spectral signatures of ^{1}(TT) and ^{1}(T...T) in TIPS-pentacene thin films as depicted in Figure 2.2. [36,37] They probed the asymmetric alkyne (C≡C) stretch of the side groups to follow the dynamics of the correlated triplet pair separation during SF. The mid-IR transient absorption spectra consisted of a narrow alkyne stretch at 2132 cm^{-1} superimposed on a broad electronic photoinduced absorption (PIA) feature, which corresponded to the excited state absorption from the S_1 and ^{1}(TT) as shown in Figure 2.2b and c. By analyzing the dynamics of the PIA spectra in Figure 2.2d and e, they assigned the alkyne shift from 2132 to 2116 cm^{-1} to the ^{1}(T...T) state and found that TIPS-pentacene molecules transitioned

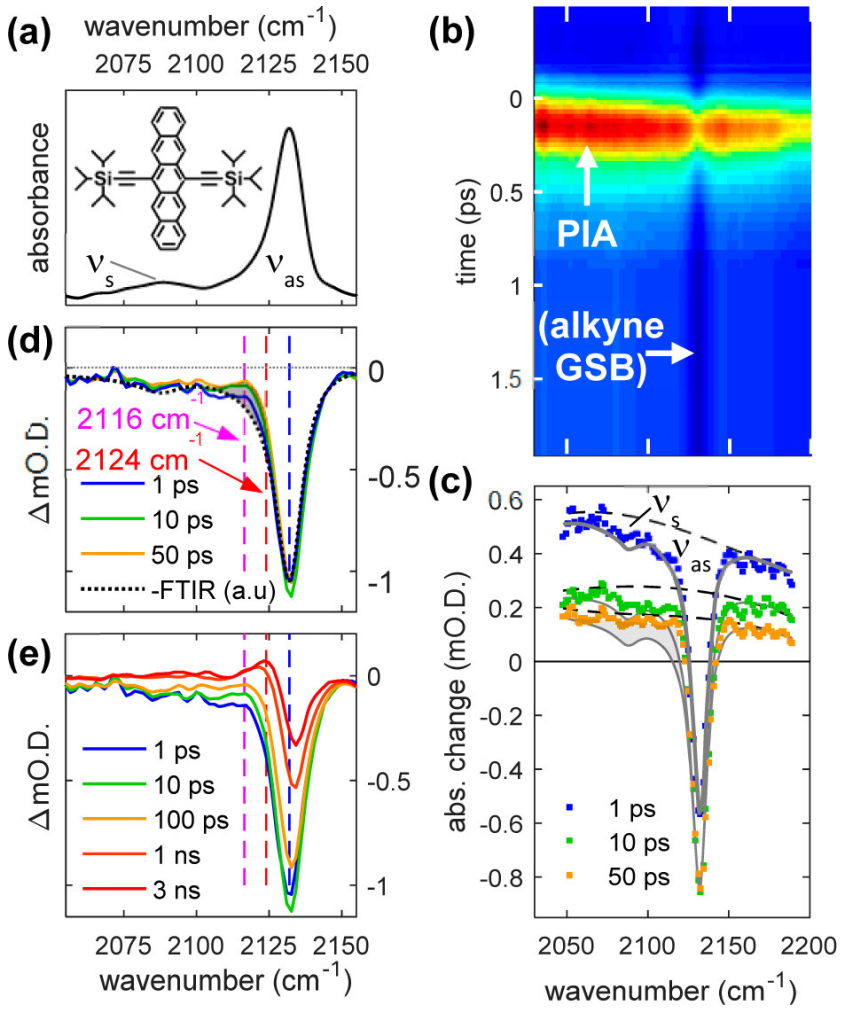

Figure 2.2: (a) Molecular structure and FTIR spectrum of the alkyne stretch mode in TIPS-pentacene thin films. (b) Mid-IR transient absorption spectra after photoexciting to the S_1 state. Ground state bleach (GSB) and photoinduced absorption (PIA) resulting from correlated triplet pairs intermediates. (c) Spectral slices from b at various time intervals highlighting the alkyne stretch mode and broad photoinduced absorption from correlated triplet pairs. (d) Background subtracted data from c, where marked arrowed corresponds to vibrational features of the triplet excitons (2116 cm^{-1}) and hot ground state (S_0*) molecules (2124 cm^{-1}). (e) Transient plots at longer time delays displaying vibrational dynamics during SF. Reproduced with permission from American Chemical Society, Copyright (2017).[36]

within 3.4 ps from the ^{1}(TT) to the ^{1}(T...T) state. The authors also suggested that the complete dissociation of the ^{1}(T...T) state into T_1 states occurs on a nanosecond timescale. This study demonstrates the strength of directly probing vibrational modes where it led to the identification and characterization of the ^{1}(T...T) state, an otherwise difficult-to-isolate state using electronic spectroscopies. Additionally, they observed an absorption feature at 2124 cm^{-1} corresponding to the hot ground state (S_0*) which reached half its final population within 50 ps. This fast time scale of populating the S_0* states was attributed to the excess energy distribution after vibrational cooling from the initially photoexcited S_0 states. This study thus highlights the utility of probing vibrational motions to provide insights about the energy dissipation pathways within electronic states along the SF process. Monitoring the energy flow movement during SF will open up the opportunity to understand its influence on the rate and yield of generation of the separated triplets for their harvesting in optoelectronic devices.

In addition to thin films, Grieco et al. also used mid-IR transient absorption to examine SF in solution by probing the local molecular environments in TIPS-pentacene. [38] They monitored the temporal evolution of the C≡C stretch of the side group and C–H stretch motions of the alkyl chains in the side group in TIPS-pentacene solution. This study showed that the TIPS-pentacene molecules form aggregates through their side groups that break the molecular symmetry, enabling rapid and efficient SF rather than diffusive interactions of the excitons in solution as previously thought. This study highlights the structural insights gained from vibrational motions to better comprehend the intermolecular interactions and symmetries that mediates SF. TRIR spectroscopy has thus emerged as a new

technique capable of examining the excited state dynamics, structure and nature of electronic states in SF chromophores through vibrational spectra. It has helped to identify the vibrational signatures of the intermediates ^{1}(TT) and ^{1}(T...T), and triplet excitons in acene systems. It has provided insights towards elucidating charge transfer mediated SF process, nuclear motions driving the formation of triplets, competition between relaxation pathways and triplet harvesting from ^{1}(TT), and effect of intermolecular coupling and molecular symmetry on SF in acenes. These studies demonstrate the utility of TRIR to explore the structural origins of electronic states in materials for the development of future SF-based optoelectronic devices.

2.3.2 Raman-based techniques

Steady state and time-resolved Raman spectroscopies can probe conformational changes by monitoring the inherently narrow vibrational Raman bands and their sensitivity to changes in molecular structure during SF. Steady-state Raman spectroscopy is useful in unambiguously assigning the structure of long-lived triplet states. Picosecond and femtosecond Raman spectroscopies have been used to characterize triplet states and illustrate SF in acenes and biological systems, study the role of vibronic coherences in driving the photophysics, identify specific nuclear motions along the SF reaction coordinate, and provide design guidelines to modify the molecular structure for efficient SF in acene based chromophores.

Steady-state resonance Raman spectroscopy has been applied to determine structure of the long-lived triplet states generated by the SF process, useful in quantifying reorganization energies and identifying molecular structural changes

between S_0 and T_1 states. For example, Angelella et al. probed the resonance Raman spectra of both the ground and triplet state of perylene bis(dicarboximide) (PDI) dimer. [39] They assigned 1324 (C–H in-plane bends), 1507 (perylene core I), 1535 and 1597 (perylene core II) cm^{-1} bands to T_1 signatures and noticed that they were red-shifted with respect to corresponding bands in the S_1 states. Chen et al. also measured resonance Raman spectra of triplet states of tetramer and hexamer oligothiophenes, showing that the T_1 excitation is delocalized at least over five rings. [40] Llansola-Portoles et al. used transient absorption and resonance Raman measurements to prove that lycopene crystalloids extracted from tomatoes undergo SF, the first time SF has been observed in a biological structure. [41] In the steady-state they observed a power-dependent Raman band at 1128 cm^{-1}, corresponding to C=C stretches which have been previously shown to be fingerprints of carotenoid triplet excited states. These studies illustrate the utility of ground state resonance Raman to spectrally identify triplet state structures.

Picosecond time-resolved resonance Raman (TRRR) spectroscopy, a pump-probe technique that detects transient spontaneous Raman signatures, is an effective tool to quantify the triplet yields during SF. Wang et al. implemented TRRR to prove that zeaxanthin aggregates undergo SF with $\sim$ 90–200% quantum yield [42, 43] and observed distinct vibrational features corresponding to the ground S_0, S_1 and T_1 states, with a triplet rise time of $\sim$ 4 ps. Relatedly, ultrafast stimulated Raman spectroscopy has been used by Jana et al. to examine the structural dynamics in 9,10-bis(phenylethynyl)anthracene under resonance condition to during the ^{1}(TT) formation. [44] Although TRRR can identify different

electronic states associated in SF through vibrational modes, its temporal resolution is limited to 1–2 picoseconds, much longer than the ultrafast (<100 fs) timescale of the relevant nuclear motions to map out the excited state reaction coordinate during SF.

In order to understand SF enough to map out its potential energy surface, researchers require the knowledge of the evolution of the electronic states and the relevant nuclear coordinates as a function of time. Understanding the role of vibrational motions and vibronic couplings in the SF process has gained momentum recently, with many groups attempting to determine the contribution of vibronic coherence to the SF pathway. Stern et al. utilized TA and resonance Raman spectroscopy to reveal that certain vibrational modes in TIPS-tetracene drive the nuclear wavepacket originally generated in the S_1 state to the ^{1}(TT) potential energy surface, suggesting that ^{1}(TT) forms via a vibronic coherent process on an ultrafast timescale (<300 fs). [45] 2DES is an electronic technique sensitive to probing contributions of Raman active modes, and is able to extract such information through vibronic coupling. Bakulin et al. used 2DES to identify the Raman bands in pentacene and its derivatives, suggesting that the mixing of vibronic manifolds of the S_1 and ^{1}(TT) states play a key role in SF for pentacene and two of its derivatives. The coupling between electronic and vibrational states guides the photochemical reaction pathways in molecules. Identifying the coupled nuclear motions and its effect on the coupling between the states can allow us to synthetically modify existing molecules and design new molecules to tune the outcome of the ultrafast SF process.

To identify the importance and nature of vibronic coherence during SF, Musser

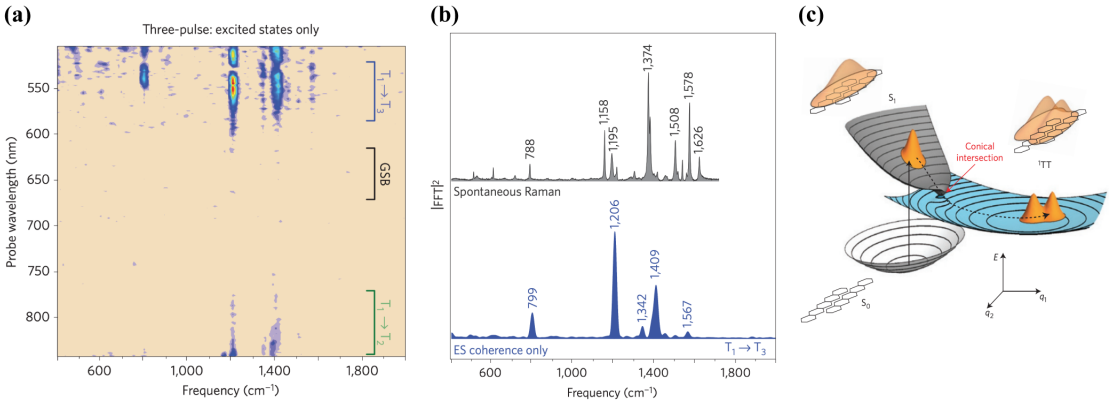

Figure 2.3: (a) Pump-dump-pulse experiment to observe vibrionic coherence in the region of the excited state absorption in the triplet manifold. (b) Integration of the frequency map in the dark blue bracket region in (a) generates the vibrational modes of the triplet exciton. Spontaneous Raman spectrum in grey is to compare the vibrational frequencies in the ground S_0 and the triplet states (dark blue). (c) Schematic representation of the progress in SF mediated via a conical intersection. Reprinted by permission from ref [17]. Copyright (2015) Springer Nature.

et al. employed a pump-dump-probe technique to selectively depopulate the excited triplet states to measure the importance of vibronic coupling during SF in thin films of 6,13-bis(triisopropylsilylethynyl) (TIPS)-pentacene. [17] Using the three-pulse experiment, they isolated the vibrational coherence in the final excited triplet states while removing the ground state coherence, Figure 2.3a. Integration of the frequency map from the three-pulse experiment in the excited state absorption bands in the triplet manifolds and comparing it with the spontaneous Raman spectrum revealed the distinct vibrational modes of the triplet exciton in Figure 2.3b. This transfer of the initially generated wavepacket in the singlet excited state into the separated triplet states is mediated through the correlated triplet pair indicating the presence of vibronic coupling between the S_1 and the ^{1}(TT) states. They thus proposed that the presence of such strong vibronic coupling is

evidence that SF in TIPS-pentacene undergoes the direct mechanism mediated by a conical intersection between the singlet and triplet manifolds, as shown in Figure 2.3c. Although this technique is unable to identify the specific nuclear motions driving the system towards the crossing, the presence of conical intersection explains the high rate and efficiency of SF in TIPS-pentacene and helps to map out a part of the complex potential energy surface. This model of the presence of conical intersection mediating the SF process can thus be generalized to other ultrafast SF chromophores. The understanding of coherences can be used for effective designing of new SF chromophores by modulating the strength of the vibronic coupling between the S_1 and ^{1}(TT) states.

In crystals, the coupling of individual molecular vibrations with the lattice play a role in driving SF relevant photophysical processes. Impulsive stimulated Raman spectroscopy can observe the low frequency modes of these excited electronic states without interference from Rayleigh scattering. Schnedermann et al. combined excited-state time-domain Raman spectroscopy and quantum mechanical simulations to probe the nature of the vibrational coherence in the ^{1}(TT) state and to identify the vibrational modes driving the SF process to construct a molecular movie of the ultrafast SF in real-time in a pentacene dimer. [46] Integrating the wavelength-resolved impulsive Raman data in different spectral region, they obtained the vibrational modes unique to S_0, S_1 and ^{1}(TT) states, as shown in Figure 2.4a and 2.4b. Their results demonstrated the roles vibrational modes with A_1 symmetry and B_1 or B_2 symmetry, as shown in Figure 2.4c, play during SF. Vibrational modes with A_1 symmetry do not mediate the coupling between S_1 and ^{1}(TT) states, but instead modulate the pentacene core structure and act as

tuning modes associated with in-plane ring deformation motions during the SF reaction. Meanwhile, modes with B_1 or B_2 symmetry correspond to the coupling modes, which are associated with the twist around the pentacene-pentacene bond.

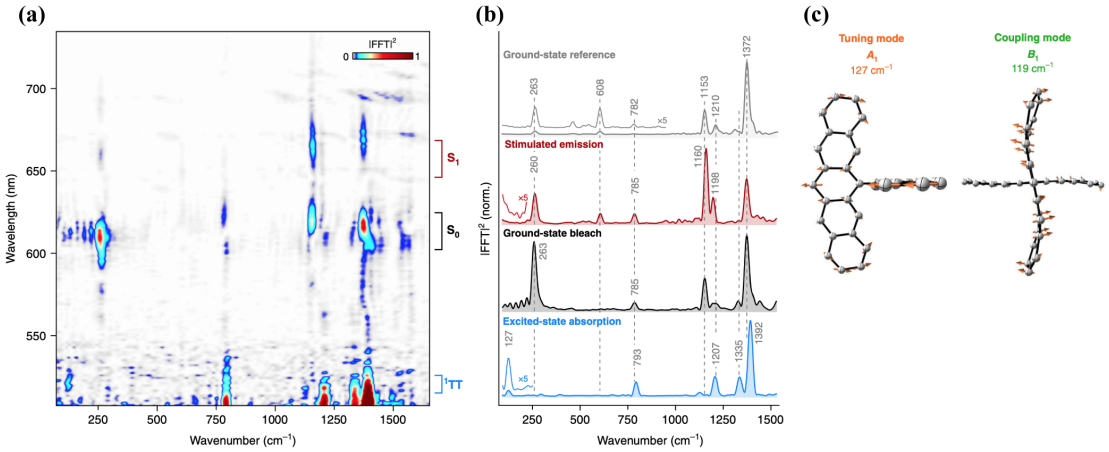

Figure 2.4: (a) Wavelength-resolved impulsive Raman spectra of pentacene dimer after impulsively populating the S_1 state. The marked regions represent the spectral map of the S_1, S_0 and ^{1}(TT) states. (b) Integrated region of the bracketed regions in (a) generates the impulsive Raman spectra of different species: stimulated emission (S_1), ground state bleach (S_0) and excited state absorption (^{1}(TT)). The off-resonant impulsive Raman spectrum in ground state is in grey for comparison of the vibrational modes in the excited states. (c) Representative normal modes for the tuning and coupling mode during SF. Reprinted by permission from ref [46]. Copyright (2019) Springer Nature.

Their real space movie showed that the first 75 fs was dominated by in-plane ring deformation which positions the energy levels for efficient S_1 to ^{1}(TT) transition. The next 125 fs was dominated by the twist around the pentacene-pentacene bond which drives the conversion of the S_1 to ^{1}(TT). However, the coupling modes were computationally predicted to be less intense than the tuning modes by an order of two, hence were obscured and rarely observed experimentally. Using a vibrationally sensitive technique, this study not only highlights the function of

vibrational modes during SF in real time but also recognizes the driving motions for efficient ^{1}(TT) generation in real time, which was previously unknown. Identifying those unique nuclear motions can then be used for either mode-selective excitation to facilitate the efficient ^{1}(TT) generation and can be used as guidelines to synthetically modify chromophores that can display those vibrations without attenuation for their use as efficient SF chromophores.

Femtosecond stimulated Raman spectroscopy (FSRS) is an ultrafast structurally sensitive technique used to study real-time transient structural evolution during SF. FSRS can provide vibrational structural information on a timescale which is comparable to the time period of the probed nuclear motions. It can have both high temporal (sub-50 fs) and spectral (10 cm^{-1}) resolution, while still obeying the Heisenberg's uncertainty principle. What sets FSRS apart from other IR-based techniques is that it can simultaneously probe vibrational features over a wide spectral window of 3000 cm^{-1}. This is important as the SF chromophores displays numerous vibrational motions over a wide frequency range, and FSRS can probe them all together as compared to other ultrafast IR spectroscopies, that are typically limited to narrower spectral region. Even though the scattering cross-sections are the same as for spontaneous Raman, the scattering signal is enhanced by six orders of magnitude in FSRS leading to high signal-to-noise ratios and shorter acquisition times. Additionally, FSRS is a nearly fluorescence-free technique due to the signal being detected in the small solid angle. This unique property of FSRS makes it well-suited to study SF chromophores where fluorescence background can overwhelm the vibrational signatures of interest. Each of

these unique qualities of FSRS helps to obtain relevant changes in vibrational energies across broader regions of the same molecules during SF, providing a more holistic view of structural change during SF.

In order to obtain structural information used to determine the mechanism of SF, Hart et al. used FSRS to study the triplet formation mechanism in crystalline pentacene. [47] From the FSR spectra of pentacene crystals, they observed a broad transient absorption background, which corresponded to spectral signatures of triplet states formed beyond $\sim$ 800fs. Before the formation of the triplet states, they observed two excited state Raman peaks, one upshifted and one downshifted by $\sim$ 5–25 cm^{-1} for each of the ground S_0 peaks. Based on the kinetics of the Raman vibrational modes and theoretical calculations, they assigned the split Raman bands to intermediates with charge transfer character, suggesting that SF in crystalline pentacene proceeds via the two-step charge transfer mediated mechanism. Therefore, this study provides insights into the evolution of the intermediate charge transfer states on the highly anharmonic potential energy surfaces and suggests that anionic and cationic species could play a role in facilitating efficient SF. This work lays out the structural evolution in molecules during the early ^{1}(TT) formation step during SF, which can help in modifying existing materials for effective optoelectronic devices.

The ^{1}(TT) state must separate into triplets for efficient harvesting of solar energy and thus further investigation of the structural reorganization during the separation of the ^{1}(TT) is needed. In order to gain insights into the molecular nuclear dynamics during the SF triplet separation process, Bera et al. studied the structural evolution in crystalline rubrene with FSRS (Figure 2.5a). [48] As

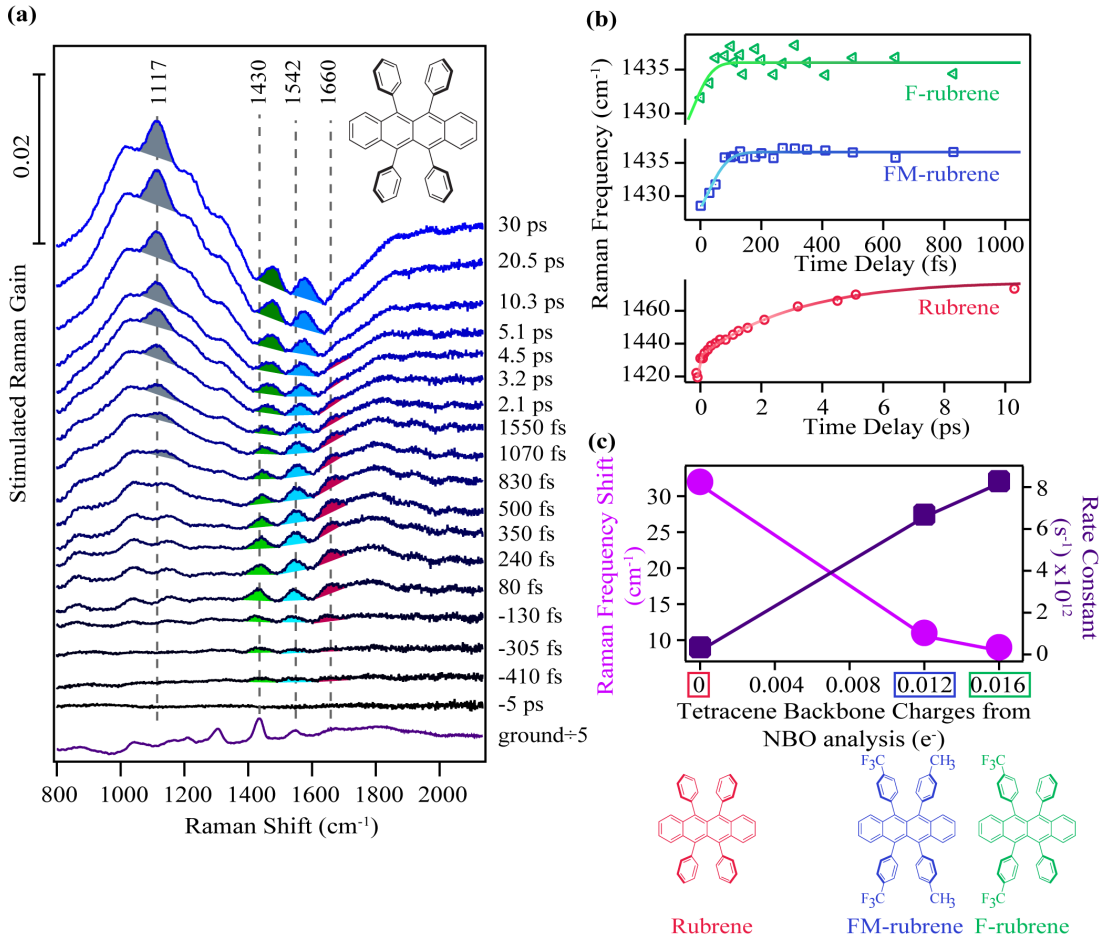

Figure 2.5: (a) Molecular structure and time-resolved FSR spectra in crystalline rubrene at different time delays after photoexcitation. (b) Transient time evolution of the 1430 cm^{-1} Raman mode displaying a blue shift during the ^{1}(TT) separation in rubrene, FM-rubrene and F-rubrene. (c) Total shift of the 1430 cm^{-1} Raman mode and the associated rate constant for this peak shift as a function of total charge on the tetracene backbone calculated from natural bond orbital (NBO) population analysis in the rubrene derivatives series. Adapted with permission from American Chemical Society, Copyright (2017) [48] and reference [49].

shown in the time-resolved FSR spectra in Figure 2.5a, they not only observed a vibrational feature around 1660 cm^{-1} corresponding to the ^{1}(TT) state, but also two Raman modes around 1430 cm^{-1} and 1542 cm^{-1} that displayed large transient frequency shifts to higher frequencies. Analyzing the dynamics of these Raman peak frequencies, they found that these frequency shifts occur on the same timescale as the separation of ^{1}(TT) to ^{1}(T...T). Based on spontaneous Raman measurements on a rubrene derivative and density functional theory calculations on rubrene charged species, they attributed the blue shift of the Raman modes during the separation of the correlated triplet pair ^{1}(T...T) to a structural reorganization that shifts the electron density away from the tetracene core of the crystalline rubrene molecules. Given that the ^{1}(TT) $\rightarrow$ ^{1}(T...T) is associated with loss of electron density, they proposed that molecules that facilitate similar changes in core electron density will undergo efficient SF.

Building off on the structural evolution knowledge gained during crystalline rubrene SF, Bera et al. have successfully screened and designed fluorinated rubrene derivatives, F-rubrene and FM-rubrene, with reduced core electron density, as shown in Figure 2.5c to study the prospects of spectroscopy-guided rational designing of SF chromophores. They observed similar blue-shifting of the transient Raman peak at 1430 cm^{-1} in the rubrene derivatives as they observed in unsubstituted rubrene, as summarized in Figure 2.5b. However, the derivatives displayed lower frequency shifts on a much faster timescale compared to rubrene. Therefore, not only did they provide the first experimental evidence of SF in those rubrene derivatives, but they also observed SF rates an order of magnitude higher in the derivatives than non-substituted rubrene (Figure 2.5c). Using FSRS, they

demonstrated that the fluorinated rubrene derivatives undergo less structural reorganization than rubrene because the initially more electropositive tetracene core does not have to lose as much electron density to generate the ^{1}(T...T) state. [49] The knowledge of the structural evolution in regards to the electron distribution provides a new synthetic control over the ultrafast SF process. Therefore, this study bridges the gap between the spectroscopic results and its realization as practical application to devise principles for novel materials with better SF properties which goes beyond the energy criteria. These studies by Bera et al. demonstrate the fulfillment of the long-harbored promise of spectroscopy-guided rational engineering design and syntheses formulations of future chromophores for efficient SF.

Thus, ultrafast Raman spectroscopy is ideally suited to investigate the influence of molecular structure on SF, with a unique combination of broadband probing, high temporal resolution, and compatibility with small sample volumes. It has been used to identify the vibrational signatures of the ^{1}(T...T) and charge transfer intermediate species, unique nuclear motions driving the photoexcited wavepackets to the triplet states, structural reorganization during the triplet formation and insights into molecular designing principles. These advances provide means to implement the structural evolution knowledge into synthesizing new SF sensitizers.

2.4 Recent Developments & Future Directions

Vibrational spectroscopy is a well-equipped field to discern underlying mechanism, vibronic couplings and molecular structural changes across different steps

in the SF process. While we have discussed the unique capabilities of vibrational spectroscopy that advanced the SF field, vibrational techniques have yet to reach their full potential in helping us identify design principles for making better chromophores for SF-based devices. In addition to the recent advancements in the SF community, vibrational spectroscopies can have multiple interesting avenues to explore as we discuss in this section.

2.4.1 Magneto-vibrational spectroscopy

The coupling of two triplet states can result in triplet ^{3}(TT) and quintet ^{5}(TT) states in addition to the singlet ^{1}(TT) state. Although quintet ^{5}(TT) states have been observed as SF intermediates in TR-EPR studies, [27, 28, 50] we do not understand their roles in SF well because their electronic and vibrational spectral features are highly similar to that of the ^{1}(TT) state. Incorporating a strong magnetic field with a vibrational technique can make it possible to differentiate the vibrational features of ^{1}(TT), ^{3}(TT) and ^{5}(TT) intermediates and may help us understand whether strong ^{1}(TT), ^{3}(TT) and ^{5}(TT) coupling is desirable for SF process. We can also learn if certain vibrational motions drive molecules towards any of the ^{1}(TT), ^{3}(TT) and ^{5}(TT) states, and use that insight to optimize certain excitation pathways. While not yet utilized in a SF study, magnetoinfrared spectroscopy, where IR spectra were collected under magnetic fields of various strengths, was used to investigate magnetic transitions in single crystals of antiferromagnet $[Cu(HF_2)(pyz)_2]BF_4$. [51] Musfeldt et al. observed red shifting of out-of-plane pyrazine ring deformation and out-of-plane C–H bending modes at

higher magnetic fields, revealing that the pyrazine ring was distorted to accommodate the fully polarized magnetic state. [51] If a similar magneto-vibrational technique were to be applied on SF systems, we would have a better understanding of the dynamics involved with ^{3}(TT) and ^{5}(TT) during SF and if the three-step process in equation 2.1 is actually an accurate description of SF in all molecular systems. Based on this spectroscopic technique, molecular systems where the appropriate relative molecular orientations and vibrational motions can access the ^{3}(TT) and ^{5}(TT) can be designed for understanding SF from a mechanistic viewpoint.

2.4.2 Mode-selective excitation

Another exciting future possibility is the application of mode-selective excitation to drive or inhibit SF in organic chromophores in order to confirm the role of specific nuclear contributions in the SF process. Mode-selective excitation and inhibition of Raman or IR modes can be achieved by shaping femtosecond pulses to excite desired vibrational modes while suppressing others. [51] For example, Grumstrup et al. made use of adaptive pulse shaping to increase triplet yield in tetracene films, leading to a 20% increase in the triplet absorption feature. [52] A computational study by Castellanos et al. also revealed that destructive interference between two co-existing charge-transfer mediated fission pathways in a model pentacene dimer can be suppressed by intermolecular vibrations, leading to a more efficient SF process. [53] Recently, Paulus et al. identified excited state vibronic coherences in iron(II)-based chromophores, and then synthetically modified the molecules to interfere with the vibrational modes associated with

the coherences, which led to more than a 20-fold increase in the lifetime of the photo-induced excitons. [54] Similar studies could be done with SF chromophores, where it is possible to synthetically modify molecular structure to affect the vibrational motions of interest that facilitate SF while simultaneously inhibiting other relaxation pathways, increasing exciton lifetimes and diffusion lengths, therefore improving the efficacy of SF based photovoltaics.

2.4.3 Terahertz spectroscopy

Analogous to vibronic coupling, phonon modes can couple to electronic states in thin-films or crystalline chromophores undergoing SF. Terahertz (THz) spectroscopy is a vibrational technique that spans the electromagnetic spectrum between the microwave and the far IR regions, matching the energies of crystalline phonon vibrations and intermolecular bonding. [55] Although not yet utilized in a SF study, it has been increasingly used to investigate carrier dynamics in photovoltaic materials. [56] In a recent example, Lan et al. used time-resolved multi-THz spectroscopy to probe coherent and incoherent charge carrier dynamics in low temperature orthorhombic phase of methylammonium lead iodide perovskite. [57] With the aid of computational calculations, they assigned excited-state THz spectral features to two distinct populations of free and bound excitons that appeared at different time scales. They also observed charge coupling to the low energy phonon mode at 30 cm^{-1}, which likely arose from mixed inorganic and organic sublattice motion. Employing THz spectroscopy to SF systems would help to decipher the roles that phonons or intermolecular interactions play during each step of the SF process. This will enhance our understanding further into the role and

importance of lattice orientation and molecular packing contributions to efficient SF.

2.4.4 Exciton transport

As our understanding of the SF mechanism improves, more studies emerge that are dedicated to optoelectronic device optimization. We believe that the next step forward, in addition to synthesizing newer classes of SF chromophores, is to minimize energy losses from transport by understanding how the charge carriers propagate. Previous studies have mainly employed electronic spectroscopic techniques such as TR-PL and TA to study the charge carrier transport and recombination dynamics during SF. For example, Akselrod et al. have imaged exciton transport in tetracene crystal and thin film by detecting the delayed fluorescence from triplet-triplet fusion. [58] This study showed the importance of nanoscale morphology on exciton transport: the transit mode in crystals was random walk diffusion, but was sub-diffusion in thin films due to the presence of exciton traps. Meanwhile, Huang et al. utilized transient absorption microscopy (TAM) to simultaneously image singlet and triplet exciton transport and discovered the cooperative nature of their transport. [59] As singlet and triplet excitons have different TA bands, Huang et al. generated separate exciton maps to extract diffusion lengths of singlet and triplet excitons in SF chromophores respectively. Although these time-resolved spectroscopic techniques have provided valuable information about the exciton charge transport dynamics, they do not provide the influence of molecular structural properties on the transport process, making it harder to target specific functional groups to improve the transport properties of

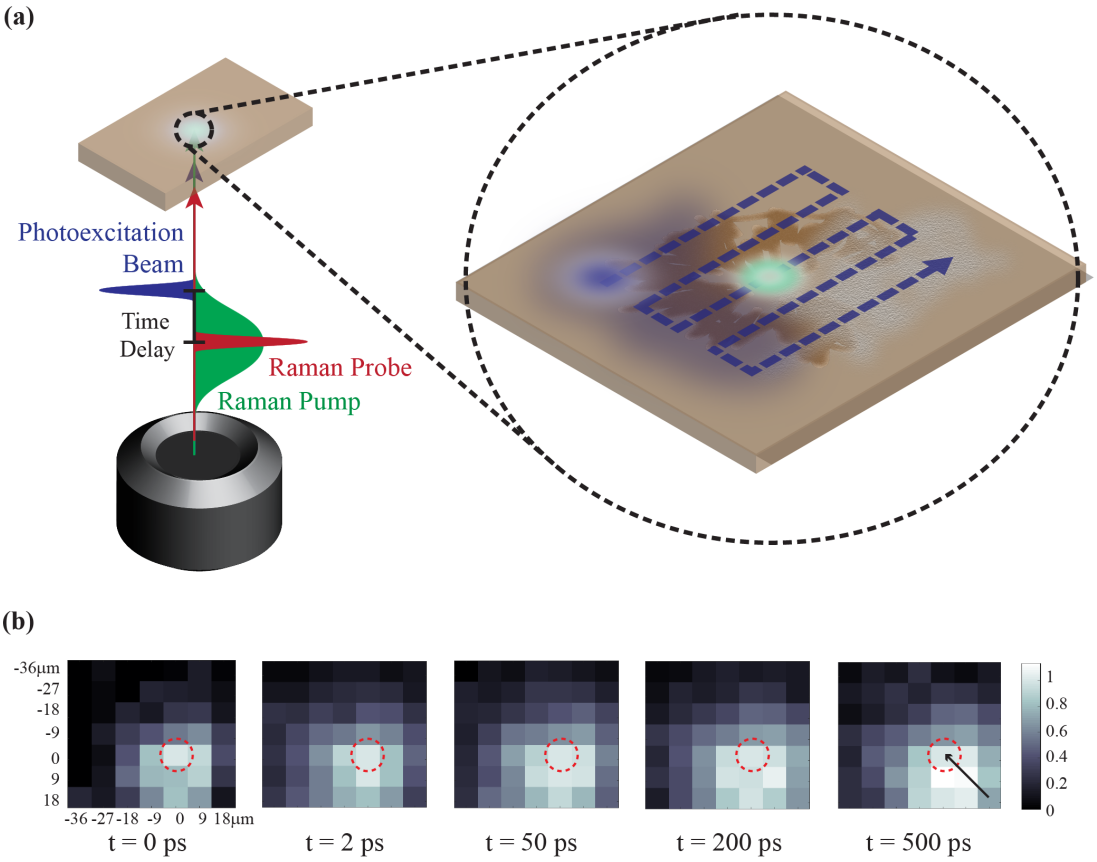

Figure 2.6: (a) Schematic representation of the pulse profiles and raster scan for SO-FSRS experimental set-up. (b) Evolution of the 1386 cm^{-1} vibrational mode depletion in TIPS-pentacene at different photoexcitation positions over time. The dashed circle represents the position of the Raman probe pulse. The arrow in the rightmost panel represents the diffusion direction of the excitons generated in bottom right photoexcitation position, which falls along the fast exciton transport axis in TIPS-pentacene. Adapted with permission from American Chemical Society, Copyright (2020).[60]

existing materials.

To extract molecular structural information during transport, Kwang et al. have recently developed spatially offset femtosecond stimulated Raman spectroscopy (SO-FSRS), which combines the strength of vibrational studies and exciton transport imaging. [60] As seen in Figure 2.6a, the photoexcitation pulse is raster-scanned across the Raman pump and probe pulses, which are held stationary with time. Thus, excitons need to propagate from the initial photoexcitation zone to the probing zone before they can be observed. Although SO-FSRS is still a technique in its infancy, it verified that the fast exciton transport axis is identical to that of free charge carriers in TIPS-pentacene and that exciton transport is less anisotropic than free charge carrier transport. By tracking the Raman bleaching features of TIPS-pentacene at each photoexcitation location, they generated excited state structural maps at multiple time delays as shown in Figure 2.6b, providing a visual representation of exciton transport over time. This allows us to observe how molecular structure evolves spatially as excitons travel through the material. As the vibrational analog of TAM, SO-FSRS can help to identify specific molecular interactions that facilitate or hinder charge and exciton transport in SF systems for future studies. By offering valuable insight on how to design molecules that both undergo efficient SF and have long-range energy transport efficiency, SO-FSRS helps to move closer to achieving commercialization of SF based optoelectronic devices.

2.5 Conclusions

This chapter demonstrates that the vibrational spectroscopy has emerged as a technique capable of examining the influence of molecular structure and its evolution in chromophores to broaden the understanding of SF, as well as to give roadmaps on how to modify existing molecules to make them better suited for SF-based applications. The importance of vibrational motions in SF research started with the realization that vibronic coupling mediates the SF process in many organic chromophores. Combined with theoretical studies, this has given a considerable amount of momentum for the employment of vibrational spectroscopy to understand the role of molecular structure of the materials on the electronic states and its influence on the SF efficiency. The sensitivity of vibrational features to local environments makes it possible to identify molecular interactions that facilitate or hinder progress in each step of the SF mechanism. Studies using time-resolved infrared spectroscopy have identified the specific nuclear motions driving the coherent SF process, thereby providing a tool to control photochemistry. Ultrafast Raman spectroscopy has successfully exhibited its strength in providing real-time structural reorganization knowledge of the excited electronic states and have guided the screening procedure and intelligent design principles for efficient SF chromophores. These techniques together help understand the SF pathway and provides roadmaps to design new molecules that are better suited for SF applications by modifying specific areas within existing molecules.

2.6 Acknowledgements

This work is supported by Department of Energy DE-SC0018203 and the Doctoral Dissertation Fellowship award from University of Minnesota. We thank Dr. Christopher C. Rich and Dr. Ariel Alperstein for their critical reading and feedback.

Chapter 3

Femtosecond Raman Microscopy Reveals Structural Dynamics Leading to Triplet Separation in Rubrene Singlet Fission

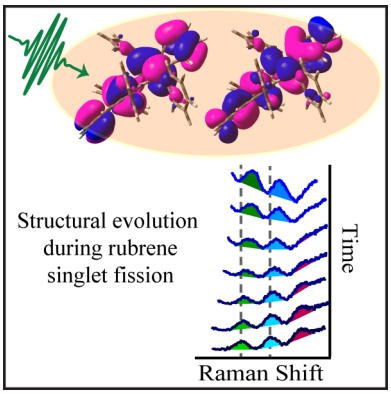

Reprinted with permission from the manuscript by Kajari Bera, Christopher J. Douglas and Renee R. Frontiera, *J. Phys. Chem. Lett., 2017*, 8 (23), 5929-5934.

3.1 Overview

Singlet fission generates multiple excitons from a single photon, which in theory can result in solar cell efficiencies with values above the Shockley-Queisser limit. Understanding the molecular structural dynamics during singlet fission will help to fabricate efficient organic photovoltaic devices. Here we use femtosecond stimulated Raman spectroscopy to reveal the structural evolution during the triplet separation in rubrene. We observe vibrational signatures of the correlated triplet pair, as well as shifting of the vibrational frequencies of the 1430 and 1542 cm^{-1} excited state modes, which increase by more than 25 cm^{-1} in 5 ps. Our results indicate that the correlated pair separation into two individual triplets occur concurrently with the loss of electron density from the tetracene backbone in rubrene. This study provides new insights to the triplet separation process and proves the utility of structurally-sensitive ultrafast vibrational techniques to understand the mechanism of singlet fission.

3.2 Introduction

The efficiency of single junction photovoltaic devices is limited by the Shockley-Queisser limit to values of $\sim$ 34%. [1] Fortunately, this number can be increased to 45% through a process known as singlet fission (SF) in which two electron-hole pairs are generated from a single photon. [2, 9] This phenomenon has been used in photovoltaics and photodetectors with an external quantum efficiency of 109% [6] and $\sim$ 100% [61], respectively, due to the high efficiency of singlet to triplet conversion. [3, 16] Despite these promising advances, photodriven devices

that make use of SF are not yet viable for widespread commercial adoption and further gains in overall efficiency will likely require a greater understanding of the mechanisms of energy conversion and charge transport in order to minimize losses.

The process of SF is depicted in a simplified form as [62]

$$S_0 \rightarrow S_1 \leftrightarrow {}^1(TT) \rightarrow {}^1(T...T) \rightarrow T + T \tag{3.1}$$

After photoexcitation, a singlet exciton (S_1) interacts with a neighboring ground state molecule forming a correlated triplet pair, ^{1}(TT), followed by the separation of the triplet pair, $^1(T\ldots T)$, and eventual separation into two individual triplets. Previous studies have largely examined the triplet generation process [2,3,22,63–65], which is typically extremely efficient in most SF materials and thus, challenging to optimize further. However, only a few have identified structural signatures of the correlated triplet pair [23, 25, 66, 67] and its subsequent separation dynamics. [24, 66, 68] Triplets formed after the separation of the correlated pair typically have a very long lifetime which helps in exciton diffusion to interfaces for energy harvesting. [69] However, the correlated triplet pair must first separate to generate the uncorrelated triplets for further solar harvesting. This necessitates understanding the underlying dynamics of triplet separation process in SF to identify the specific structural properties needed to generate new materials for highly efficient organic photovoltaics.

Rubrene is an organic semiconductor that undergoes SF in the orthorhombic crystalline form. [70–72] The structure of rubrene is shown in the inset of Figure 3.1a, consisting of four phenyl rings, two on each side of a tetracene backbone.

In rubrene, the energy of the S_1 state is approximately equal to twice the energy of the T state, [71, 73, 74] which is one of the required properties for any molecule to undergo SF. [2, 3] Many studies have shown that rubrene undergoes efficient SF, thereby generating triplets [71, 75, 76] that have long lifetimes (ns-µs) and long exciton diffusion lengths. [75, 77] The quantum efficiency of triplet generation through SF in rubrene crystals is $\sim$ 100%, [78] making it a model system to investigate the structural dynamics associated with SF and multiexciton migration. Even though the fluorescence lifetime in rubrene crystal lasts for picoseconds, [71, 72, 75, 76] a recent 2D electronic spectroscopy (ES) study found that the formation of the correlated triplet pair is extremely fast, on the order of 20 fs, and is in equilibrium with the bright S_1 state, and the correlated triplet pair has a lifetime of 2 ps before separating into two separate triplets. [24] However, to fabricate devices with optimal charge separation and transport properties, it is important to understand the underlying structural dynamics occurring during SF in order to optimize molecular design for efficient solar energy conversion. Thus, structural studies to examine the molecular motions involved with all of the steps in the SF process are urgently needed.

To provide new insights into the molecular conformational changes occurring during SF, we use femtosecond stimulated Raman spectroscopy (FSRS) in a microscope configuration [79] to follow the structural evolution of rubrene during SF and subsequent triplet pair separation. FSRS is an ultrafast vibrational technique that allows for the determination of structural changes in a chemical reaction by monitoring the vibrational modes of the system with high temporal (as short as 50

fs) and spectral resolution (<10 cm^{-1}). [80–85] Since FSRS can monitor the structural changes on the ultrafast timescale of correlated triplet pair generation and separation by probing vibrational dynamics of the system in its excited state, it is well-suited to study the photo-physical processes of SF and triplet pair separation, thus mapping out the potential energy surfaces associated with the dynamics.

3.3 Methods

3.3.1 Rubrene crystal growth

We used $\geq$ 98% purity rubrene powder from Sigma Aldrich and grew the rubrene crystals using the previously reported methods of physical vapor transport. [86, 87] We heated the furnace overnight at 350°C before the crystal growth to minimize impurity content. We then placed 16 mg of rubrene powder in a glass boat inside the furnace in the presence of 0.1 MPa Argon gas with a flow rate of 100 ml/min for 90 minutes to create an inert atmosphere. We heated the furnace to 330°C at the source region by a thermocouple for 35 min and the crystals were formed 5–8 cm away from the source region. We obtained long needle-shaped orange colored rubrene crystals, 4–6 mm long, and then mounted them onto glass slides. F_{20} rubrene was prepared according to our previously reported route. [88]

3.3.2 UV-visible spectroscopy

We obtained the absorption spectrum of rubrene crystals using UV-2600 UV-Vis spectrophotometer by Shimadzu in transmission mode.

3.3.3 Continuous wave Raman spectra

We obtained the spontaneous Raman spectra of rubrene crystals and F_{20} rubrene powder using a home-built Raman spectrometer. We passed a 785 nm laser through a 30:70 beam splitter and focused onto the sample through a 10x Olympus objective. The power of the laser at the sample was 21 mW and we collected the Raman signal in a back-scattering geometry using a Princeton Instruments 2500i spectrograph and a Princeton Instruments PIXIS 100BX CCD array.

3.3.4 Femtosecond stimulated Raman spectroscopy

We collected the time-resolved Raman data on a home-built setup which employed Coherent model Libra-F-1K-HE-110 femtosecond amplifier. [79] The 4.6 W fundamental output at 800 nm was used to generate the three pulses for the FSRS studies. We passed 480 mW of the fundamental output beam through our home-built grating filter to generate a 2.1 ps narrowband Raman pump. [82] We generated the broadband continuum femtosecond Raman probe by passing 2.5 mW of the 800 nm fundamental output through a 2 mm thick sapphire crystal followed by a RG830 long pass filter and then compressed it with a fused silica prism compressor. The photoexcitation pump was generated by a home-built non-collinear parametric amplifier (NOPA). NOPA generation required a seed pulse and a 400 nm pump pulse. The white light seed continuum was generated in a 2 mm thick sapphire crystal. The 400 nm pump pulse was generated by frequency doubling the 800 nm fundamental output using a BBO crystal. The two pulses were then mixed in a 1 mm thick BBO crystal and the resultant visible light was

passed through an SF10 prism compressor to minimize the linear chirp. The photoexcitation pump was tuned to a central wavelength of 536 nm and a FWHM of 14 nm with a Gaussian spectral shape. We sent the three pulses through an inverted Olympus IX 73 microscope and focused them non-collinearly onto the sample using a 35 mm focal length lens. We used a piezoelectric stage to vary the time delay between the photoexcitation pump and the Raman pump-probe. The cross-correlation of the photoexcitation pump and the Raman probe was 250 ± 2 fs as measured by the optical Kerr effect with a 2 mm cuvette of cyclohexane. We focused the Raman probe and the stimulated Raman signal using a 100 mm focal length lens on to a 1/3 meter spectrograph and a Princeton Instruments PIXIS 100F CCD array that collected the spectra at a kHz repetition rate. We used a home-built Labview program to collect the femtosecond stimulated Raman spectrum where each spectrum was collected for 20–90 seconds and obtained the Raman gain spectra by dividing the Raman pump on spectra over Raman pump off spectra.

3.4 Results & Discussions

The steady state absorption spectrum of rubrene single crystal shows four absorbance maxima at 438 nm, 464 nm, 497 nm and 536 nm which indicates a vibronic progression of $\Delta\omega = 1391$ cm^{-1}, as shown in Figure 3.1a. For FSRS measurements, we photoexcited the rubrene samples with a 536 nm femtosecond laser pulse as indicated in Figure 3.1a. The inset of Figure 3.1b shows the rubrene crystal used for FSRS measurements that we grew using physical vapor transport, resulting in a needle-like crystal (Figure A.1).

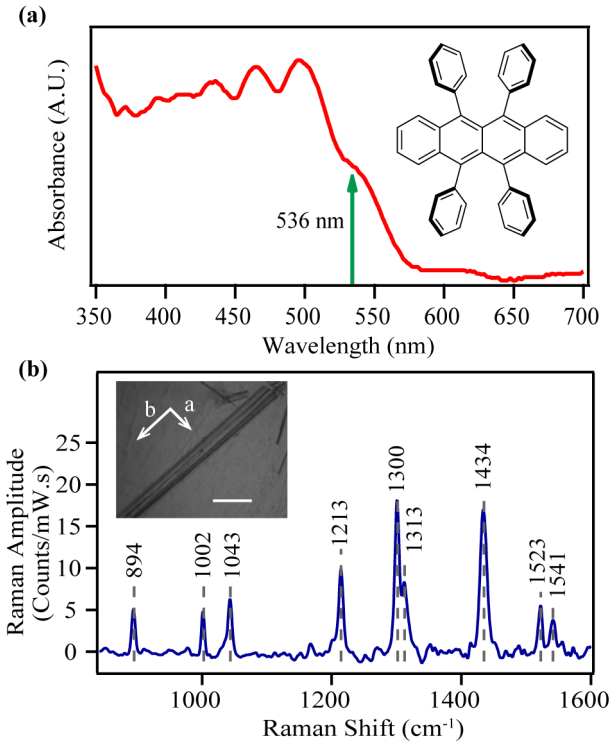

Figure 3.1: (a) Steady state absorption spectrum of the rubrene crystal used for FSRS measurements along with the molecular structure. (b) Spontaneous Raman spectrum of this rubrene crystal with the incident p polarized 785 nm excitation normal to the ab plane with prominent peaks indicated by the dashed lines. The inset shows a representative rubrene crystal image under the microscope used for our FSRS studies. The scale bar is 0.4 mm in length.

We tried FSR measurements on both platelet and needle crystals, but were only able to see excited state Raman signatures on needle crystals, possibly due to higher optical density obtained with needle samples. Figure 3.1b shows a ground state spontaneous Raman spectrum of the needle crystal used for FSRS with 785 nm excitation. The intense Raman bands in the 1002 cm^{-1} to 1213 cm^{-1} region correspond to C–H wagging modes and the bands in the 1300 cm^{-1} to 1541 cm^{-1} are assigned to C–C stretching modes in the tetracene backbone of rubrene based

on our DFT calculations.

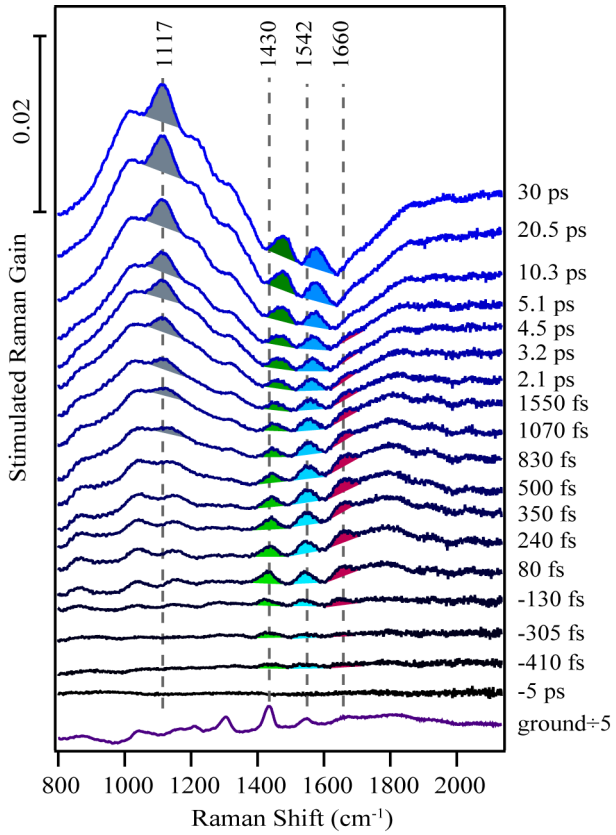

Figure 3.2: FSR spectra of crystalline rubrene at various time delays following photoexcitation. The shaded regions indicate different excited state features during the SF and triplet separation processes. Transient features are seen at Raman shift values of 1117, $\sim$ 1430, $\sim$ 1542 and 1660 cm^{-1}. The features around 1430 and 1542 cm^{-1} shift to higher frequencies with increasing time delay.

We used FSRS to study the excited state structural dynamics during SF and triplet separation in rubrene crystals with an instrumental response function of 250 $\pm$ 2 fs with transmission geometry in an optical microscope. A raw FSR spectrum contains stimulated Raman signals from both the ground and excited states. To obtain only the excited state features, we subtracted the FSR spectra of the ground state taken in the absence of the photoexcitation pump from identical

spectra collected in the presence of the photoexcitation pump. We show the FSR spectra after this one-to-one subtraction in Appendix A Figure A.4. The large depletion of the ground state peaks in the excited state spectra demanded the addition of scaled ground state spectrum, as is customary in FSRS. [89–91] Hence, we added the ground state back to the excited state difference spectra until no depletion of any of the ground state peaks were observed (kinetics shown in Figure A.5, in accordance with previous work [24]), resulting in Figure 3.2. We assign each of the shaded features observed in the time-resolved spectra in Figure 3.2 as peaks and not regions between two valleys after careful evaluation of baseline shape across the full frequency region at all time points, as well as consideration of the transient frequency evolution dynamics which are in agreement with previous ultrafast electronic spectroscopic work. [24] The trace in violet at the bottom of Figure 3.2 is the ground state stimulated Raman spectrum of rubrene scaled by a factor of one fifth. In this work, we focus mainly on the four vibrational peaks in regions around 1117, 1430, 1542 and 1660 cm^{-1}, as indicated by shading.

From Figure 3.2, we observe large frequency shifts of two modes, shaded in green and blue, on picosecond timescale. These modes appear around time zero at frequencies of 1430 and 1542 cm^{-1}, and shift to frequencies of 1478 and 1580 cm^{-1} by 30 ps. The peak around 1660 cm^{-1}, shaded in pink, grows rapidly and decays in intensity on the picosecond timescale. A fourth feature at 1117 cm^{-1}, marked with grey shading, grows in on the picosecond timescale.

Figure 3.3a shows the kinetic fits of the amplitude for the features around 1117, 1430, 1542 and 1660 cm^{-1}, and Figure 3.3b shows the kinetic fits of the peak frequencies for the bands around 1430 and 1542 cm^{-1}. Table 3.1 summarizes

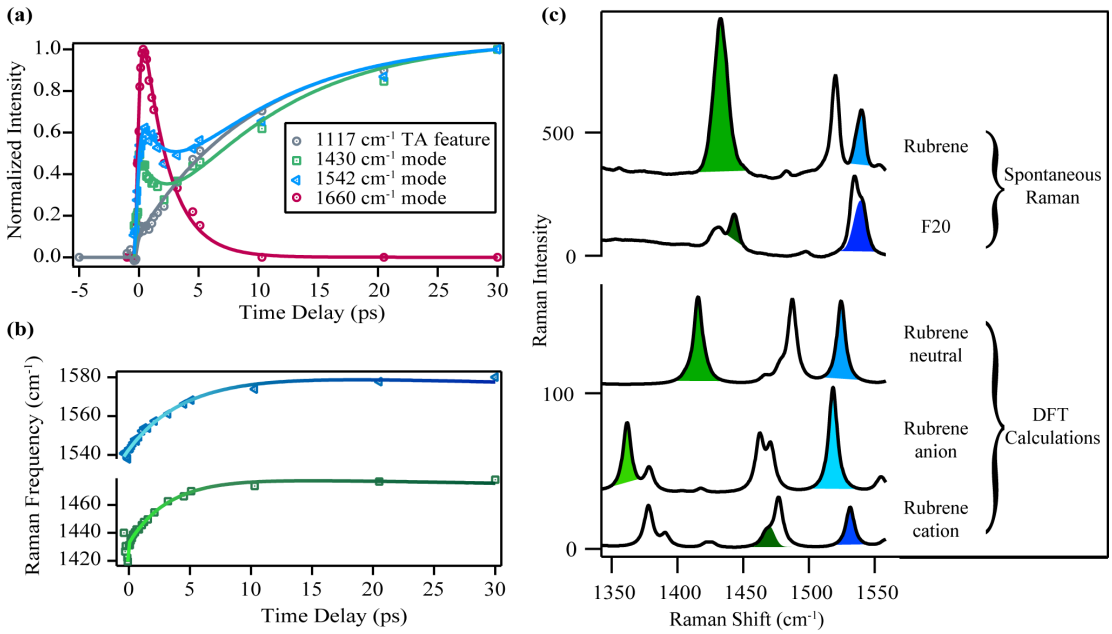

Figure 3.3: Time resolved kinetics of vibrational modes and transient features in crystalline rubrene. The markers represent the raw data obtained from the spectral fitting and the solid lines indicate the exponential fits. (a) Raman amplitude of vibrational modes and transient absorption (TA) feature of rubrene crystal. (b) Transient Raman frequency shifts. (c) Comparison of spontaneous Raman and DFT calculations examining effects of charge density changes on vibrational frequencies. Shades of green represent the shift of the 1430 cm^{-1} mode while the shades of blue represent that of the 1542 cm^{-1} mode in cation, anion and neutral form of rubrene.

the time constants associated with the kinetic fits. An additional time constant of tens of nanoseconds, corresponding to the triplet lifetime, was held constant to fit the amplitude dynamics of the 1117, 1430 and 1542 cm^{-1} features. We see that the band around 1660 cm^{-1} grows in amplitude within 240 $\pm$ 44 fs and decays within 2.2 ps. This band is absent in the ground state spectrum, which indicates it as an excited state, transient intermediate feature. A 2D ES study reported that the correlated triplet pair, ^{1}(TT) in rubrene single crystal attains

Table 3.1: Time constants obtained from the exponential fits of TA feature and mode-specific Raman amplitudes and frequencies. Time constants without errors are held in the fitting.

Raman and TA	Amplitude			Raman Frequency
Feature (cm^{-1})	τ_1 (fs)	τ_2 (ps)	τ_3 (ps)	Shift τ_4 (ps)
1660	240 ± 44	2.2 ± 0.2		
1430	240	2.2	9.9	3.3 ± 0.2
1542	240	2.2	9.9	4.5 ± 0.3
1117 (877 nm TA)			9.9 ± 0.8	

its maximum population within 20 fs and then undergoes vibrational relaxation until 2 ps, when triplet separation begins. [24] Thus, we assign the 1660 cm^{-1} feature to that of the correlated triplet pair, ^{1}(TT). Therefore, we conclude that structural evolution after 2 ps provides information about the mechanism of triplet pair separation. In this chapter, we are focused on monitoring the dynamics after the correlated triplet pair is formed followed by its separation into two triplets, as we do not have the time resolution required to monitor the kinetics before the formation of the correlated triplet pair. We also observe that the kinetics of the feature around 1117 cm^{-1} grows within 9.9 ± 0.8 ps and has a long lifetime. The transient absorption (TA) data for the rubrene crystal, in the absence of the Raman pump, shows a similar narrow feature at 877 nm from Figure A.6, which is indicative of an excited state absorption. This TA peak corresponds to the 1117 cm^{-1} feature in the FSRS data in Figure 3.2. Thus, we assign the 1117 cm^{-1} feature to a transient absorption signature of the separated triplet states in accordance with previous reports. [71]

Interestingly, the two modes at 1430 and 1542 cm^{-1} undergo spectral evolution in the first several picoseconds following photoexcitation. We observe both the

modes shift to higher frequencies by more than 26 cm^{-1} by 5 ps. Two possible explanations for a blue shift of frequency in the ultrafast vibrational spectra can be either vibrational cooling or structural rearrangement. [85, 89, 92, 93] Vibrational cooling is accompanied with increasing vibrational frequency and decreasing vibrational linewidth. However, we do not see any decrease in the linewidth of the peaks (Figure A.7). Additionally, vibrational cooling is not expected to be significant given that we are exciting on the red edge of the absorption spectrum. This implies that the blue shift in the frequencies of the 1430 and 1542 cm^{-1} modes must be due to structural rearrangement in the excited state.

The ground state spectrum of rubrene has peaks at 1434 and 1545 cm^{-1}, which correspond to the C–C stretching and C–H wagging motions in the tetracene core of rubrene. Our DFT calculations support these mode assignments. The excited state spectra show similar features at 1430 and 1542 cm^{-1} at time zero. This suggests that these two bands at time zero are associated with the tetracene core vibrational motions. Since the two bands at 1430 and 1542 cm^{-1} shift in frequency in the first several picoseconds after photoexcitation, the shift in frequency must be associated with structural rearrangement of the tetracene core during the triplet separation process. One possibility for these dramatic frequency shifts is a change of electron density in the tetracene moiety of the molecule.

To test the hypothesis that changes in the electron density of the tetracene core cause the frequency shifts observed in the transient Raman spectra, we performed spontaneous Raman measurements on a fluorinated rubrene to see how the fluorine substitution affects the vibrational frequencies of the tetracene core.

We used F_{20} rubrene, in which all hydrogens on the four phenyl rings are replaced with fluorine, as a mimic for a system with reduced electron density in the tetracene core due to the presence of the electronegative fluorine atoms. [88] We plot spontaneous Raman measurements on the powder form of both rubrene and F_{20} rubrene in Figure 3.3c. To prove that the difference between powder and crystalline states has no effect on the high energy vibrational frequencies, we measured the spontaneous Raman spectrum obtained from rubrene single crystal, rubrene powder and rubrene solution in chloroform and plotted them in Figure A.10. Since we do not see any change in the high energy frequencies between the three samples, it is safe to assume that the effect of fluorine atoms in F_{20} on the tetracene core will be the same in solution, powder, or crystalline form. From Figure 3.3c, we observe that the vibrational modes at 1434 and 1541 cm^{-1} in rubrene increase in frequency in F_{20} rubrene to 1444 and 1543 cm^{-1}, respectively. The 1541 cm^{-1} mode shifts in frequency by 2 cm^{-1} while going from rubrene to F_{20} rubrene, and this frequency difference is significant given that we are able to resolve peaks separated by 1 cm^{-1} due to the high signal to noise ratio from our samples. The shift in the two vibrational modes are in the same direction as the shifts seen in the transient FSR spectra. Thus, we infer that the blue shift in the frequencies observed in the FSR data could be caused by removal of electron density from the tetracene core.

To provide further support to the idea that the tetracene core loses some charge density during triplet separation, we compared the experimental Raman frequencies to DFT calculations. Although DFT cannot tractably calculate the complex

Table 3.2: Experimental Raman frequencies for rubrene and F_{20} rubrene, and calculated vibrational frequencies for neutral, anionic and cationic rubrene

Mode Description	Spontaneous Raman Frequencies(cm^{-1})		DFT Frequencies (cm^{-1})		
	Rubrene	F_{20}	Neutral	Anion	Cation
Terminal C=C stretch in tetracene core and C–H wagging	1434	1444	1416	1362	1467
C–H scissoring and C=C stretch in tetracene core	1541	1543	1524	1518	1531

nature of SF due to the need to include a number of interacting excited state potential energy surfaces, it is quite accurate for vibrational frequency calculations. Although the isolated single molecule used for these calculations cannot accurately model any exciton delocalization or band structure of the rubrene molecular crystal, previous work on rubrene has shown that vibrational frequency calculations at single molecule level do rigorously match experimental vibrational frequencies of rubrene crystals. [94] We optimized and calculated the vibrational frequencies at B3LYP/6-311+G(d,p) level of ground singlet state rubrene in neutral, cationic and anionic form and plotted the scaled vibrational frequencies by a factor of 0.967 [95] in Figure 3.3c. The relevant vibrational modes are color-coded, with gradients of the same color representing the same normal modes. Table 3.2 summarizes the experimental and calculated frequencies along with the corresponding vibrational mode descriptions. The calculated vibrational frequencies of neutral rubrene are in good agreement with the experimental values, with a maximum deviation of 1.3% for the 1434 and 1541 cm^{-1} modes localized on the tetracene core. Importantly, DFT calculations show that the mode at 1416 cm^{-1} in neutral

rubrene shifts to 1362 cm^{-1} in the anion and 1467 cm^{-1} in the cation. Similar frequency shifts are seen for the 1524 cm^{-1} mode between the charged and non-charged rubrene species. These shifts are in agreement with our hypothesis that the FSRS measurements report on a reduction in electron density in the tetracene core during triplet separation.

Therefore, we conclude that the blue shift in frequencies during triplet separation in rubrene is accompanied by the removal of electron density from the tetracene core. The electron density removed from the tetracene backbone might go into the phenyls, or to another neighboring rubrene molecule, which may be off-resonant with our Raman probing process. The present work does not provide sufficient support for either of these pathways, as the phenyl ring vibrational motions as well as Raman features from off-resonant species are too low in amplitude to be observed in these measurements.

Figure 3.4 depicts a schematic illustration of the structural dynamics occurring during SF in rubrene. Upon photoexcitation, the system goes to ^{1}(TT) state within the 250 fs time resolution of our experiment. This state is associated with a unique Raman peak at 1660 cm^{-1}, and lives for 2.2 ps. The FSRS measurements reveal unique structural changes on the 3–4 ps timescale associated with rearrangement of electron density in the tetracene backbone, followed by formation of the triplet state in 9.9 ps. The large frequency shifts observed here prove that the electron density is removed from the tetracene backbone prior to formation of the triplet state, indicating that structural derivatives of rubrene which facilitate similar changes in electron density may lead to increased rates or yields of triplet separation. Fortunately, synthetic methodologies for facile generation

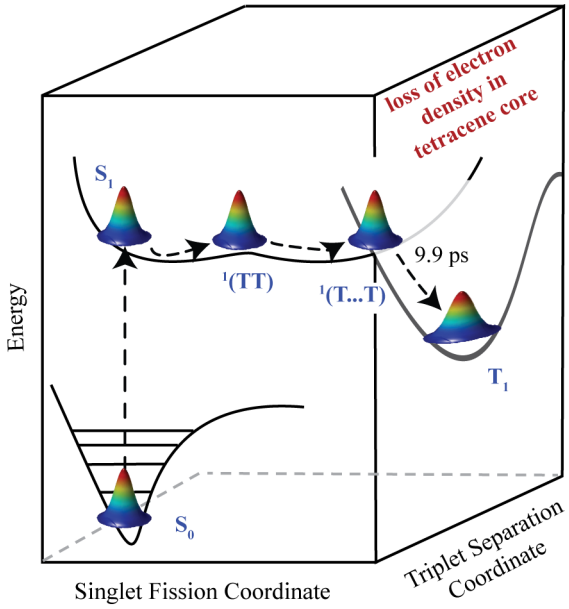

Figure 3.4: Potential energy surfaces participating in triplet generation and separation in rubrene during SF.

of fluorinated and isotopically-substituted rubrenes exist and will enable further investigation into the mechanism of SF in organic materials. [88, 96–99]

3.5 Conclusions

In summary, we have used FSR microscopy to study the structural dynamics associated with SF and triplet separation in crystalline rubrene. By using a structurally-sensitive technique we are able to map out some of the nuclear coordinates associated with the triplet separation process in SF. We observe significant vibrational frequency blueshifts of two vibrational modes due to the structural rearrangement occurring during separation of the correlated triplet pair. These

results, along with ground state DFT calculations and spontaneous Raman measurements of a rubrene derivative with highly electronegative phenyl rings, indicate that a decrease in the electron density over the tetracene backbone in rubrene is associated with triplet separation. This work provides insights into the structural changes that assist in the separation of the correlated triplet pair and is a step towards understanding structural evolution during SF in organic crystalline materials. Given that the loss of electron density is associated with separation of the correlated pair, this opens up the possibility for designing rubrene derivatives with appropriate substituents capable of undergoing efficient triplet separation, thereby leading to more efficient photovoltaic devices. Fabricating new materials with molecular structures that could aid in efficient triplet separation and transport should enable the widespread adoption of SF materials for efficient light harvesting.

3.6 Acknowledgements

This work is supported by National Science Foundation, CHE-1552849 and DMR-1006566. The authors thank Professor James Johns for use of the furnace for rubrene crystals growth, Billy Ogden and Zhuoran Zhang for the F_{20} rubrene sample, and Soumen Ghosh and Dr. Ruchira Silva for helpful discussions on calculations. The authors also acknowledge the Minnesota Supercomputing Institute (MSI) at the University of Minnesota for providing resources that contributed to the research reported in this paper.

Chapter 4

Femtosecond Stimulated Raman Spectroscopy - Guided Screening Leads to Efficient Singlet Fission in Rubrene Derivatives

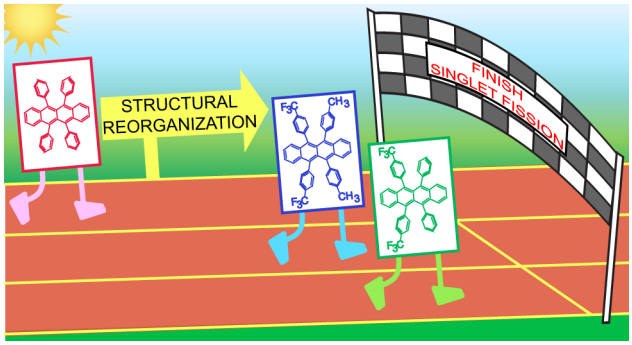

4.1 Overview

Chromophores undergoing singlet fission are promising candidates for harnessing solar energy as they can generate a pair of charge carriers by the absorption of one photon. However, photovoltaic devices employing singlet fission is still lacking as practical applications due to the limitations within the existing molecules undergoing singlet fission. Chemical modifications to acenes can lead to efficient singlet fission devices, but the influence of changes to molecular structure on the rate of singlet fission is challenging to model and predict. Using femtosecond stimulated Raman spectroscopy we have previously demonstrated that the triplet separation process during singlet fission in crystalline rubrene is associated with the loss of electron density from its tetracene core. Based on this knowledge, we have screened new rubrene derivatives with electron withdrawing substituents to prime the molecules for efficient singlet fission, without impacting their crystal packing. Our rationally screened crystalline chromophores exhibit significantly improved singlet fission rates - an order of magnitude higher. This study demonstrates the utility and strength of a structurally sensitive spectroscopic technique in providing insights to spectroscopy-guided materials selection and design guidelines that go beyond energy arguments to design new singlet fission-capable chromophores.

4.2 Introduction

Converting solar energy into electrical energy with photovoltaic devices is a renewable and clean pathway to manage global energy need and environmental

challenges. However, the theoretical efficiency of solar energy conversion to electrical energy for a single p-n junction solar cell is limited to $\sim 34\%$ as calculated by Shockley and Queisser. [1] Although, this limit takes into account the energy losses due to fill factor and charge recombination, the largest reason for this limit is due to spectral losses. Currently, solar cell technologies are dominated by silicon. [100] Photons that have an energy below the bandgap of silicon (and other light absorbing materials) will not be absorbed by the photovoltaic device. When an incident photon is higher in energy than the bandgap of silicon, only one electron-hole pair is generated from the absorbed photon and the extra energy after the absorption of the higher energy photon is lost as heat, known as thermalization. A strategy to overcome these spectral losses is to manufacture semiconductors based on organic molecules that can better utilize the solar spectrum by increasing the charge per photon ratio. One such process is singlet fission, where one photon is used to generate two triplet excitons, leading to external quantum efficiency exceeding 100%. [6, 101]

Singlet fission (SF) is a multi-exciton generation process where a high energy singlet exciton is converted into two low-lying triplet excitons, that are initially coupled as an overall singlet state. Therefore, SF generates two charge carriers at the expense of a single photon through a spin-allowed ultrafast process. SF is an energetic down-conversion process that utilizes the shorter wavelength photons to minimize thermalization losses, thereby expanding the spectral window for light harvesting and generating multiple charge carriers. [6, 12] Customized organic chromophores undergoing SF have the ability to push the boundary of photovoltaic power conversion efficiency from 34% to 45% and thus has inspired new methods

to fabricate photovoltaic devices. [2, 9] However, solar cells based on SF have yet to deliver on this promise, with observed power conversion efficiency maximum of only 5.1% due to energy loss mechanisms. [4] Therefore, we need strategic material design models for advancing compounds capable of undergoing SF to achieve efficiency much closer to the theoretically modelled limit.

The major obstacle in the development of SF devices is the scarcity of materials capable of undergoing SF with near unit efficiency while also being solution processible, photochemically stable and possessing large extinction coefficients. [3, 102] This lack of materials is partly due to the limited knowledge about the molecular design principles to develop tunable SF-capable systems, resulting in slow and unproductive trial-and-error approaches. Computational-guided design is challenging due to difficulty in modelling the complex multiexcitonic states with several different crossing potential energy surfaces and spins. Also, the photophysics of the SF process is not fully understood and much debated. The small number of applicable SF chromophores, where multiple theoretical models could explain the mechanism, limits our understanding. The only way to reach a consensus is by examining a wider set of materials. Thus, the primary interest in this field has been to understand the photophysical mechanism of SF with the aim of rationally designing materials to increase the commercial viability of SF. Examples of rationally selecting materials, particularly congeners of molecules known for SF properties, are exceptionally rare.

Ultrafast spectroscopic measurements have demonstrated that SF is a multistep process comprising of an excited singlet exciton S_1 converting into a distinct

intermediate of a neighboring pair of triplets coupled with an overall singlet character, called correlated triplet pair $^1(T_1T_1)$, [13,25,62,103–105] undergoing subsequent loss of the electronic coherence to form $^1(T_1...T_1)$ and finally spin relaxation leading to two individual isolated triplets T_1. [16,17,25,36,105–108] In order to be fast on sub-100 fs timescale, SF needs to be isoergic or slightly exoergic, and this requires the first excited singlet energy to be close to twice the energy of the lowest-lying triplet state. In addition to the electronic energy criteria, the electronic coupling between the neighboring molecules in the solid state must be considered. In order to design materials undergoing efficient and rapid SF, crystal packing needs to be optimized. Many experimental and theoretical studies have focused on the connection between electronic and vibronic couplings with SF dynamics to design systems for highly efficient SF process. [10, 11, 17, 26, 67, 103, 106, 109–111] However, the relationship between SF efficiency and molecular structure is challenging to explore, and correlations between the molecular structural changes and its effects on the SF rates and yields remain unclear. Thus, there is a need to construct a comprehensive set of measurement-guided design protocols based on the structural dynamic studies on known SF molecules to develop principles for the synthesis or selection of new and more efficient SF systems.

To address the above-mentioned challenges about rational designing of materials guided by spectroscopic measurements, we couple prior vibrational spectroscopic knowledge and synthetic protocols to identify and screen potential candidates for SF. Although transient absorption spectroscopy is the most popular technique to quantify and demonstrate singlet fission, obtaining direct structural information using this technique can be challenging. Vibrational spectroscopies are

compelling probes because they can directly probe nuclear motions, thereby monitoring the structural changes in molecules undergoing singlet fission. We have previously investigated the structural evolution in crystalline rubrene, the tetraphenyl tetracene derivative shown in Figure 4.1a, during SF with femtosecond stimulated Raman spectroscopy (FSRS). Rubrene is one of the most studied organic semiconductors because of its unique optoelectronic properties, such as high charge carrier mobility and long exciton diffusion lengths, [75, 77, 112, 113] and the fact that it undergoes efficient SF in its crystalline orthorhombic form. [24, 71–73, 76, 114–116] Early studies established that SF is the most prominent decay path of the excited singlet excitons in crystalline rubrene, [71, 75, 76] where the correlated triplet pair is formed within 20 fs and has a lifetime of 2 ps before separating into two individual triplets. [24]

A large number of rubrene congeners have been crystallized, and even more have been synthesized. Limiting a Chemical Abstract Search (SciFinder) to substituted 5,6,11,12-tetraphenyltetracenes (rubrene) revealed over 350 structures with the 5,6,11,12-tetraaryltetracene core. [117] Limiting the candidates to those proven by X-Ray crystallography to adopt conformations and solid-state packing similar to orthorhombic rubrene reduces the number of candidates by an order of magnitude, but still provides a daunting number of candidates. One of us has developed syntheses that allow for late-stage diversification of the rubrene structure; [96] new compounds of this class can be readily prepared by a variety of methods. [118–121] Without predictive structural and mechanistic models however, selecting candidates to study SF from this library of rubrenes amounts to 'guess-and-check' work. The prospect of proposing the synthesis of new rubrenes

for SF is similarly guesswork. Ideally, a model for the structural and electronic changes involved in rubrene's SF process would select optimal candidates from the pool of known rubrene structures and aid in the design of new targets for synthesis.

We previously conducted a study highlighting the changes in the molecular structure of rubrene during the SF process. [48] FSRS is an ultrafast vibrational spectroscopic technique that is used to investigate the structural dynamics in a chemical reaction by monitoring the vibrational modes of the system with high temporal and spectral resolution. [80–85] Our FSRS measurements indicated that the separation of the correlated triplet pair into two individual triplets is accompanied with the loss of electron density from the tetracene core in crystalline rubrene. [48] Building off on our crystalline rubrene FSR spectral analysis and interpretation during SF, here we hypothesize that rubrene derivatives with reduced amount of electron density in the tetracene core will facilitate the triplet separation process faster, which will be experimentally manifested as smaller extent of structural reorganization in the FSR data of the derivatives.

Assessing this hypothesis requires a system in which the electron density over the tetracene backbone in parent rubrene can be controlled, for example by introducing substituents in the peripheral phenyl groups in rubrene moiety. Fortunately, Douglas and co-workers have previously engineered and characterized a series of rubrene derivatives with the electron withdrawing CF_3 substituent. [88,96] In this work we study two potential candidates for SF from the database of synthesized rubrene derivatives by Douglas and co-workers: di-CF_3 di-CH_3 rubrene (FM-rubrene) and di-CF_3 rubrene (F-rubrene), where the functional groups are

on the para position of the phenyl rings as shown in Figure 4.1. [96] The presence of electron withdrawing groups in the phenyl rings reduces the electron density over the tetracene core in the rubrene derivatives, which is in accordance with the criteria to test our proposition.

Comparing rubrene with the FM-rubrene and F-rubrene derivatives, the substitution has little impact on the crystal packing and the electronic energy of the crystalline excited states. FM-rubrene and F-rubrene have comparable electronic state energies to that of rubrene, indicating that SF should occur in both derivatives. [122] Although these rubrene derivatives have not been previously investigated for SF experimentally, thin films of these derivatives have been shown to have longer exciton diffusion length as compared to rubrene, indicating enhanced electronic coupling, a desirable property for optoelectronics and SF. [123] The tetracene core in FM-rubrene and F-rubrene is planar and the π-stacking packing motif of rubrene is maintained in crystals of these derivatives, demonstrating that there is little change in packing between the rubrene analogues. Computational studies on FM-rubrene and F-rubrene showed an increased wave function overlap due to the noncovalent interactions provided by substituents, which leads to large favorable electronic couplings of the excited states for SF. [122] Thus, we selectively chose FM-rubrene and F-rubrene based on the energetics of their orbitals and their similarity in the crystal packing with rubrene, which indicates that SF should occur in both FM-rubrene and F-rubrene. We used crystals of rubrene, FM-rubrene and F-rubrene rather than thin films due to the controlled morphology available with crystal growth which is important to study singlet fission. In this investigation, we aim to establish the practical applicability of

spectroscopy-guided screening to identify and provide synthetic designing principles for chromophores with efficient SF properties that go beyond the simple energy arguments.

4.3 Methods

4.3.1 Sample Preparation

We grew crystalline rubrene via a physical vapor deposition (PVT) method. [48] Briefly, we used 16 mg of rubrene powder, $\geq$ 98% purity from Sigma Aldrich in the PVT furnace with Ar gas flowing at the rate of 100 ml/min. We heated the source region in the furnace to 330°C using a thermocouple for 35 minutes and obtained 4-6 mm long needle-shaped orange colored rubrene crystals at a distance of 5–8 cm away from the source region.

We obtained the raw material of FM-rubrene and F-rubrene powder from McGarry et al. [96] to grow their single crystals via slow solvent evaporation method. We dissolved the raw powder in a minimum amount of CH_2Cl_2 and layered the top of the solution with isopropanol in the ratio of 1:4 CH_2Cl_2:isopropanol and left it standing at room temperature under nitrogen gas environment until crystals had formed. We obtained 2–3 mm long and wide, plate-shaped, red-colored FM-rubrene and F-rubrene crystals. We separately mounted each of the crystals used in this work onto a 1 mm thick glass microscope slide and sealed them with a glass coverslip and glue.

4.3.2 UV-Vis spectroscopy

We obtained the absorption spectra of rubrene, FM-rubrene and F-rubrene crystals using UV2600 UV-Vis spectrophotometer by Shimadzu in transmission mode. We plot the normalized steady-state absorption spectra of crystalline rubrene, FM-rubrene and F-rubrene along with the respective crystal image as seen under the microscope for our FSRS studies in Figure B.1. The absorption spectrum of a rubrene single crystal shows four absorbance maximum at 438, 464, 497 and 536 nm, FM-rubrene single crystal shows the absorbance maxima at 442, 468, 500 and 560 nm and F-rubrene crystal peaks at 466, 510, 531 and 557 nm. The poor resolution of the peaks in F-rubrene crystal is due to the smaller crystallite size. The estimated crystal thickness of rubrene is $\sim$ 1–2 µm, FM-rubrene and F-rubrene are $\sim$ 30–40 µm.

4.3.3 Continuous wave Raman spectra

We obtained the spontaneous Raman spectra of rubrene, FM-rubrene and F-rubrene crystals using a home-built Raman spectrometer. We sent a 785 nm laser through an inverted Olympus IX 73 microscope and focused it onto the samples through a 10x Olympus objective. The power of the laser at the sample was 90 mW and we collected the Raman signal in a transmission geometry using a Princeton Instruments 2500i spectrograph and a Princeton Instruments PIXIS 100BX CCD array.

4.3.4 Femtosecond stimulated Raman spectroscopy

We measured time-resolved FSRS experiments on our home-built optical setup, described elsewhere. [47, 48, 79, 124, 125] Briefly, we used the fundamental output of 4.6 W at 800 nm from a 1 kHz repetition rate Ti:Sapphire regenerative amplifier (Coherent model Libra-F-1K-HE-110) to generate the Raman pump, Raman probe and actinic pulses for the FSRS experiments. We used two different setups to generate Raman pump pulses for the experiments presented in this chapter. We used a custom grating filter to generate the Raman pump pulse by sending 480 mW of the fundamental output through the grating filter to generate a 2.1 ps Raman pump pulse for rubrene FSRS data. We also passed 450 mW of the fundamental output through a custom etalon (TecOptics) to produce a 4 ps narrowband Raman pump pulse centered at 807 nm for FM-rubrene and F-rubrene FSRS studies. We then passed these pulses through an optical chopper synced with the laser repetition rate to block every other Raman pump pulse.

We focused 2.5 mW of the 800 nm fundamental output through a 2 mm sapphire crystal to generate a white light continuum as the Raman probe. We passed the continuum through an 830 nm long-pass filter to block the residual 800 nm output. We then compressed the pulses with a fused silica prism pair to generate the femtosecond broadband Raman probe. We set the path length of the Raman pump pulse and Raman probe pulse to be the same and overlapped them temporally for the FSR measurements.

We used a home-built non-collinear optical parametric amplification (NOPA) system to generate the actinic pulse. We generated the white light seed continuum in a 2 mm thick sapphire crystal and used a BBO crystal to generate the

400 nm pulse by frequency doubling the 800 nm fundamental output. In our NOPA set-up, we mixed the white light continuum and the doubled fundamental pump pulse in a 1 mm BBO mixing crystal. We then passed the generated visible pulse through a newly installed pulse shaper (Fastlite Dazzler^{TM}) and an SF10 prism pair compressor for compression and dispersion compensation to generate the actinic pulse. To collect time-resolved data, we used an actinic pulse with a central wavelength of 536 nm and full-width half maximum of 14 nm for crystalline rubrene and a 533 nm actinic pulse with 10 nm full-width half maximum for crystalline FM-rubrene and F-rubrene, shown in Figure B.2. We performed the time-resolved experiments on different days with different alignments, which resulted in slightly different actinic pulse central wavelength. We used a newly installed pulse shaper (Fastlite Dazzler^{TM}) and an SF10 prism pair compressor for compression and dispersion compensation in the actinic pulse for the FM-rubrene and F-rubrene FSR measurements.

We sent all the three pulses to the sample through an inverted Olympus IX 73 microscope and focused the Raman pump, Raman probe and actinic pump pulse collinearly onto the sample using a 6 cm focal length lens and used a condenser (Olympus IX2-LWUCD, NA 0.55) to collimate the Raman probe pulse to the detector. The laser beams are normal to the *ab* plane in rubrene and FM-rubrene, and *ac* plane in F-rubrene crystals. We controlled the time delay between the actinic pulse and the Raman probe pulse using a piezoelectric delay stage (Thorlabs, DDS220). We measured the cross-correlation of the actinic pump and Raman probe pulses to be 120 $\pm$ 2 fs with 533 nm actinic pump pulse for FM-rubrene and F-rubrene studies and 250 $\pm$ 2 fs with 536 nm actinic pump pulse

for rubrene FSR measurements by the optical Kerr effect with a 2 mm cuvette of cyclohexane. The better cross-correlation for the FM-rubrene and F-rubrene measurements is attributed to better compression of the actinic pulse by the newly mounted pulse shaper (Dazzler), which was absent for the rubrene studies. For all measurements, we used a 10 cm lens to focus the stimulated Raman signal and the probe onto a 1/3 meter spectrograph and a Princeton Instruments PIXIS 100F CCD array to collect the Raman spectra with an acquisition rate of 1 kHz. We used a customized LabVIEW program to obtain the femtosecond stimulated Raman gain spectra by collecting the ratio of the Raman probe spectra with the Raman pump on and the Raman pump off. Given the high signal to noise ratio in our FSR data, we can resolve changes in frequency less than 2 cm^{-1} apart.

In this study, we use previously published results for crystalline rubrene [48] and have broadened the set of chromophores examined here to provide new insights for molecular structure designing guidelines to obtain more efficient SF systems for their use in optoelectronics.

4.3.5 Computational calculations

We optimized the ground state geometries (S_0) with flat conformation of rubrene, FM-rubrene and F-rubrene in the gas-phase using density functional theory (DFT) with B3LYP functional and 6-31g(d,p) basis set on Gaussian 16 (version C.01) program package. [96, 126] We computed the harmonic vibrational frequencies of the optimized geometries to confirm a minimum without any imaginary frequency had been reached. We performed the natural bond orbital (NBO) analysis at B3LYP/6-31g(d,p) level using NBO 3.1 program implemented in the

Gaussian 16 package to compare the charge distribution in ground singlet state of rubrene, FM-rubrene and F-rubrene. We optimized the lowest-energy triplet state geometries (T_1) of all three molecules by DFT at the (U)B3LYP/6-31g(d,p) level of theory in gas-phase single molecule.

4.4 Results & Discussions

To investigate the effect of reduced electron density in the tetracene backbone of rubrene on SF dynamics while keeping the crystallographic parameters similar, we rationally selected FM-rubrene and F-rubrene for this study. We present the crystallographic parameters of rubrene, FM-rubrene and F-rubrene in Table 4.1 demonstrating that the three motifs pack quite similarly in crystals. [123] We overlaid the dimers of rubrene and its analogues from the crystallographic data in Figure 4.1a to show that there exists minimal change in the crystallographic packing between all three of them, so any difference observed in SF dynamics is only due to the changed electron density in the tetracene core. We plot the steady-state absorption spectra of rubrene, FM-rubrene and F-rubrene in Figure B.1, which depicts clear vibronic signatures in all the crystalline systems.

Table 4.1: Crystallographic parameters of rubrene, FM-rubrene and F-rubrene, where *a*, *b* and *c* are the lattice parameters and *d* is the intermolecular spacing.

	Lattice	a (Å)	b (Å)	c (Å)	d (Å)
rubrene	orthorhombic	26.79	14.21	7.17	5.46
FM-rubrene	orthorhombic	34.14	14.05	7.14	5.89
F-rubrene	orthorhombic	31.18	14.21	7.12	5.73

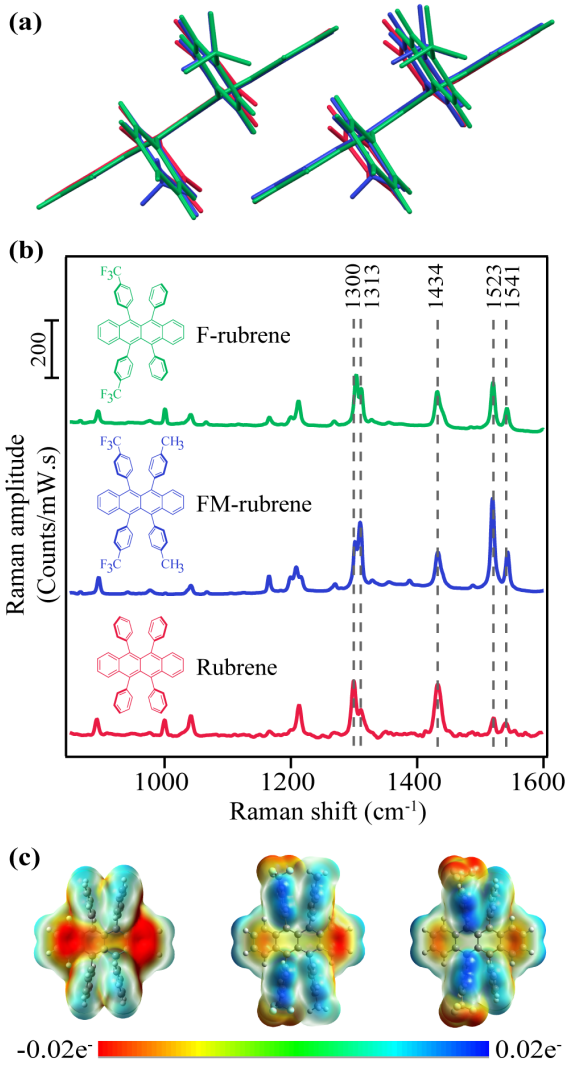

Figure 4.1: (a) Overlaid dimers from crystallographic data of rubrene, FM-rubrene and F-rubrene demonstrating the similarity in crystallographic packing between the three organic molecular crystals. (b) Molecular structure of rubrene, FM-rubrene and F-rubrene along with the spontaneous Raman spectra in their crystalline form with a 785 nm p-polarized excitation. (c) Electrostatic potential (ESP) plot in rubrene, FM-rubrene and F-rubrene from our DFT calculations. Red depicts high electron density and blue depicts low density.

We collected ground state spontaneous Raman spectra of crystalline rubrene, FM-rubrene and F-rubrene with a 785 nm excitation to probe the effect of chemical substitution on the vibrational modes and present it in Figure 4.1b. All three moieties possess the same vibrational modes in the fingerprint region. We have labeled select Raman modes in Figure 4.1b between 1300 – 1541 cm^{-1}, which correspond to C–C stretching and C–H wagging motions in the tetracene core of all the three molecules, based on our DFT frequency calculations.

Since the structural rearrangement observed during SF in crystalline rubrene was previously established to be associated with the loss of electron density in the tetracene core, [48] we aimed to quantify the effect of the electron withdrawing groups on the charge distribution in the tetracene core within the rubrene derivatives. We performed natural bond orbital (NBO) analysis on the optimized ground state singlet geometries of rubrene, FM-rubrene and F-rubrene. The natural charges from the NBO population analysis on the tetracene backbone in rubrene, FM-rubrene and F-rubrene are 0 e^-, 0.012 e^- and 0.016 e^- respectively. These values indicate that the tetracene core in rubrene has the most electron density followed by FM-rubrene and then F-rubrene. To visually inspect this charge distribution over the rubrene series, we display the electrostatic potential (ESP) maps in Figure 4.1c. The ESP plot shows the density of electrons within a molecule on a surface that encompasses the molecule. Red depicts high electron density and blue depicts low density. Based on the ESP plots, we observe that the negative ESP is localized more on the tetracene backbone in rubrene, followed by FM-rubrene and then F-rubrene. The ESP maps along with NBO analysis demonstrates that the electron density over the tetracene backbone is reduced

while going from rubrene to FM-rubrene and to F-rubrene.

Although the rubrene series have similar crystallographic packing and ground state vibrational bands, the key difference between these three molecules is the tetracene core electron density. This indicates the importance of studying excited state dynamics where the transient spectral changes between the three can be significant and those spectral differences can be attributed as the function of the tetracene core electron density. Based on our aforementioned hypothesis and the electron density distribution calculations, we here predict that F-rubrene should undergo the least structural rearrangement and thus the fastest SF rate.

To test our prediction, we used time-resolved FSRS to examine the excited state structural evolution during SF and triplet separation process in crystalline rubrene and rubrene derivatives. We compare these newly measured derivatives to the previously published experimental data of crystalline rubrene. [48] A raw FSR spectrum contains contributions from both the ground state and excited state features. Thus, to extract only the excited state information, we subtracted the FSR spectra collected in the ground state without the actinic pulse from the spectra collected at a given time delay after photoexcitation with the actinic pulse. We present this one-to-one subtracted FSR data of crystalline rubrene, FM-rubrene and F-rubrene in Figure B.3. We observe large bleach features of the ground state modes in the excited state spectra due to the fact that there are fewer molecules in the ground state after photoexcitation. These bleach features in the excited state spectra required the addition of a scaled ground state spectra to be able to extract features exclusive to the excited states. Therefore, we added fraction of the ground state spectrum back to the excited state spectra until ground

state bleach was no longer observed (kinetics shown in Figure B.4) for rubrene, FM-rubrene and F-rubrene FSR data in Figure 4.2.

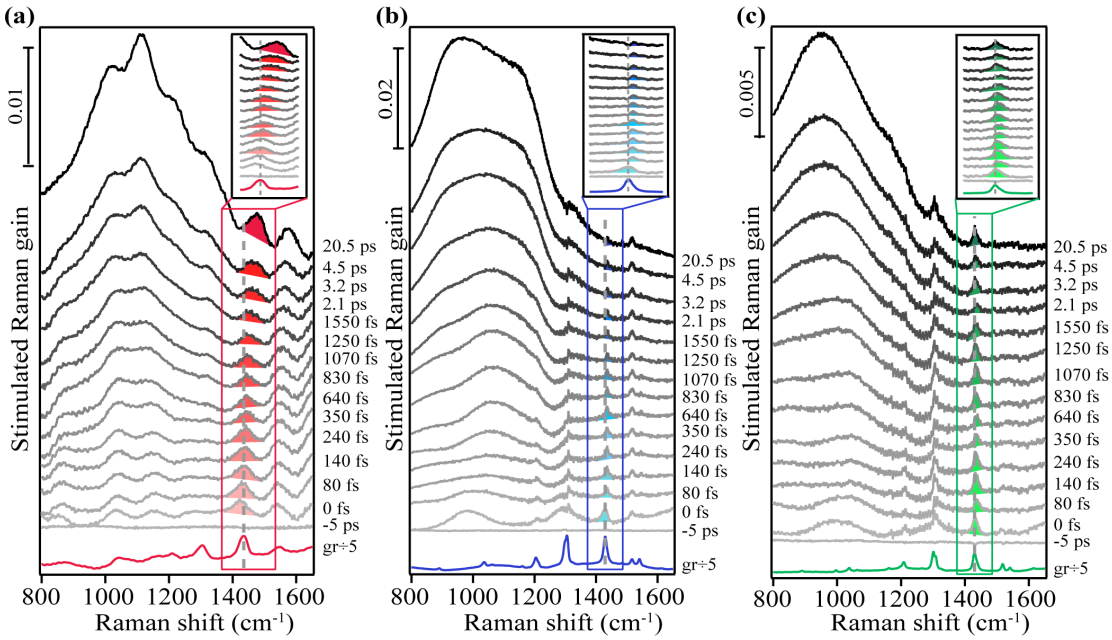

Figure 4.2: Femtosecond stimulated Raman spectra of crystalline (a) rubrene, (b) FM-rubrene and (c) F-rubrene. Shaded regions highlight the transient Raman spectral evolution after photoexcitation for the 1430 cm^{-1} mode. Inset shows the zoomed in profile of the solid boxed region to aid the visualization of the small frequency shifts.

We used a grating filter as the source to generate the Raman pump pulse for the FSR data of rubrene in Figure 4.2a and an etalon as the source for the FSR data of FM-rubrene and F-rubrene in Figure 4.2b and 4.2c, which lead to differences in the linewidths between the measurements. As a control, we collected the FSR data of crystalline FM-rubrene using the grating filter as the source to generate Raman pump pulse (Figure B.5, B.6 and B.7) and we observe similar excited state dynamics as we observe with the etalon. Therefore, we can confidently compare the three data sets presented in Figure 4.2 to understand how the dynamics of

SF and triplet separation process differ among the rubrene derivatives. While the excited state dynamics in FM-rubrene are similar using grating filter and etalon-derived Raman pump pulses, we continued using the etalon system to study the excited state dynamics in F-rubrene because the etalon provides better spectral resolution, necessary here to observe small changes in vibrational frequencies. The traces at the bottom of the three data sets in Figure 4.2 correspond to the ground state stimulated Raman spectrum of crystalline rubrene, FM-rubrene and F-rubrene, each scaled by a factor of 1/5 for clear pictorial representation. In this study we mainly focus on the broad features below 1200 cm^{-1} and the shaded region vibrational peaks around 1430 cm^{-1} in all three crystals.

From Figure 4.2, we observe broad long-lived features below 1200 cm^{-1} region in the FSR data of crystalline rubrene, FM-rubrene and F-rubrene. From our previous FSR study on crystalline rubrene we assigned this broad feature to an electronic signature of the separated triplets during the SF process by comparing the dynamics of this broad feature with the transient absorption data in rubrene (Figure B.8). [48] Interestingly, the FSR data of crystalline FM-rubrene and F-rubrene in Figure 4.2b and 4.2c also display broad long-lived features below 1200 cm^{-1}. We observe similar broad features in the transient absorption data for crystalline FM-rubrene and F-rubrene in Figure B.8, which is indicative of excited state absorption. Since rubrene does not undergo SF in solution, [71] as a control we measured the transient absorption data of FM-rubrene in solution, presented in Figure B.9. We do not witness these broad long-lived features in the transient absorption data of FM-rubrene solution as seen in its crystalline counterpart. This

implies that the origin of those broad long-lived features in FSR spectra of FM-rubrene and F-rubrene are similar to the long-lived triplet states in crystalline rubrene. Given that the energetics of the electronic states in FM-rubrene and F-rubrene satisfy the energy criteria for SF [122] and the similarity of spectral dynamics between rubrene and the derivatives, we believe that FM-rubrene and F-rubrene undergo SF and form long-lived triplets. Therefore, we assigned these broad long-lived spectral features to electronic transient absorption signatures of the separated triplets generated through the SF process in FM-rubrene and F-rubrene.

In addition to triplet features, we observe that the Raman mode shaded in red for crystalline rubrene FSR data in Figure 4.2a undergoes a spectral evolution with a time constant of 3.3 ± 0.2 ps. This mode appears at a frequency of 1430 cm^{-1} around time zero and then blueshifts to a frequency of 1462 cm^{-1} by 3 ps as shown in Figure 4.3a. In ultrafast spectroscopy, a shift in vibrational mode implies a structural rearrangement. [85, 89, 92, 93] Since the time constant associated with the frequency shift of the 1430 cm^{-1} mode is longer than the 2 ps correlated triplet pair lifetime in crystalline rubrene, [24] we previously assigned this structural evolution to dynamics during the triplet pair separation ^{1}(T...T). [48]

The 1430 cm^{-1} mode in the ground state Raman spectrum of rubrene corresponds to C–C stretching and C–H wagging motions of the tetracene core in rubrene. Since the 1430 cm^{-1} vibrational mode blueshifts after photoexcitation, the shift in frequency we observe in the excited state spectra is associated with the structural rearrangement of the tetracene core during the triplet separation process in crystalline rubrene. We previously assigned this spectral evolution of

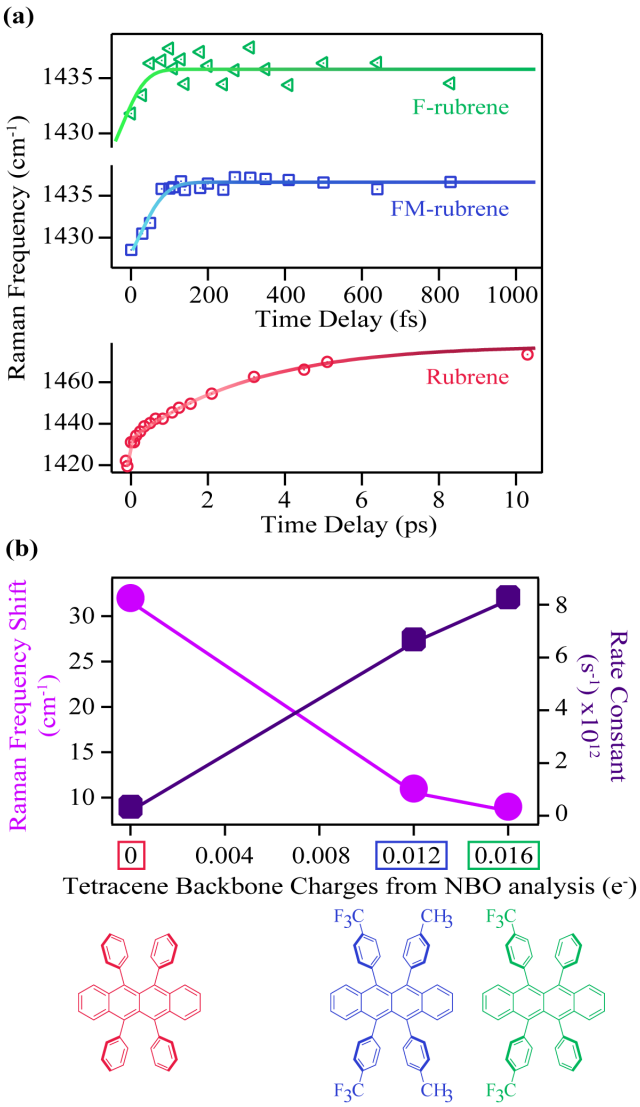

Figure 4.3: (a) Transient Raman frequency evolution of the mode around 1430 cm^{-1} at time zero in crystalline rubrene, FM-rubrene and F-rubrene upon photoexcitation. Error bars are contained within the markers. (b) The corresponding total shift in the 1430 cm^{-1} Raman band position in the three molecules and the associated rate constants as a function of the total charge on the tetracene backbone from NBO population analysis.

the 1430 cm^{-1} to higher frequencies to be accompanied by the loss of electron density in the tetracene backbone during the correlated triplet pair separation into two individual triplets in crystalline rubrene. [48] Therefore, we expect a correlation between the structural rearrangement during the correlated triplet pair separation and the frequency shift along the rubrene series: the smaller the structural rearrangement, the smaller the frequency shift, and the less energy lost during the whole fission process. Since FM-rubrene and F-rubrene have less electron density in their tetracene core than rubrene, we expect to observe smaller and faster frequency shifts in the vibrational mode in the derivatives compared to rubrene, where F-rubrene is expected to be the fastest to separate the correlated triplet pair into individual triplets.

Excitingly, we obtained similar behavior of the frequency evolution for the 1430 cm^{-1} vibrational mode in crystals of FM-rubrene and F-rubrene as observed in crystalline rubrene, as shown in the FSR data in Figure 4.2b and 4.2c respectively. To extract information on the transient evolution of the Raman vibration, we fit the Raman mode around 1430 cm^{-1} at different time delays after photoexcitation with a Gaussian spectral function. We notice that the intensity evolution of the 1430 cm^{-1} mode is different within the three crystals and this difference in intensity evolution of the 1430 cm^{-1} mode is due to differences in the resonance conditions of the excited states in the three derivatives. We plot the dynamics of this fitted peak frequency as a function of time for rubrene, FM-rubrene and F-rubrene in Figure 4.3a. The experimental error bars for the frequency fits are contained within the markers. We fit the spectral peak frequencies to a biexponential decay convoluted with the cross-correlation between the actinic pulse and

the Raman probe to obtain the kinetics. We have propagated the error in the instrument response function during the deconvolution process and obtained the time constants (τ_1) associated with the kinetic fits for rubrene, FM-rubrene and F-rubrene as 3.3 $\pm$ 0.2 ps, 150 $\pm$ 20 fs and 120 $\pm$ 40 fs, respectively. The time constants of the spectral evolution for FM-rubrene and F-rubrene approaches our instrumental response function of 120 $\pm$ 2 fs in the experiments. A time constant of tens of nanoseconds, corresponding to long-lived triplets, was held constant to fit the transient spectral evolution of the feature around 1430 cm^{-1}. Using the time constants from the kinetic fits, we quantify that the 1430 cm^{-1} at time zero displays a shift of $\sim$ 32 cm^{-1} by 3 ps in rubrene, $\sim$ 11 cm^{-1} by 150 fs in FM-rubrene and $\sim$ 9 cm^{-1} in less than 120 fs in F-rubrene. Within error, the time constants for FM-rubrene and F-rubrene are not significantly different. However, we have measured multiple F-rubrene and FM-rubrene crystals, and in all cases, we observe faster dynamics in F-rubrene compared to that in FM-rubrene. Thus, the trend of frequency shift and the associated time constants is qualitatively followed where F-rubrene displays a smaller frequency shift on a relatively faster time scale than FM-rubrene.

The stimulated Raman signal obtained by employing a broadband Raman pump and a narrowband Raman pulse offers a high spectral resolution of vibrational features and information on the time dependent vibrational frequencies integrated over the dephasing vibrational time. The signal observed in FSRS experiments do not represent instantaneous vibrational frequencies present in the sample only at the moment when the probe arrives, but the signal comprises of

all the vibrational frequencies present in the sample over the course of the vibrational dephasing time. [127, 128]. This means that the FSRS spectrum obtained at a time point of 100 fs contains information on 100 fs + ΔT, where ΔT is the vibrational dephasing time convoluted with the Raman pump pulse. The center peak frequencies observed experimentally at the early time points in our FSRS data in Figure 3.3a are not the instantaneous frequencies. However, the relative shifts of the 1430 cm^{-1} mode in the fluorinated rubrene derivatives, while small, are reproducible across samples and thus qualitatively holds true.

The frequency upshifts observed in Figure 4.3a are not intuitively correlated with bond stiffening or weakening. However, based on our previous computational and experimental studies, we found out that the blue shift is associated with the electron density change after photoexcitation during singlet fission. [48] The amount of frequency shift observed experimentally is related to the extent of structural rearrangement occurring within the molecules during the correlated triplet separation process while undergoing SF. This structural rearrangement is in turn associated with the loss of electron density over the tetracene core in the rubrene series during the loss of electronic coherence of the correlated triplet pair. Thus, to extract the relationship between the electron charge distribution in the ground state of the rubrene series with spectral evolution, we plot the total experimentally observed shift in frequency of the Raman mode around 1430 cm^{-1} from our FSRS data and the rate $(1/\tau_1)$ of this frequency shift as a function of the NBO charges on the tetracene core in the rubrene derivatives in Figure 4.3b. We observe an inverse relationship between the frequency shift and the tetracene backbone being more positive along the rubrene series. We also found a direct

correlation between the rate constant of the frequency shifts with the presence of less electron density between the tetracene cores in rubrene, FM-rubrene and F-rubrene. The rate constant of this frequency shift is proportional to the rate of SF and thus, our results reveal that the FM-rubrene and F-rubrene exhibit SF rates an order of magnitude higher than rubrene, with F-rubrene undergoing slightly faster SF than FM-rubrene. This demonstrates a one-to-one correlation between the charge distribution over tetracene core in the three molecules and the experimentally observed structural rearrangement and rate of triplet pair separation via SF.

To correlate the observed experimental structural reorganization with the molecular structural properties in the rubrene derivatives, we draw attention to our NBO calculations. From the NBO analysis, F-rubrene and FM-rubrene have less electron density in their tetracene core compared to rubrene, and therefore, the derivative structures are closer to their triplet state structures to begin with. Since F-rubrene possess the minimum amount of electron density in its tetracene core among the rubrene series, it displays the smallest frequency shift, and thereby undergoes the least and fastest structural reorganization to form the individual triplets because its ground state structure is pre-primed to that of the final triplet structure. Hence, less energy is lost in restructuring the molecules in F-rubrene while separating the correlated triplet pair, a favorable property for SF as this reduces the thermalization loss. Therefore, we have successfully utilized our spectroscopic knowledge to predict and screen the molecular structure of the rubrene derivatives such that they are pre-deposited to the product structure, which is the triplet structure during SF in this scenario. Additionally, the observed correlation

between the frequency shift and the tetracene core electron density suggests that the electron density shifts away from the tetracene core into the phenyl groups during the separation of correlated triplet pairs in rubrene and its derivatives. This time-resolved study thus provides new insights regarding the directionality of the electron density movements during SF within the rubrene derivatives series.

Figure 4.4 represents a schematic illustration of the structural changes in rubrene, FM-rubrene and F-rubrene during the triplet pair separation process via SF. We graphed the frontier molecular orbitals consisting the highest occupied molecular orbital (HOMO) of the ground singlet state and singly occupied molecular orbital (SOMO) of the triplet state in rubrene, FM-rubrene and F-rubrene obtained from our DFT calculations in Figure 4.4. Analyzing the optimized geometries in the ground singlet and first triplet structures along the rubrene derivatives supports our experimental results that FM-rubrene and F-rubrene undergo less changes in their structures while going from singlet to triplet geometry than rubrene. Also, comparing the molecular orbitals of the SOMO of triplet and HOMO of ground singlet state confirms that the electron density indeed shifts from the tetracene backbone into the edges of the peripheryl phenyl groups during the triplet generation process, as depicted by the curved purple arrows in Figure 4.4. Therefore, the time-resolved studies in partner with the theoretical calculations together support that the electron density moves away from the tetracene core into the side phenyl groups during the separation of the correlated triplet pair in rubrene and its derivatives.

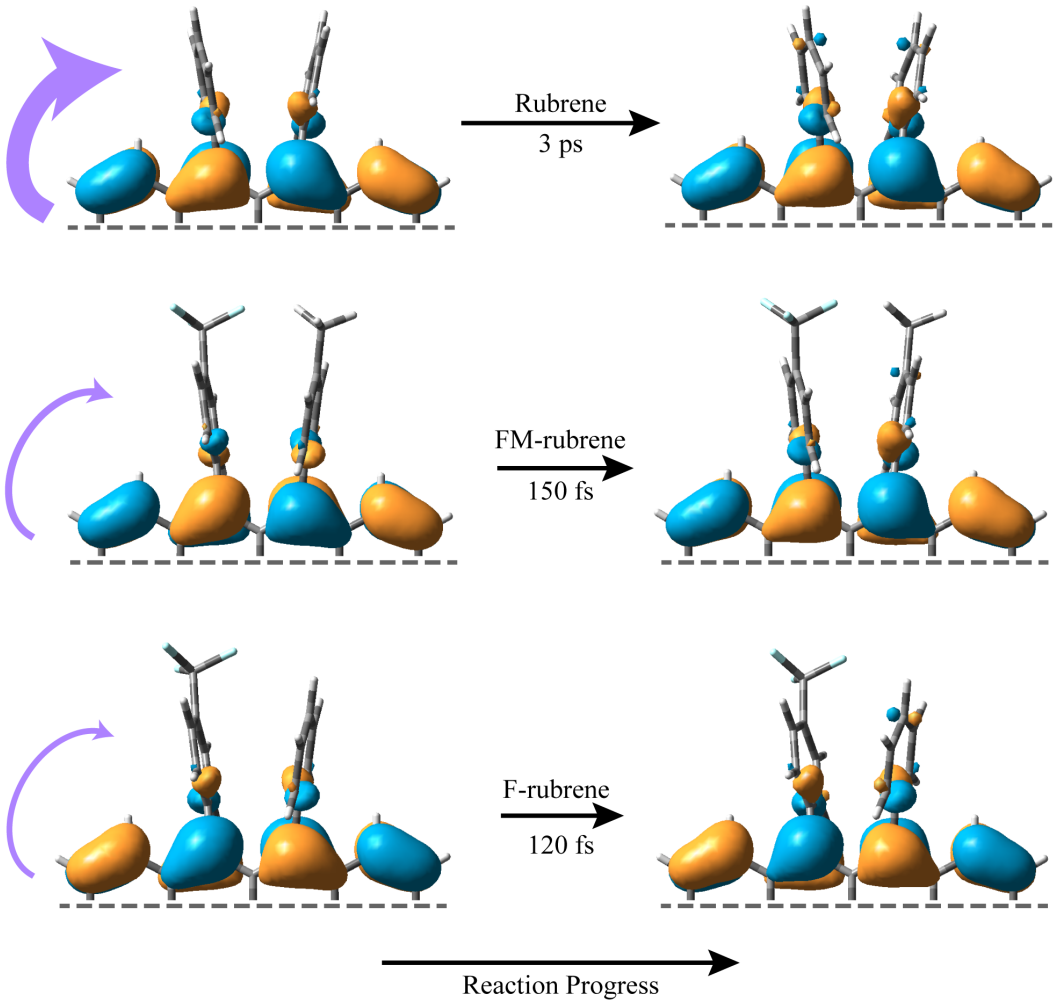

Figure 4.4: Schematic diagram of the frontier molecular orbitals associated with the SF process in rubrene, FM-rubrene and F-rubrene. The HOMO of the ground singlet state is plotted on the left side and the lowest energy SOMO of the triplet states on the right side for each of the molecular systems. The purple curved arrows illustrate the loss of electron density from the tetracene core into the peripheryl phenyl groups during the triplet separation process via SF. The time constants are experimentally obtained from our FSRS data.

In summary, we used the insights gained from FSRS studies about structural changes during SF in crystalline rubrene to screen promising candidates for efficient SF process. We compared the crystal structures and measured spontaneous Raman spectra of rubrene, FM-rubrene and F-rubrene to show their similarities. We then performed FSRS on crystalline rubrene, FM-rubrene and F-rubrene and observed that after the systems absorb light, placing the wavepackets on the excited state Franck-Condon surface, all three chromophores relaxes displaying spectral signatures of long-lived triplets generated via SF. We provide the first ever experimental evidence for these rubrene derivatives to undergo efficient SF. Among the three molecules, F-rubrene displays the fastest rate of SF, which is a favorable property to generate excitons for further harvesting into photovoltaics. Hence, we conclude that we have selected pre-primed molecular structures of rubrene derivatives, guided by spectroscopic data, to undergo more efficient SF. Our results not only define the structural changes within molecules during SF but bridges the gap between spectroscopic results and translating these results to practical application regarding efficient SF systems. This study expands upon our previous spectroscopic knowledge, proving that controlling the electron density in the tetracene core synthetically leads to significant improvement in the SF rate. Moving forward, we plan to explore this spectroscopy-guided experimental control of synthesis with other acene derivatives, particularly those containing electron withdrawing functional groups on the peripheral aryl groups, provided the molecular packing in the crystal remains the same. These studies will help achieve the end goal of utilizing current spectroscopic knowledge to formulate and realize design guidelines for new and efficient SF systems.

4.5 Conclusions

In conclusion, we have successfully used FSRS to understand the effect of chemical modification on SF and our results indicate that both our carefully chosen rubrene derivatives, FM-rubrene and F-rubrene, undergo SF. We observe a shift in the frequency of a vibrational mode during triplet separation process in our time-resolved FSR data, which is associated with the loss of electron density from the tetracene backbone into the peripheryl phenyl groups in crystalline rubrene and its derivatives. By intentionally reducing the electron density over the tetracene core in the rubrene derivatives, we have now designed the system to have a structure which is much closer to the final structure for efficient SF. Thus, we observe less structural reorganization in rubrene derivatives and a faster rate of SF in F-rubrene followed by FM-rubrene compared to parent rubrene. Less structural reordering leads to lower energy losses, thereby reducing thermalization loss mechanism for efficient SF. We have created a predictive model based on spectroscopic techniques for the design and identification of rubrene derivatives that show an order-of-magnitude increase in SF rates. Our work shows that the long-held promise of spectroscopy-informed small molecule design for organic optoelectronic materials can be realized in rubrene-based singlet fission systems. This will inspire spectroscopic measurements-guided intelligent engineering and syntheses of future materials within SF chromophores and other similar families.

4.6 Acknowledgements

This work is supported by Department of Energy DE-SC0018203 and the Doctoral Dissertation Fellowship award from University of Minnesota. The authors thank Dr. Billy Ogden and Dr. Zhuoran Zhang for the crude samples of FM-rubrene and F-rubrene, and Dr. Federico Coppola for helpful discussions on calculations. The authors also acknowledge the Minnesota Supercomputing Institute (MSI) at the University of Minnesota for providing resources that contributed to the research reported in this paper.

Chapter 5

Facile Background Discrimination in Femtosecond Stimulated Raman Spectroscopy using a Dual Frequency Raman Pump Technique

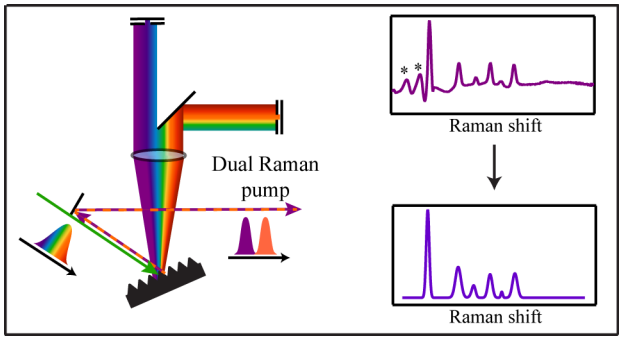

Reprinted with permission from the manuscript by Kajari Bera, Siu Yi Kwang, Alyssa A. Cassabaum, Christopher C. Rich, and Renee R. Frontiera *J. Phys. Chem. A., 2019*, 123 (37), 7932-7939.

5.1 Overview

Femtosecond stimulated Raman spectroscopy (FSRS) is a useful technique for uncovering chemical reaction dynamics by acquiring high resolution Raman spectra with ultrafast time resolution. However, in FSRS it can be challenging to discern Raman features from signals arising from transient absorption and other four-wave mixing pathways. To overcome this difficulty, we combine the principles of shifted excitation Raman difference spectroscopy (SERDS) with a simple fixed frequency comb to perform dual frequency Raman pump FSRS. Through the addition of only two mirrors and a slit to the standard FSRS setup, this method provides Raman spectra at two different excitation wavelengths that can be processed by an automated algorithm to reconstruct the Raman spectrum. Here we demonstrate the utility of dual frequency Raman pump FSRS to easily identify Raman signatures by visual inspection for excited state and ground state spectra, both on and off resonance. We show that previously assigned short-lived vibrations of photoexcited β-carotene are actually not vibrational in nature. We also use crystalline betaine-30 as a challenging test case for this method, as the FSRS spectra contain a number of narrow transient vibronic and non-SRS features. By reliably reducing interference from background signals, the interpretation is substantially more quantitative and enables the future study of new systems, particularly those with small Raman cross sections or solid state samples with narrow vibronic features.

5.2 Introduction

Femtosecond stimulated Raman spectroscopy (FSRS) is an ultrafast vibrational technique that measures the structural evolution of molecular systems in their excited electronic states with high temporal and spectral resolution. [80, 82–85, 89, 90, 92, 93, 129, 130] FSRS uses a short, femtosecond actinic pulse to photoexcite the sample, followed by a narrowband picosecond Raman pump pulse and a broadband femtosecond Raman probe pulse to generate the stimulated Raman signal which monitors the evolution of vibrational modes. The spectral resolution in FSRS is limited by the bandwidth of the narrowband Raman pump pulse with respect to the dephasing time of the vibrational coherences in the system under study. The effective time resolution of the experiment is limited by the width of the Raman probe pulse and the actinic pulse. Over the years, FSRS has emerged as a valuable tool to map out the excited state potential energy surface of photophysical and photochemical phenomena in various systems such as green fluorescent protein, [92] rhodopsin [89], bacteriorhodopsin [91] and many more. [83]

While this technique has found considerable success in providing new physical insights on the structural dynamics of ultrafast photochemical processes, there are experimental challenges that must be overcome in order for it to reach its full potential as a user-friendly analytical tool. A particular challenge for most ultrafast Raman techniques is distinguishing Raman signatures from other nonlinear spectral features arising from transient absorption and other four-wave mixing processes. [131, 132] When either the Raman pump or probe pulse is resonant or

near resonant with an electronic transition, other processes can dominate the apparent FSRS signal. [131] Additionally, distinguishing Raman features from other processes can be complicated in situations in which the excited state lifetime is very short, resulting in broad Raman features due to rapid dephasing, or in molecular crystals, which can have narrowband transient vibronic features due to less heterogeneous broadening.

There have been several previous approaches to background removal in FSRS. Common approaches to FSRS data analysis include higher order polynomial fitting [133–135] and fitting the spectra to a linear combination of spectral basis sets to extract the narrow Raman features from the broad band signal, [136, 137] both of which require significant expertise in fitting and can be subjective. Another technique used in FSRS to reduce interference from undesired signals is by collecting data with two Raman pump pulses that are very close in energy. So far, two methods have been used to produce the Raman pump pulses at two excitation frequencies: one which uses a spatial light modulator [138] and the other which uses a customized chopper based wavelength modulator. [139] However, background correction is not always straightforward, particularly in cases where multiple overlapping resonances are present which can make the baseline difficult to assign. Another approach to obtain background free FSRS data is to use a wavelength modulator in combination with spectral watermarking. [140] In this approach, the experimental data is obtained by collecting the Raman signal at different wavelengths of the Raman pump pulse simultaneously using a pulse shaper and a customized chopper. Although these methods are helpful in

removing background from FSRS data, they add complexity to an already complicated experimental setup, which has constrained their widespread adoption in FSRS. The goal of this work is to present a new and effective method to distinguish transient Raman peaks from other nonlinear spectral features in FSRS using a shifted excitation Raman difference spectroscopy (SERDS) inspired technique with minimal complexity, and no moving parts.

SERDS can successfully remove the fluorescence background in spontaneous Raman spectroscopy, [141–148] and has been effectively applied to FSRS through the use of the two approaches described above. [138–140] SERDS is based on the principle that Raman features are excitation frequency dependent, whereas fluorescence spectra are independent of slight changes in excitation frequency. Therefore, small changes in the excitation wavelength result in equivalent shifts of the Raman peaks, while the fluorescence background remains unchanged. Various specialized light sources have been previously employed for SERDS, such as the external cavity diode laser, [146,149] distributed Bragg reflector (DBR) diode laser, [147] and a monolithic dual-wavelength diode laser at 785 nm. [148,150] By subtracting Raman spectra obtained with two different, but close in frequency ($\sim$ 5 – 10 cm^{-1}) excitation wavelengths, dispersive shaped Raman features are obtained and all other spectral contributions such as fluorescence [146, 151] are removed from the wavelength dependent Raman peaks. [150] A background free Raman spectrum can then be recovered using curve fitting and integration algorithms. [138,141,143,146,147,150,152–155] The choice of reconstruction method is application dependent and can range from being relatively simple to complicated

integration algorithms requiring user intervention to manually specify the limits. [138, 146, 156] Therefore, a simple and straightforward technique is desired to produce an excitation pulse at two wavelengths to distinguish the Raman features from the background.

To more easily produce simultaneous yet spectrally different Raman pump pulses for a SERDS-inspired approach to FSRS, we took inspiration from the work of Kearns et al. who built a simple frequency comb generation setup for vibrational sum frequency generation (VSFG) experiments. [152] To collect two different VSFG spectra simultaneously, Kearns et al. used a pair of mirrors to divide the Ti:Sapphire fundamental output into two visible beams in a grating filter. [152] This simple addition of two mirrors in the grating filter produced two visible pulses that were spectrally separated but spatially and temporally overlapped resulting in two different VSFG signals for multiplex detection. Given that a standard FSRS approach uses a grating filter to generate the picosecond Raman pump pulse, we utilize a similar design here.

In this work, we present a new method to obtain background free FSRS data by combining the principles of SERDS and the experimental approach of frequency comb VSFG. We also benchmark a data analysis approach to remove the background from the ground and excited state Raman spectra and differentiate between Raman and non-Raman features in FSRS. We demonstrate the ease with which we can collect and process background free ground-state and time-resolved FSR spectra applying this method to cyclohexane, 3,3′-diethylthiatricarbocyanine (DTTC) iodide and β-carotene. We also tested the applicability of our experimental design and data analysis to obtain FSR spectra with crystalline betaine-30, a

challenging test system for FSRS due to the existence of very narrow transient vibronic features which can easily be mistaken for Raman signals. This experimental approach can also be used widely for any kind of SERDS measurement, particularly in cases with backgrounds more complex than typical broadband fluorescence spectra.

5.3 Methods

5.3.1 Sample Preparation

We used HPLC grade cyclohexane ($\geq$99.9% purity), HPLC grade methanol and DTTC iodide from Sigma Aldrich as received. We used neat cyclohexane and 1.42 x 10^{-5} M DTTC iodide in methanol in a 2 mm glass cuvette for ground state stimulated Raman experiments. For transient measurements, we dissolved β-carotene (Sigma Aldrich) in HPLC grade cyclohexane and flowed the solution in a 0.5 mm path length flow cell. The optical density of this solution was 0.6 at 500 nm. We dissolved 50 mg of betaine-30 powder (Sigma Aldrich) in 1 mL of HPLC grade methanol (Sigma Aldrich) to grow betaine-30 crystals through slow solvent evaporation. We mounted the crystals onto a glass microscope slide with a piece of double-sided tape for FSR experiments.

5.3.2 Femtosecond stimulated Raman spectroscopy

We performed time-resolved FSRS experiments on our home-built optical setup, described elsewhere. [47, 48, 79] Briefly, we used 4.6 W of the fundamental output at 800 nm from a Coherent model Libra-F-1K-HE-110 femtosecond

1kHz amplifier to generate the three pulse trains used for the FSRS studies. We generated the actinic pulse using a home-built non-collinear optical parametric amplification (NOPA). In our NOPA set-up, we mixed a white light continuum and a doubled fundamental pump pulse in a BBO mixing crystal. For compression and dispersion compensation, we used a pulse shaper (Fastlite Dazzler^{TM}) and an SF10 prism pair compressor. We generated the femtosecond broadband Raman probe by focusing 2.5 mW of the 800 nm fundamental output through a 2 mm sapphire crystal followed by compression with a fused silica prism pair.

To generate the dual frequency Raman pump, we passed 460 mW of the 800 nm fundamental output through our home-built grating filter to generate a 2.1 ps narrowband Raman pump. [82] In our grating filter, the fundamental diffracts off a grating and is then focused onto a slit with a cylindrical lens which selects a portion of the input bandwidth to be reflected back through the lens to the diffraction grating. In order to generate two Raman pump pulses, we inserted a 1 mm thick rectangular silver mirror, shown in bold inside the red dotted box in Figure 5.1a, after the focusing lens, which reflects the red portion of the dispersed input bandwidth onto a second slit and mirror. We used the second slit to select a portion of this spectral bandwidth to generate the second Raman pump pulse, which is reflected back through the lens to the grating as shown in Figure 5.1a. We collected the combined reflections from both mirrors after the grating with a D-shaped pickoff mirror. The output beam consisted of two narrowband pulses separated in wavelength by 1.6–3.0 nm. The two Raman pump pulses are overlapped in space and time at the sample. In order to correct for small differences in the two pathlengths in the grating filter, we added 4.15 mm of glass into one

arm to achieve perfect temporal overlap. We mounted the slits on translational stages to adjust the frequencies required for the two Raman pump pulses. For the data presented in this article, we set the two Raman pump pulse frequencies at 803.1 ± 0.1 and 806.1 ± 0.1 nm for cyclohexane and crystalline betaine-30 FSR experiments and at 802.0 ± 0.1 and 803.6 ± 0.1 nm for DTTC iodide and β-carotene FSR experiments.

An optical chopper synced with the laser repetition rate in the Raman pump line allows for FSRS data collection with the Raman pump pulse on for every other laser shot. Both Raman pump pulses have the same optical path length and pass through the same chopper, which we modulated at 500 Hz. We focused the Raman probe pulse, actinic pulse and Raman pump pulses collinearly onto the sample using a 6 cm focal length lens. To collect time-resolved data, we used an actinic pulse with a central wavelength of 500 nm and full-width half maximum of 9 nm for β-carotene and a 535 nm actinic pulse with 10 nm full-width half maximum for crystalline betaine-30. We used a motorized stage to control the time delay between the actinic pulse and the Raman probe pulse. We focused the stimulated Raman signal and the probe onto a 1/3 meter spectrograph and a Princeton Instruments PIXIS 100F CCD array to collect the data with an acquisition rate of 1 kHz. We wrote a Labview program to obtain the femtosecond stimulated Raman gain spectra by collecting the ratio of the Raman probe spectra with the Raman pump on and the Raman pump off.

5.4 Results & Discussions

We show the modified set-up of our Raman pump pulse generation to obtain pulses that are spectrally separated for an easy SERDS-inspired FSRS system in Figure 5.1a. We generated the Raman pump pulses at two frequencies by the addition of a mirror pair and a slit into our existing grating filter. We call this method dual frequency Raman pump FSRS and its advantages over existing methods are that it is easy to implement, and it produces Raman pump pulses at two frequencies simultaneously. This allows us to switch between the two Raman pump wavelengths without changing any other experimental parameters. Figure 5.1b illustrates the fundamental principle of SERDS, in which Raman features are shifted by known frequencies relative to the two excitation wavelengths, and non-Raman features overlap.

To demonstrate that dual frequency Raman pump FSRS can discriminate Raman peaks from non-Raman peaks and background spectra, we first used this setup to measure the ground state stimulated Raman spectra of cyclohexane. As cyclohexane is a well-known Raman standard, we were able to verify if our technique could effectively isolate Raman peaks from the other signals. Our experimental setup allows us to obtain Raman spectra with two excitation frequencies in a single laser shot, as shown in the Raman spectrum of cyclohexane in Figure 5.2a. The Raman features in cyclohexane show up as double peaks when we plot them with respect to one Raman pump excitation frequency. All other non-Raman features do not show up as double peaks, making this an easy way to isolate Raman features from the rest of the spectrum.

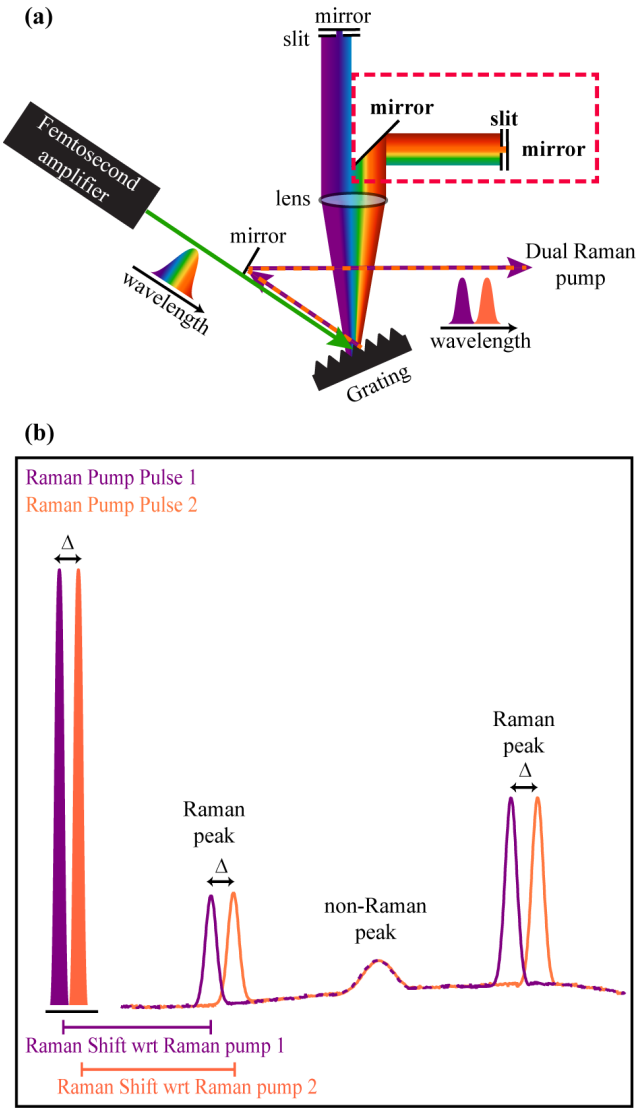

Figure 5.1: (a) Diagram of the modified grating filter setup to generate Raman pump pulses at two wavelengths. A mirror, indicated by the red dashed box, is added to send half of the diffracted light to another mirror-slit pair to generate the second Raman pump pulse. (b) Schematic explaining the principle of SERDS, where the Raman signals shift in frequency upon a shift in the Raman pump excitation wavelength, and the non-Raman signals remain unchanged.

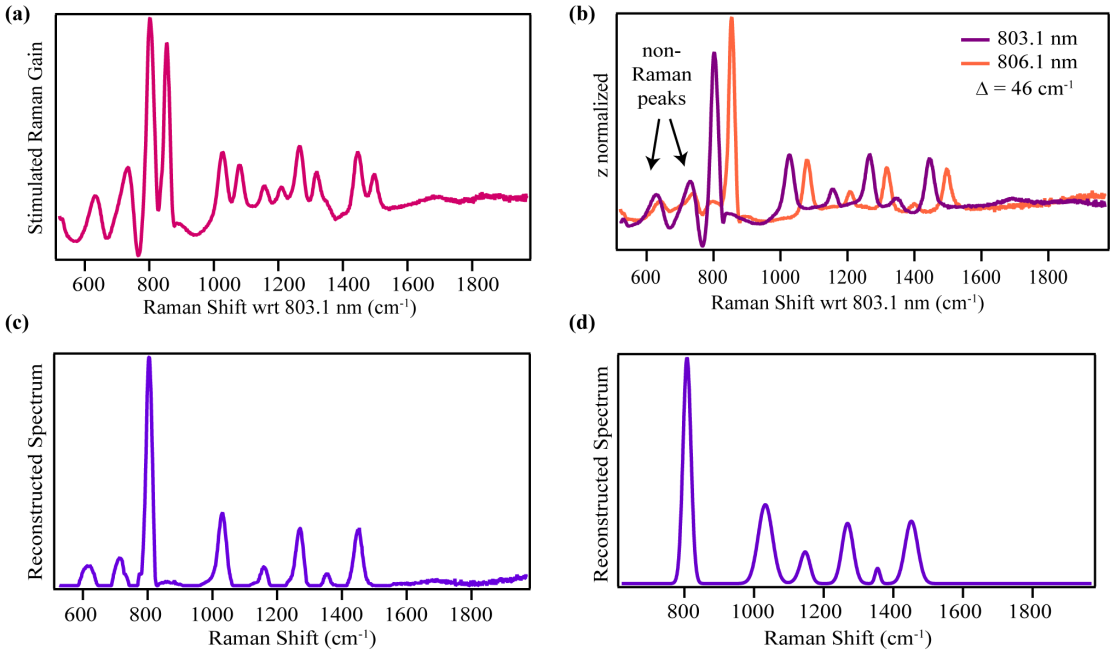

Figure 5.2: (a) Stimulated Raman spectrum of cyclohexane obtained at two Raman excitation frequencies in a single laser shot. (b) Stimulated Raman spectra of cyclohexane obtained at two different Raman pump energies, where the Raman peaks are seen to undergo frequency shifts while the non-Raman peak positions do not change. (c) Raman spectrum of cyclohexane after reconstruction using a previously employed algorithm. [148,154,155] (d) Raman spectrum of cyclohexane after reconstruction using the automated method developed here.

We converted the stimulated Raman spectra of cyclohexane taken separately with the Raman pump pulses at 803.1 nm and 806.1 nm to a common scale through z-normalization [146] so as to make their background spectra similar in Figure 5.2b. Based on the 3 nm difference between the two Raman pump frequencies, the Raman signals taken with the 806.1 nm Raman pump should be upshifted by 46 cm^{-1} (Δ) with respect to the Raman signals taken with the 803.1 nm Raman pump. Comparing the two spectra in Figure 5.2b, we observe that the frequencies of the six Raman peaks of cyclohexane shift by the expected amount.

We can also confirm that the two peaks observed in the 600–800 cm^{-1} region are not Raman peaks as they are independent of the Raman pump wavelength. These non-Raman peaks are likely signatures of cross-phase modulation between the Raman pump and probe pulses. Figures 5.2a and 5.2b illustrate the strength of the dual frequency Raman pump setup to distinguish Raman from non-Raman features in an idealized test sample.

After identifying the Raman peaks from non-Raman peaks using the dual frequency Raman pump setup, our next step involved obtaining a background free Raman spectrum. In Figure 5.2c, we employed a previously used algorithm for SERDS to reconstruct the Raman spectrum of cyclohexane. [148, 154, 155] This reconstruction method has been used exclusively for SERDS with spontaneous Raman spectra and works by computing the summation of two specific difference spectra as shown in the Appendix Table C.1. Although this reconstruction method is able to identify the Raman peaks, it does not eliminate the background completely, and still shows the two spectral features in the 600–800 cm^{-1} region. We have also used other previously-reported reconstruction algorithms [157] with little success (Table C.1), motivating us to seek another approach to reconstruct a cleaner Raman spectrum. Clearly, the stimulated nature of FSRS and the likelihood of spectral features arising from nonlinear processes like cross phase modulation requires a new approach for SERDS data analysis in this application.

To this end, we have developed a reconstruction algorithm that automates the process and identifies regions containing Raman peaks, for which codes are freely available on GitHub. [158] The cyclohexane Raman spectrum regenerated from our method not only retains all the Raman peaks, it also eliminates the

non-Raman peaks and has a zero baseline as shown in Figure 5.2d. To obtain the baseline free Raman spectrum of cyclohexane, we obtained a difference spectrum by subtracting the two Raman spectra in Figure 5.2b, and wrote a program to fit the difference spectrum with a pair of Gaussian functions shifted by Δ. We then retrieved the fits and used them to plot the background free Raman spectrum of cyclohexane in Figure 5.2d. We discuss the steps of our reconstruction method in detail in the Appendix C.

To demonstrate the robustness of our experimental approach, we applied our dual frequency Raman pump technique on DTTC iodide, which is resonant with near-infrared excitation (Figure C.5) and exhibits dispersive lineshapes when near-infrared Raman pulses are used for probing. [131, 159, 160] We show the ground state stimulated Raman spectra of DTTC iodide in methanol obtained with the two Raman pump pulses at 802.0 and 803.6 nm in Figure 5.3. We are clearly able to distinguish Raman peaks from the broad background. For DTTC iodide, we modified our reconstruction algorithm to use a pair of Fano lineshape [161] functions shifted by Δ. Detailed reconstruction procedure is included in Appendix C. We present the reconstructed spectrum of DTTC iodide in Figure 5.3 in blue. This work demonstrates that our dual frequency Raman pump technique is not limited to specific resonance conditions and can be extended to various experimental conditions depending upon the system under study.

We have also applied this experimental approach and automated data analysis technique to time-resolved studies. The introduction of the actinic pulse can give rise to more non-Raman signals, such as a strong transient absorption background, which can make it more challenging to resolve Raman features associated

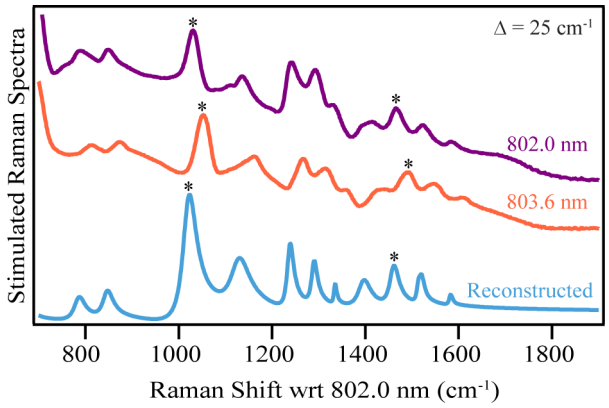

Figure 5.3: Stimulated Raman spectra of DTTC iodide obtained with the two Raman pump excitation frequencies. Reconstructed spectrum from the automated algorithm using dispersive lineshapes is shown in blue color. Peaks marked with *asterisks* are methanol peaks.

with excited state dynamics. Thus, having a technique that can reliably help to distinguish Raman features from non-Raman features is a big improvement. As a test for our approach applied to time-resolved spectra, we carried out dual frequency Raman pump FSRS on β-carotene due to its well-established time-resolved excited state dynamics using FSRS. [5, 135] We collected the excited state FSR spectra of β-carotene, which contains contributions from both the ground and excited states of β-carotene at various time delays after photoexcitation. To extract excited state Raman features, we performed a one-to-one subtraction of the ground state β-carotene spectrum from each excited state spectrum at different time intervals. We show the raw time-resolved FSR spectra of β-carotene measured at Raman pump wavelength of 802.0 nm in Figure 5.4a.

After photoexcitation, we observe ground state bleaching for Raman modes at 1157 and 1524 cm^{-1} due to decreased population of the S_0 state along with an excited state Raman signature of the S_1 peak between 1780–1798 cm^{-1} in

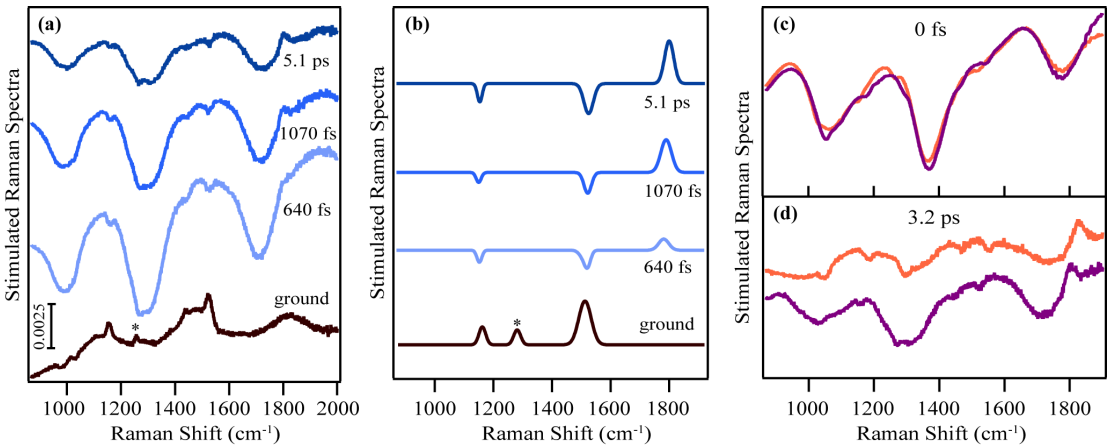

Figure 5.4: (a) FSR spectra of β-carotene at various time intervals after photoexcitation. (b) Reconstructed Raman spectra of β-carotene using our newly developed automated reconstruction method. Asterisks indicate solvent peaks. (c) Excited state Raman spectra obtained at 0 fs after photoexcitation with the two Raman pump frequencies overlaid on one another. (d) Excited state Raman spectra at a much later time point after photoexcitation obtained using two Raman pump pulses.

Figure 5.4a. However, the sharp Raman features are on top of a broad oscillatory background in the excited state data. Using our reconstruction algorithm, we generated background free ground and excited state FSR spectra of β-carotene, as shown in Figure 5.4b.

To provide visual inspection of the distinction between Raman features and non-Raman features, we overlaid the Raman spectra obtained at 0 fs and 3.2 ps after photoexcitation using the two Raman pump pulses at 802.0 and 803.6 nm in Figure 5.4c and 5.4d. We clearly see a shift in frequencies of the ground state bleach modes and the S_1 peak between the different Raman pump frequencies, while the broad background remains the same regardless of the pump frequency.

Previous FSRS studies on β-carotene assigned broad features following photoexcitation to vibrational features on the short-lived second excited singlet state

(S_2) of β-carotene. [135] Due to the sub-100 fs lifetime of this state, the authors opined that any vibrational coherence would not survive state hopping, and vibrational features would be broadened significantly, a very reasonable assumption given the information available. However, the dual frequency Raman pump pulse approach provides new insight into the early time dynamics of β-carotene. As shown in Figure 5.4c, at early time delays we see broad features in the excited state spectra, consistent with previous results. However, when we overlay the Raman spectra obtained with two frequency shifted Raman pump pulses, we see that these broad features do not show a Raman pump frequency dependent shift as would be expected for a vibrational feature. This proves that the broad features observed at early time delays in FSR spectra of β-carotene are not Raman peaks on a short-lived state, but instead are likely electronic features from the S_2 state.

To further test the broad applicability of this experimental technique, we then applied our dual frequency Raman pump FSRS on crystalline betaine-30, a more challenging sample due to its interesting polarization and orientation dependent excited state dynamics and the narrowband excited state features observed in its FSR spectra. [124] The crystal was oriented such that the long axis of the crystal was approximately at an angle of 60° with respect to the probe polarization (Figure C.8). We measured the time-resolved FSR spectra and performed a one-to-one subtraction of the ground state betaine-30 spectrum from each excited state spectrum at different time intervals. We show the excited state spectra of betaine-30 measured at a Raman pump wavelength of 803.1 nm in Figure C.9a. The presence of so many positive features of varying widths on a sloping background makes it difficult to distinguish Raman features from the non-Raman

ones.

To identify the Raman features and remove the sloping background in the excited states, we obtained FSR data of crystalline betaine-30 with Raman pump frequencies at 803.1 nm and 806.1 nm as shown in Figure 5.5. We overlaid each pair of ground and excited state spectra obtained with two Raman pump excitation frequencies to identify the Raman features by visual inspection. FSR spectra obtained at various time delays after photoexcitation collected with the 803.1 nm Raman pump are presented in gradients of purple and that with 806.1 nm are in gradients of orange. The grid lines in Figure 5.5 are spaced by Δ for visual aid to identify the same Raman mode between the two spectra obtained with different Raman pump excitation frequencies for a certain time delay after photoexcitation. Comparing the dual frequency Raman pump data, we identified the Raman features and highlighted a few of them with green dashed lines separated by Δ in the one-to-one subtracted data at 240 fs after photoexcitation in Figure 5.5. Similarly, comparing the FSR data collected with the two Raman pump excitation frequencies for the 240 fs data in Figure 5.5, we observe that the peaks around 910 and 1020 cm^{-1} are not Raman features.

After identifying Raman features from the background, one can use their customary fitting algorithms to reconstruct the excited state FSR data. Here, we used the same algorithm presented in Figure 5.2c and our newly developed automated method to reconstruct the baseline free time-resolved Raman spectra of betaine-30 in Figure C.9b and C.9c, respectively. The reconstructed spectra in Figure C.9b and C.9c clearly have a less prominent background compared to the raw data presented in Figure 5.5a. However, the reconstructed data from both

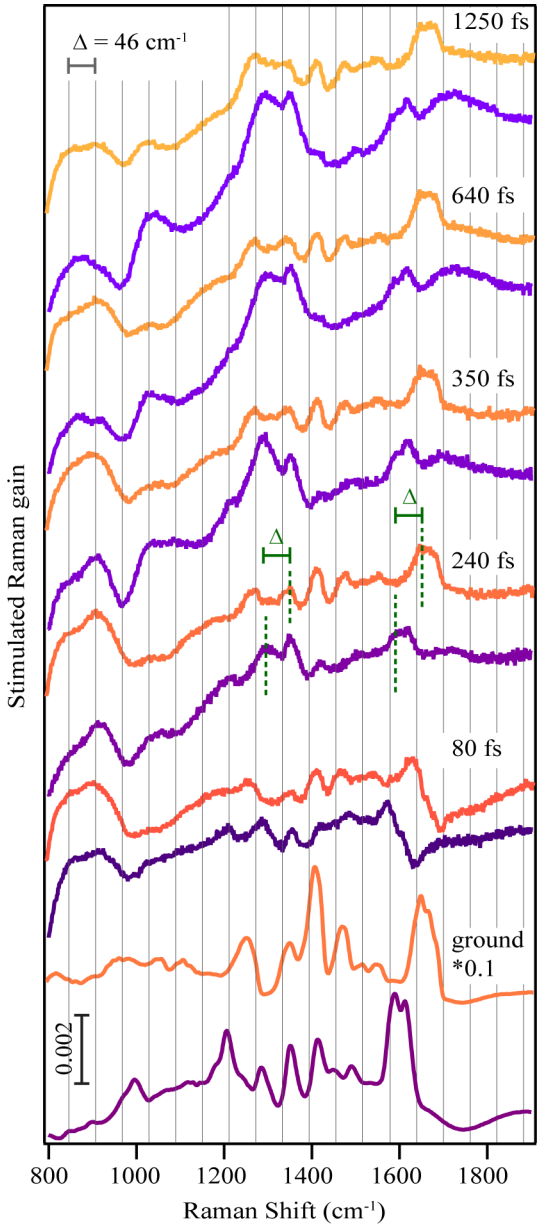

Figure 5.5: FSR spectra of crystalline betaine-30 obtained with two Raman pump excitation frequencies at various time intervals after photoexcitation. The grid lines are separated by Δ and is used for visual aid in identifying the same Raman mode between the pair of spectra at each time delay. The dashed lines in green color in the 240 fs time delay FSR spectra denotes the pair of same Raman mode.

methods still have features that are not Raman signals, such as the broad feature between 1000 – 1150 cm^{-1} marked with an asterisk as deduced from visual inspection of the dual frequency Raman pump data from Figure 5.5. We have discussed the reconstruction of the crystalline betaine-30 time-resolved data more in-depth in Appendix C.

There are limitations to our reconstruction algorithm in terms of excited state FSRS data analysis where it still holds some subjectivity. Our reconstruction method can be used with any lineshape simply by changing the lineshape function in the algorithm, although just as in fitting, prior scientific knowledge about the system is needed to choose the lineshape. We can infer what spectral features might occur in ground state stimulated Raman spectra from spontaneous Raman spectra. However, in the excited state, there is no ground truth and we can only speculate on what vibrations should occur from ground state Raman spectra. Therefore, what excited state Raman features can be determined are dependent on the ability of our algorithm to extract it. Our algorithm has limitations in discriminating excited state Raman peaks in time-resolved spectra but can be used as a rough estimate for a background free excited state Raman spectrum. Our data analysis method would probably work well with solutions as seen with β-carotene, whereas crystals have challenging environments that give rise to maximal artefacts as seen from crystalline betaine-30 data. For crystals and biological samples there is likely no true one-button fitting algorithm for FSRS, as these samples can have their own unique challenges due to the complexity of lineshapes, heterogeneity, variations in dynamics, and electronic signals. Nonetheless, the dual frequency Raman pump technique provides us a simple gateway to inspecting Raman peaks

from a pool of non-Raman features.

Thus, we demonstrated that the SERDS-inspired dual frequency Raman pump FSRS technique is a helpful tool in identifying Raman features from the background and non-Raman features. This experimental approach is economical, simple to implement and is compatible with all kinds of spectroscopies. This method will aid in the analysis of FSRS as well as other complex Raman spectra and is complementary to existing methods.

5.5 Conclusions

In summary, by adding a second arm to our grating filter we have developed this technique, which we call 'dual frequency Raman pump FSRS' to obtain ground and excited state Raman data. We have also developed an automated reconstruction method in order to distinguish Raman features from background features in transient FSR spectra of β-carotene and crystalline-betaine-30. We showed the strength of the dual frequency Raman pump method to differentiate between Raman and non-Raman features in FSRS data, where transient absorption background signals can be overwhelmingly large. We proved that our technique works well for ground state stimulated Raman in systems with various spectral lineshapes and for excited state Raman in solvated systems. Although our technique does not remove all scientific evaluation needed in interpreting FSRS spectra, it serves as a valuable tool to help decipher complex FSRS data, widening the range of systems we can understand through FSRS. This work provides insights into how a simple and economical approach is capable in removing unwanted non-Raman effects from Raman spectra in spontaneous and time-resolved

Raman spectroscopy.

5.6 Acknowledgements

This work is supported by the National Science Foundation, CHE-1552849 (K. B., A. A. C.) and Department of Energy, DE-SC0018203 (S. Y. K., C. C. R.). We thank Amartyajyoti Saha and Dr. David Punihaole for helpful discussions on the reconstruction algorithm.

Chapter 6

Prospects

6.1 Introduction

Organic compounds with semiconducting properties are now moving towards industrial application to fabricate wide ranges of electronic devices. The interest toward these materials is mainly motivated by their mechanical properties, such as flexibility, large-area integration and the possibility to tailor their electronic properties by modifying their molecular structure. The focus of this thesis has been on rubrene, a very promising molecule in the field of organic electronics due to its outstanding charge transport properties and photoconductivity. However, rubrene molecules are less soluble in common organics solvents and are known to be strongly affected by oxidation leading to the formation of epoxide, which hinders the transport and optical properties in its final application for semiconductor devices. Chemically modified rubrenes can lead to improved solubility and stability with unaltered crystal packing and semiconducting properties. Once a derivative is designed and synthesized, a comparison between the arrangement of

the new derivative molecules inside the crystal and the packing motif of the original one is of primary importance to in order to obtain a material whose crystal structure is as similar as possible to the desired one.

This chapter discusses the effort to identify and screen synthesized crystals into different packing classes by compiling and comparing low-frequency Raman spectra in rubrene and rubrene derivatives. It further discusses the excited state dynamics in two rubrene derivatives using FSRS. For the realization of organic semiconductors based devices, the library of organic semiconductors must be expanded. In addition to rubrene derivatives, this chapter presents preliminary studies on the effect of polymorphism to the excited state chemical dynamics in the organic semiconductor, 1,3-diphenylisobenzofuran, which is known to undergo singlet fission and thus has a potential to be employed in singlet fission based devices.

6.2 Crystal Packing through Lattice phonon Raman spectra

In recent years, organic crystalline molecules have been of great interest due to their simple growth procedures and stability at room temperatures making them good candidates for their applications in optoelectronics and photo-driven processes. Organic molecules are employed in photovoltaics, organic transistors, organic light emitting diodes, nonlinear optics and many other electronic applications. Apart from the need of high purity crystals for device fabrication, charge carrier mobilities in the organic semiconductors rely on the interlayer electronic

overlap, which in turn depends on the crystal packing. Therefore, the performance of organic semiconductors-based devices is strongly dependent on the molecular arrangement within the crystal lattice. As a result, slight modification in the crystal structure can lead to different excitonic and transport properties of the charge carriers. As an example, among all the crystal packing forms in rubrene, only the orthorhombic rubrene has been used as an organic semiconductor in organic field effect transistors, [113, 162–165] photovoltaic cells, [166] and light emitting diodes [167–169] due to the presence herringbone packing motif which produces large π-overlap between the interlayers leading to the favorable intermolecular interactions needed for optoelectronics. It is thus necessary to identify optimal crystal packing arrangement for efficient optoelectronics applications because specific molecular packings give rise to efficient charge generation and transport properties.

X-ray diffraction (XRD) is a widely used technique to characterize the crystal and molecular structure of a material. However, methods employing XRD are time-consuming and often destructive. Additionally, XRD requires pristine quality samples with optimum sample thickness, making it harder to analyze a batch of synthesized samples together. In contrast, it is well known that Raman spectroscopy is a non-destructive technique that can be used to identify molecular structure and conformation in situ, and can be complementary to XRD. The low-frequency phonon modes are representative of intermolecular modes within the crystal lattice. Therefore, phonon modes can be used as a probe to determine the crystal structure due to their sensitivity to molecular packing in the crystal. Identifying phonon modes with Raman spectroscopy can provide insights to the

lattice dynamics and possess many advantages over the XRD screening. Acquiring phonon modes using Raman spectroscopy does not need any special sample preparation, and can be used to screen systems in all solid state forms such as powder, thin films, or crystals. Additionally, the acquisition time can be as little as 1 second to obtain the phonon modes for crystal characterization.

Studying lattice phonon modes using Raman spectroscopy is a powerful technique with the capability to characterize crystal structure. Previously, Raman spectroscopy has been used to quantify the purity of crystals and identify various crystalline phases in acenes, such as pentacene, by monitoring the lattice phonon modes. [170, 171] Certain lattice vibrations can be representative of a particular crystal packing system. Specific crystal structures can possess favorable overlaps of the molecular orbitals which can lead to better performing optoelectronic properties. Therefore, examining a series of different crystal structures as a function of molecular structure can help discern the vibrational signatures of different packing arrangements. This will in turn allow for the quick screening and identification of unknown derivatives belonging to the same crystal family using Raman spectroscopy. Compiling the vibrational modes which represents the fingerprint of the individual crystal lattices and comparing the optoelectronic properties between the different crystal structures of the chemically modified derivatives, will help to formulate principles for easy screening of certain crystal packings that are optimal and reproducible for high performing devices. Those derivatives with optimal crystal packing can further be used to test their electronic properties such as charge mobilities for device applications, and is beyond the scope of this thesis.

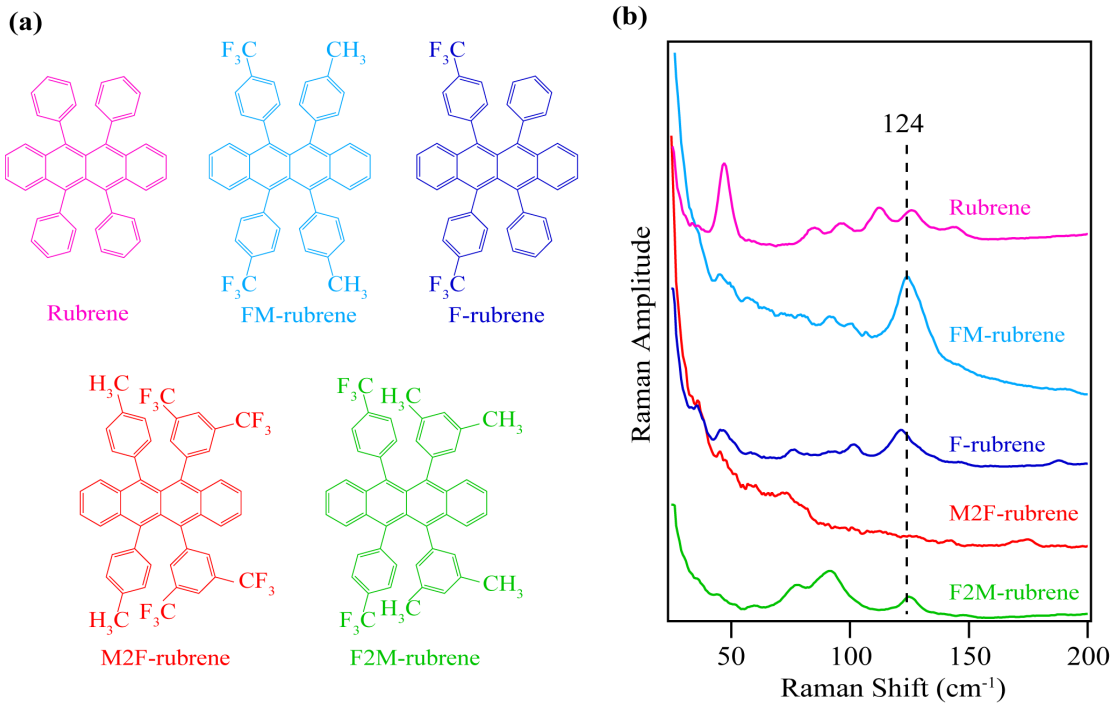

Figure 6.1: (a) Molecular structure of rubrene, FM-rubrene, F-rubrene, M2F-rubrene and F2M-rubrene. (b) Lattice phonon Raman spectra of rubrene derivatives series. The dotted line marks the 124 cm^{-1} twisting mode of the phenyl groups in the orthorhombic structured derivatives.

To this end, I have collected the low-frequency Raman active modes in a series of rubrene derivatives in their powder form: rubrene, FM-rubrene, F-rubrene, M2F-rubrene and F2M-rubrene. The molecular structure of the series of compounds is in Figure 6.1a and their associated low-frequency phonon modes is in Figure 6.1b. All the rubrene derivatives have a planar backbone in their crystalline forms except for M2F-rubrene, where the tetracene backbone is twisted by $\sim 20°$. [88, 96] Rubrene, FM-rubrene, F-rubrene and F2M-rubrene crystallizes in an orthorhombic packing with Cmca, Pbcm, Pnma and Pbcm space groups respectively, whereas M2F-rubrene packs up in a monoclinic ($P2_1/c$) structure.

Comparing the phonon modes in Figure 6.1b, I observe that all the orthorhombic crystal structured derivatives display a Raman mode at $\sim$124 cm^{-1}, which corresponds to the twisting motion of the peripheral phenyl rings from our theoretical calculations. Given that this Raman band is absent in the M2F-rubrene, where the tetracene backbone is twisted and the molecules pack in monoclinic structure, I hypothesize that the presence of the phenyl twisting motion at $\sim$124 cm^{-1} is an indication of a planar backbone and an orthorhombic packing in the rubrene derivatives series, which is the desired crystal packing structure because it is known to display efficient charge generation and transport properties due to the presence of favorable π interactions between the layers in crystals. To confirm this hypothesis, further studies involving more derivatives with and without planar backbone and various crystal structure needs to be explored. A comprehensive study can be performed with a series of other derivatized rubrene substituents such as chlorinated-rubrenes and cyano-substituted rubrenes in the future. Although this preliminary data needs further investigation, this study shows that the phonon Raman spectroscopy indeed can be utilized to screen and identify crystal structures in unknown molecules provided they belong to the similar class of molecules as discussed here.

6.3 Excited State Dynamics in Polymorphs

Organic semiconductors have a potential to compete with silicon-based semiconductors, due to their advantage of flexibility, solution processible, widespread availability and integration. A homogeneous phase is necessary for organic molecules to express better performance as molecular electronics making it crucial to

control the polymorphism during the crystal growth of these organic materials. Polymorphism occurs when molecules in a crystal pack in two or more different forms, and is quite common in organic molecular materials. The intermolecular electronic overlap depends on the molecular arrangement in the crystal and is a key factor in determining the charge carrier mobilities in organic semiconductors. As a result, similar to the effect of different molecular structure, different polymorphs of organic semiconductors have different electrical and optical properties, thereby influencing the device performance to different extent. The presence of polymorphism can induce phase mixing, which can cause disorder and affect the charge transport and mobilities in the organic semiconductors. Even small differences in crystal packing arrangements can lead to changes in the electronic band structure, which can result in different charge transfer integrals in the system, thereby affecting device performance. Therefore, it is necessary to identify and select appropriate polymorphs and understand the role of crystal packing in the charge carrier generation and transport properties.

Although in our previous studies in Chapter 3 and 4, I have used orthorhombic polymorph of rubrene, crystalline rubrene is known to exist in three polymorphic structures as discussed below and in Figure 6.2: [172–174]

1. Orthorhombic: the molecules are arranged in the herringbone packing structure which results in an efficient π stacking.

2. Triclinic: partial π stacking because molecular planes of adjacent molecules are all parallel and laterally shifted with respect to each other.

3. Monoclinic: the adjacent molecules are normal to each other which results in no π stacking.

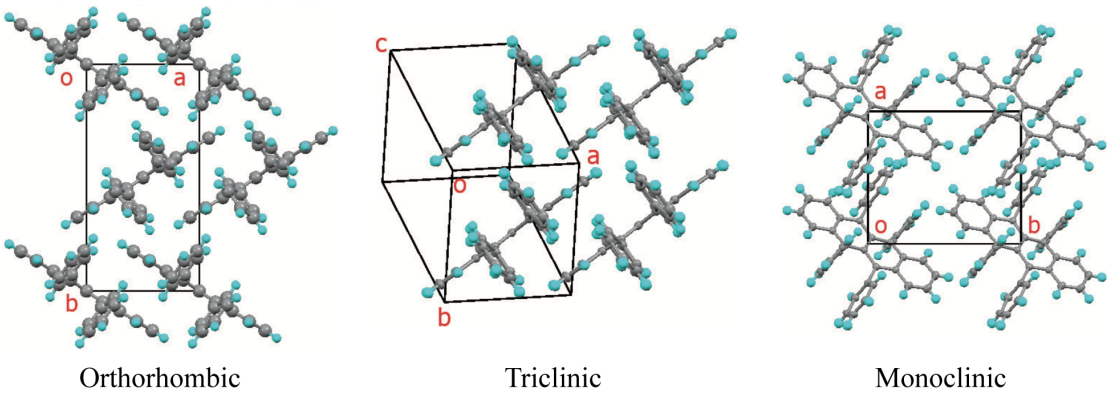

Figure 6.2: Crystal structures of the in orthorhombic, triclinic and monoclinic forms of rubrene. Reproduced after permission from ref [174].

Among the three rubrene polymorphs, the orthorhombic polymorph has been widely studied while very little attention has been given to the other two. This is due to the presence of the efficient π overlap of the orbitals along the direction of the herringbone packing in the orthorhombic polymorph of rubrene, which gives rise to extraordinary semiconducting properties. Crystalline rubrene in its orthorhombic form is known to display long exciton lifetimes (ns-µs) which contributes to their long diffusion length of $\sim$ 4 µm. [75, 77] Orthorhombic rubrene possesses one of the highest charge carrier mobilities ($\sim$ 40 $cm^2V^{-1}s^{-1}$) among organic semiconductors. [175–177] These properties are desirable as they enable the formed excitons to travel longer distances in photovoltaic devices. Due to these properties, orthorhombic rubrene has been used as an organic semiconductor in organic field effect transistors, [113, 162–165] photovoltaic cells, [166] and light emitting diodes. [167–169]

The orthorhombic form of crystalline rubrene has been experimentally proven to undergo efficient singlet fission and thus had been used in our FSRS studies, previously discussed in Chapter 3. However, computational studies by Wang et

al. investigated the excitonic properties in the three rubrene polymorphs and suggested that the energy requirements for singlet fission are better satisfied by the monoclinic form of rubrene than the triclinic and orthorhombic forms. [178] To verify this theory, I aim to identify the rubrene polymorphs and then study the rate of singlet fission in each polymorph using FSRS. This study will guide a better understanding of the nature of intermolecular interactions needed to produce efficient singlet fission.

During polymorphism, although the intramolecular vibrations in different crystal phases are similar or identical, the intermolecular modes are different due to the deformation in the crystal lattice. Therefore, lattice phonon vibrations can be used to probe and identify structures related to different polymorphs. To characterize rubrene polymorphs using Raman spectroscopy, I synthesized the orthorhombic form using physical vapor transport (PVT) method, and monoclinic and triclinic forms of rubrene by a reprecipitation method with a solution mixture of chloroform and methanol. [172] I have plotted the phonon modes in the three polymorphs of crystalline rubrene in Figure 6.3.

I observe distinct lattice vibrations in the three polymorphs in accordance with the literature. [179] These distinct phonon modes can be used to easily screen multiple crystals grown in a large batch of synthesis to identify their crystal packing structure in a short interval of time compared to XRD. The next step would be to use those screened crystals with different polymorphic packing and have them subjected to FSRS experiments. Studying the excited state dynamics in different polymorphs will provide insights about how differences in crystal packing can lead to different dynamic processes and elucidate the role of phonon modes in driving

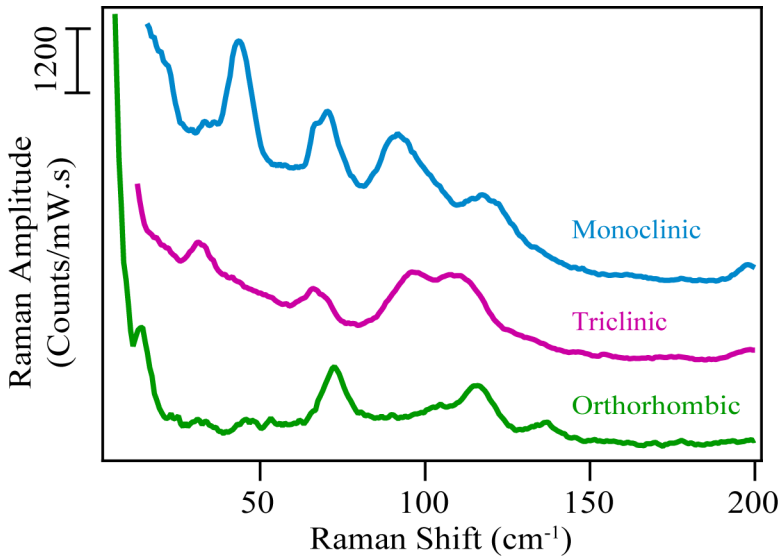

Figure 6.3: The low-frequency Raman spectra of rubrene polymorphs: orthorhombic, triclinic and monoclinic.

different photophysical processes.

6.4 Coherent Control of Excited State Dynamics in Polymorphs

Charge transport and electronic delocalization in organic crystal are determined by the overlap of the molecular orbitals and are highly sensitive to molecular geometry. Therefore, the electronic properties of molecular crystals depend on the interaction of the electronic and the nuclear dynamics in the molecule, termed vibronic coupling. Vibrational motions influence the interactions between different molecular electronic states via intra and intermolecular couplings. This makes vibrational excitation a promising tool for tracking charge transfer processes in

organic crystals for the development of electronic devices. Mode-selective chemistry deals with controlling specific structural changes or chemical reactions by selectively directing energy into specific vibrational modes of a molecule. Being able to control generation of charges and their transport by coherently driving nuclear motions along a pre-selected reaction coordinate will open up numerous avenues to improve performance of electronic devices.

1,3-Diphenylisobenzofuran (DPIB), Figure 6.4a, has a biradical character and is known to have two polymorphs, α and β (Figure 6.4b), which shows completely different triplet yields. [180–182] The α polymorph displays singlet fission with near unity efficiency, [183, 184] while β rapidly forms excimers after photoabsorption and exhibits low triplet yields. Both polymorphs retain the monoclinic crystal form and differ slightly in their lattice parameters. The polymorphs are very similar to each other, and only subtle differences in their structures give rise to the different photophysics observed.

The two polymorphs, α and β, can be obtained from slow evaporation of saturated solutions in various solvents under inert atmosphere. Crystals of the α form can be synthesized by slow evaporation of an acetonitrile solution and the β form can be obtained by slow evaporation of a dichloromethane solution. Figure 6.4c shows an optical image of the efflorescent yellow prisms of β form. I have plotted the normalized absorbance spectra of the α and β forms in Figure 6.4d. The lowest energy vibronic shoulder for the S_1 absorption is $\sim$600 cm^{-1} red shifted in the β polymorph compared to the α polymorph as marked in Figure 6.4d. Thus, the β form is more stable and has a lower energy state than the α polymorph, which allows for rapid excimer formation followed by their trapping. Due to this

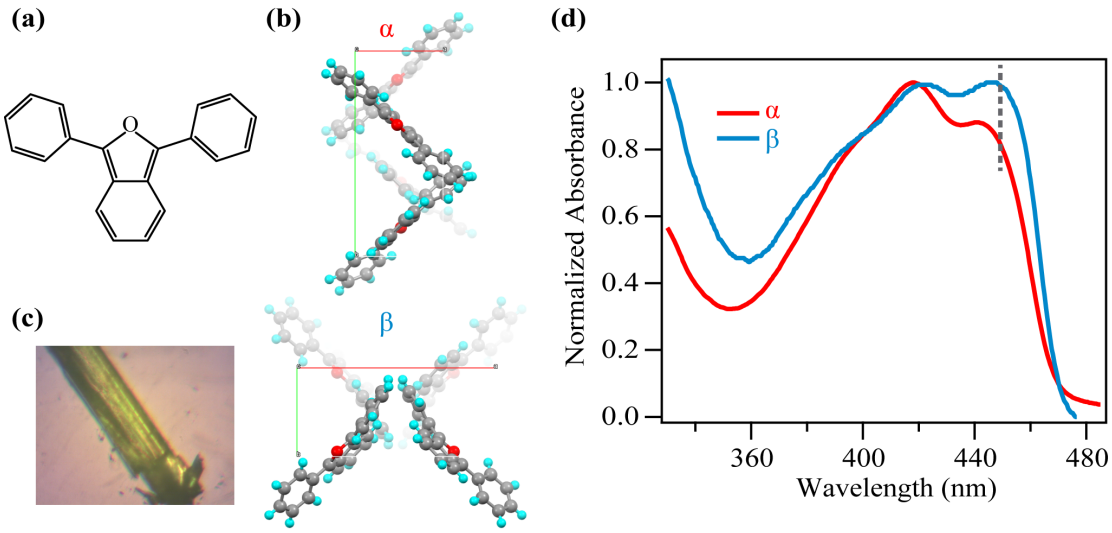

Figure 6.4: (a) Molecular structure of 1,3-diphenylisobenzofuran (DPIB). (b) Unit cells of α and β crystalline forms of DPIB looking down the c axis. (c) Optical image under microscope of β-form. (d) Absorption spectra for films of α and β polymorphs of DPIB. The gray dashed line denotes the lowest energy transition in β.

competing process, the singlet fission process is inhibited in the β polymorph, whereas the α form undergoes singlet fission with $\sim$200% triplet yield.

The presence of the different photophysics resulting from polymorphs with similar crystal structures and molecular packing calls for an interrogation into the role of lattice vibrations in executing these diverse photophysical phenomena. To probe whether the phonons modes are responsible for the different photophysics, it is necessary to examine the excited state structural evolution of the two polymorphs. The hypothesis here is that any observation of quantum beats in the FSRS data that can be assigned to the coupling of the high frequency vibrations with low-frequency phonon modes, can then be used to control the different photophysics observed in the two polymorphs.

To test for the presence of quantum beats, I conducted FSRS experiments on crystalline β-DPIB and present the excited-state data after its one-to-one subtraction from the ground state stimulated Raman in Figure 6.5a. I observe huge depletions for all the ground state Raman peaks due to fewer molecules in the ground state after photoexcitation. The trace at the bottom of the FSR data sets in Figure 6.5a correspond to the ground state stimulated Raman spectrum of crystalline β-DPIB scaled by a factor of 0.1 for clear pictorial representation.

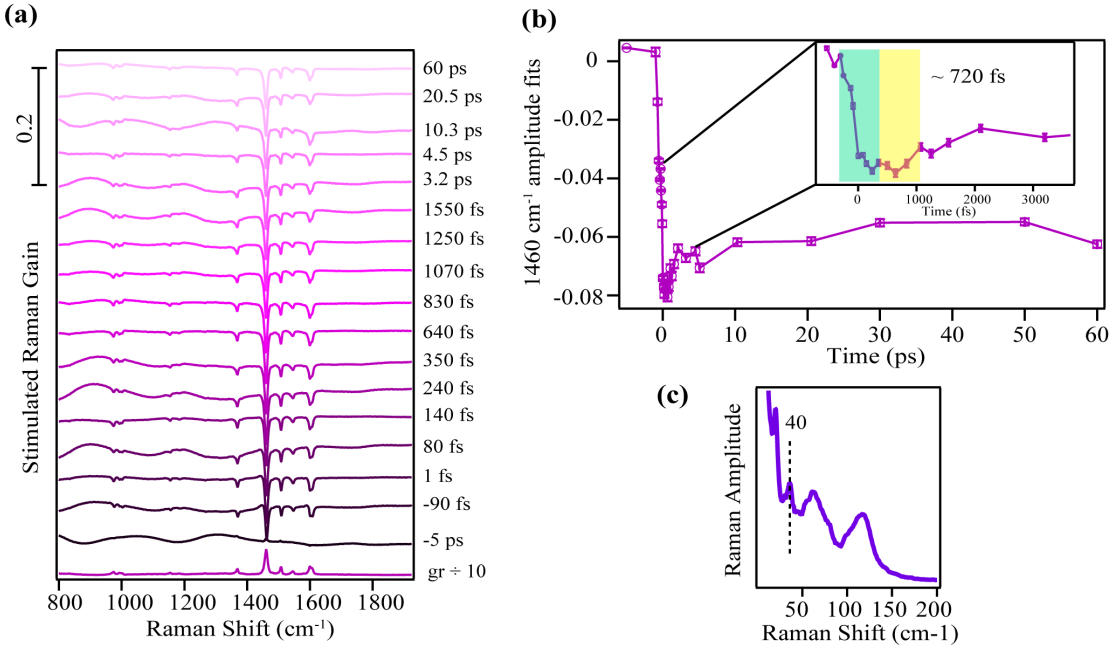

Figure 6.5: (a) Time-resolved FSR spectra after one-to-one subtraction in the β polymorph of DPIB. (b) Kinetics of the ground state bleach at 1460 cm^{-1} at different time intervals after photoexcitation. Inset shows a zoom-in of the first 2 ps. The green and yellow boxes depict the period of the oscillations, $\sim$720 fs. (c) Phonon modes in β-polymorph of DPIB. The phonon mode at $\sim$40 cm^{-1} corresponds to the frequency of oscillation in the 1460 cm^{-1} amplitude in (b).

To understand the excited state dynamics, I fit the ground state bleach at 1460 cm^{-1} with a Gaussian function and plot the amplitude of the bleach in

Figure 6.5b. The ground state bleach reached its maxima at ∼20% of ground state amplitude and the depletion was not recovered by 200 ps. I do not observe any transient spectral evolution that could provide us with any structural evolutionary insights. This implies that the photoexcited species are very long lived and are likely forming trapped excimers as suggested by previous studies.

Focusing on the early time dynamics within the first 2 ps in Figure 6.5b, I observe that the peak amplitudes are modulating with a time interval of ∼720 fs. This time period corresponds to a frequency of 46 cm^{-1} in the frequency domain. To ascertain the origin and resemblance of this peak frequency at 46 cm^{-1}, I collected low-frequency Raman spectrum of β-DPIB and present it in Figure 6.5c. The β-polymorph has a phonon mode around 40 cm^{-1} which matched extremely well with our FSRS data. This excellent match in the Raman frequency implies that phonon-modes are coupled to intramolecular vibrations. Having this knowledge of the β-form, we can use this information to control the reaction coordinate after photoexcitation. Conducting similar studies on the α-polymorph can help us identify the vibrational modes that might drive the efficient singlet fission process.

Acquiring this knowledge about the nuclear coordinates associated with the excimer and triplet generation process will allow us to selectively excite the vibrational modes that facilitate the efficient charge transport phenomenon. This control to "turn on" and "turn off" certain nuclear motions provide a handle to modulate the chemical reaction pathway in accordance with the desired outcome. Having a deeper understanding of the factors affecting the charge transport and a way to tune the transport properties through a molecular crystal will guide us

to improve electronic device performance.

6.5 Excited State Dynamics as a Function of Molecular and Crystal Structure

I have previously studied the effect of chemical substitution on singlet fission through a series of rubrene derivatives discussed in Chapter 4. The derivatives studied in Chapter 4 were chosen such that they displayed the same crystal packing structure as crystalline rubrene. From the derivatives studied in Chapter 4, we now know that the presence of electron withdrawing groups helps to make the singlet fission process an order of magnitude faster than that observed in rubrene. An interesting future direction will be to study the excited state dynamics of rubrene derivatives as a function of chemical substitution with simultaneous differences in their crystal packing compared to rubrene to obtain insights into the effect of selectively substituted molecules on the nature of the photophysical processes.

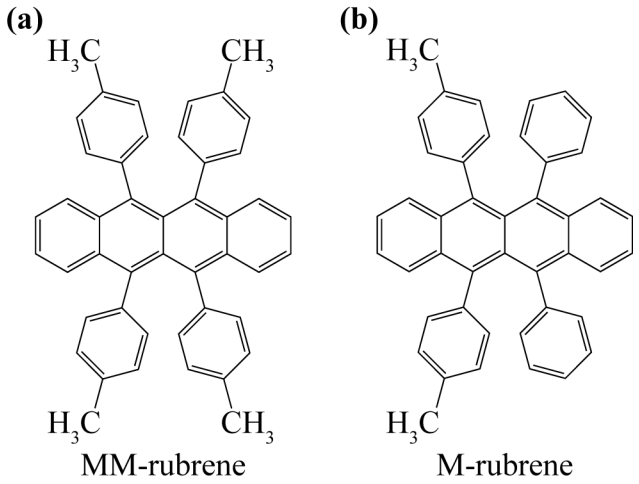

Figure 6.6: Molecular structure of (a) MM-rubrene and (b) M-rubrene.

To understand the role of the planarity of the tetracene core in deciding the fate of the excited state wavepacket, I have run some preliminary FSRS experiments on two rubrene derivatives: MM-rubrene and M-rubrene, where the para position of the periphery phenyl groups are substituted with -CH_3 groups, as shown in Figure 6.6. The tetracene backbone is twisted in both the M- and MM-rubrene derivatives in their solid crystalline form. [96] The MM-rubrene packs in a monoclinic (C2/c) structure and M-rubrene in orthorhombic (Pna2(1)) structure. The π-stacking is absent in both the derivative systems because the methyl groups at the para position in the phenyl groups favors the interactions with the tetracene core over the interlayer interactions between the other aryl groups. Therefore, these two derivatives are model systems to understand the effect of a twisted backbone and a different crystal structure on the dynamics after photoabsorption.

I used the same FSRS setup and experimental parameters mentioned in Chapter 4 for the FSRS studies on MM-rubrene and M-rubrene crystals. I present the one-to-one subtracted FSR data of MM-rubrene in Figure 6.6a and M-rubrene in Figure 6.6c. I observe large bleach features of the ground state modes in the excited state spectra due to the fact that there are fewer molecules in the ground state after photoexcitation. The traces at the bottom of the FSR data sets in Figure 6.7a and 6.7b correspond to the ground state stimulated Raman spectrum of crystalline MM-rubrene and M-rubrene, each scaled by a factor of 0.1 for clear pictorial representation.

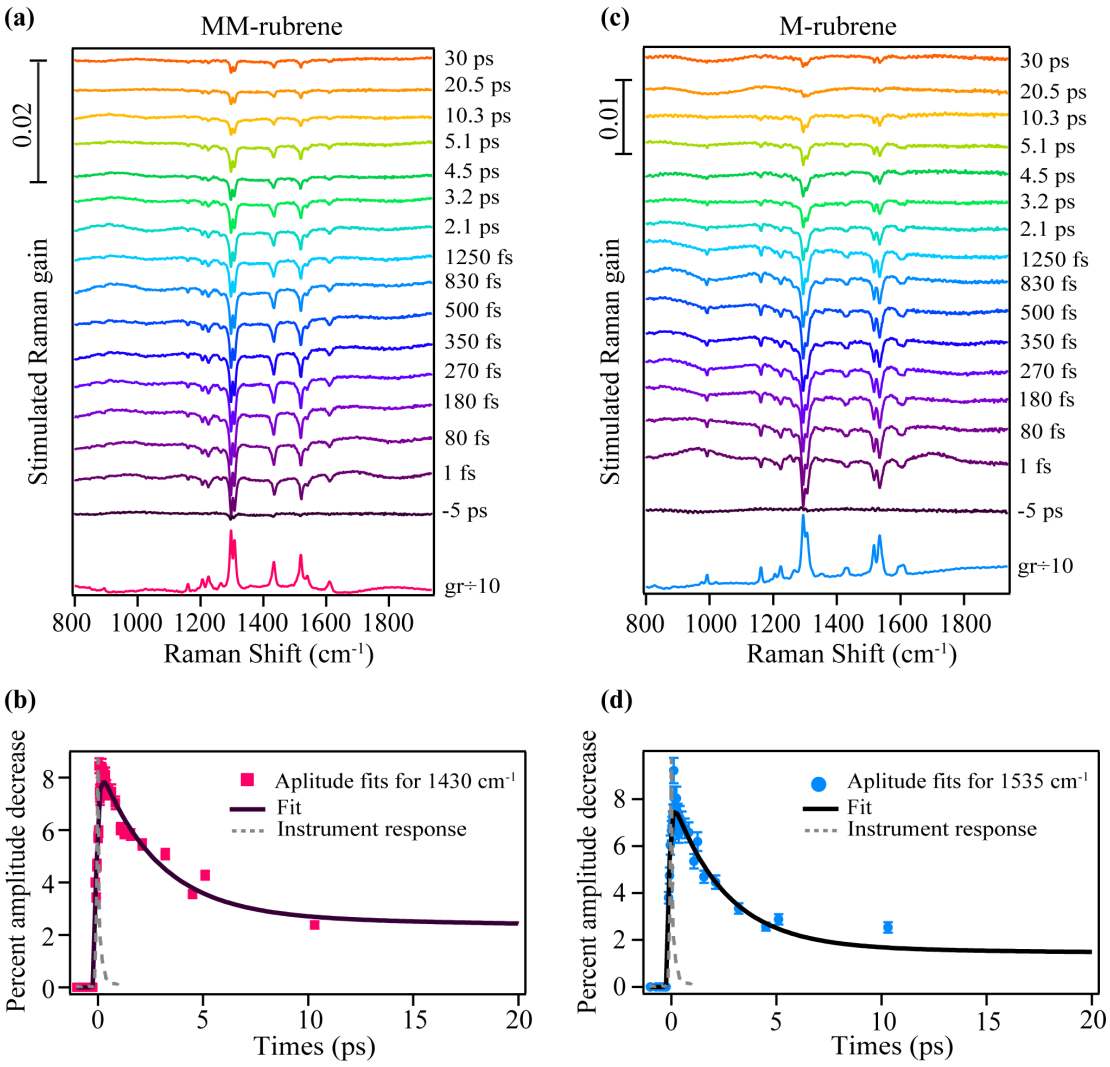

Figure 6.7: Time-resolved FSR data of (a) crystalline MM-rubrene and (c) M-rubrene. Kinetics of percent amplitude decrease of the 1430 cm^{-1} ground state mode in (b) MM-rubrene and 1535 cm^{-1} ground state mode in (d) M-rubrene. The gray dashed spectrum in (b) and (d) is the instrument response function.

To extract information on the transient evolution, I fit the ground state bleach of the Raman modes around 1430 cm^{-1} and 1535 cm^{-1} at different time delays after photoexcitation with a Gaussian spectral function and plot the dynamics of this fitted peak frequency as a function of time for MM-rubrene and M-rubrene in Figure 6.7b and 6.7d, respectively. The experimental error bars for the frequency fits are contained within the markers. I fit the spectral peak frequencies to an exponential rise and decay convolved with the cross-correlation between the actinic pulse and the Raman probe to obtain the kinetics. Table 6.1 summarizes the time constants associated with the kinetic fits.

Table 6.1: Time constants obtained from the exponential fits of the ground state bleach kinetics in MM-rubrene and M-rubrene. All fits are exponentials convolved with the 120 fs instrument cross-correlation.

	Rise time (fs)	Decay time (ps)
MM-rubrene	108 ± 33	2.8 ± 0.6
M-rubrene	110 ± 59	2.5 ± 0.5

The ground state depletion features rise effectively within the cross-correlation time (120 fs) for both MM-rubrene and M-rubrene, and decay in approximately 3 picoseconds with the MM-rubrene ground state depletion feature possibly persisting for slightly longer than the M-rubrene bleach. Here, the MM-rubrene ground state bleach peaked at only ∼8% of the ground state amplitude within the first 108 fs and maintained 3% ground state depletion at 20 ps. The M-rubrene ground state bleach peaked at ∼9% ground state amplitude within 110 fs and 2% persisted out to 20 ps. An additional time constant of tens of nanoseconds, corresponding to the exciton lifetime, was held constant to fit the amplitude dynamics of the 1430 and 1535 cm^{-1} features. This nanoseconds long-time component of the decay

could be used to interpret the effective yield in the excited state photophysical process.

Comparing the FSRS spectra of MM-rubrene and M-rubrene with that of rubrene, FM-rubrene and F-rubrene from Chapter 4, I notice that the broad background observed in the rubrene, FM-rubrene and F-rubrene FSR data due to transient absorption from the excited electronic states is absent in MM-rubrene and M-rubrene. The kinetics and lifetimes of the broad transient absorption features in the planar tetracene core rubrene derivatives were indicative of triplet states generated from singlet fission. However, the absence of the broad features in the FSRS data in Figure 6.7a and c implies that MM-rubrene and M-rubrene probably does not undergo singlet fission. There is a possibility of excimer formation and their trapping, which can in turn suppress the energy decay though the singlet fission process in the two derivatives. Apart from this, I do not observe any transient spectral shift in the two derivatives. This lack of excited state structural dynamics could be either due to the mismatch between the relative orientation of the transition dipole moment and the polarization of the Raman pump and probe, or due to mismatch of the resonance conditions of the excitons in the excited states.

The dynamics of photophysical processes are strongly anisotropic in crystalline rubrene. Thus, it is reasonable to assume that MM-rubrene and M-rubrene are also anisotropic, and hence future ultrafast studies must be conducted with different crystal orientations that might provide interesting spectral and structural evolution in those derivatives. The preliminary results indicate the absence of singlet fission in MM-rubrene and M-rubrene. Even though this is not completely

surprising given that the tetracene backbone is twisted, it is a good proof-of-concept to identify the need of the solid π-stacking for efficient singlet fission process for its further application in optoelectronics.

6.6 Conclusions

In summary, I have explored the excited state structural evolution in organic semiconductors of rubrene and its derivatives during singlet fission using FSRS. I have provided a predictive model for the rational design of new class of molecules for efficient singlet fission for device performance. Additionally, I made an advancement in the FSRS experimental setup so as to extract the interesting Raman features from the other non-linear processes to simplify the data interpretation. Finally, I have proposed multiple future directions that can be explored in terms of different chemical materials and different kinds of photophysical processes using FSRS.

In conclusion, the focus of this thesis is to understand singlet fission through the lens of FSRS, a very promising ultrafast structurally sensitive technique in the field of fundamental research due to its outstanding technical properties. I have shown that FSRS is an extremely powerful technique to study ultrafast processes and I believe that the successes presented in this thesis will advance the ultrafast community to use FSRS extensively for studying ultrafast reaction dynamics in the years to come.

Bibliography

[1] W. Shockley and H. J. Queisser. Detailed balance limit of efficiency of p-n junction solar cells. *Journal of Applied Physics*, 32(3):510–519, 1961.

[2] M. Smith and J. Michl. Singlet fission. *Chemical Reviews*, 110:6891–6936, 2010.

[3] M. Smith and J. Michl. Recent advances in singlet fission. *Annual Review of Physical Chemistry*, 64:361–86, 2013.

[4] M. Einzinger, T. Wu, J. F. Kompalla, H. L. Smith, C. F. Perkinson, L. Nienhaus, S. Wieghold, D. N. Congreve, A. Kahn, M. G. Bawendi, and M. A. Baldo. Sensitization of silicon by singlet exciton fission in tetracene. *Nature*, 571(7763):90–94, 7 2019.

[5] D. W. McCamant, P. Kukura, and R. A. Mathies. Femtosecond time-resolved stimulated Raman spectroscopy: Application to the ultrafast internal conversion in β-carotene. *Journal of Physical Chemistry A*, 107(40):8208–8214, 2003.

[6] D. N. Congreve, J. Lee, N. J. Thompson, E. Hontz, S. R. Yost, P. D. Reusswig, M. E. Bahlke, S. Reineke, T. Van Voorhis, and M. A. Baldo. External quantum efficiency above 100% in a singlet-exciton-fission-based organic photovoltaic cell. *Science*, 340:334–337, 2013.

[7] R. G. Kepler, J. C. Caris, P. Avakian, and E. Abramson. Triplet excitons and delayed fluorescence in anthracene crystals. *Physical Review Letters*, 10(9):400–402, 5 1963.

[8] S. Singh, W. J. Jones, W. Siebrand, B. P. Stoicheff, and W. G. Schneider. Laser generation of excitons and fluorescence in anthracene crystals. *The Journal of Chemical Physics*, 42:330–342, 1965.

[9] M. C. Hanna and A. J. Nozik. Solar conversion efficiency of photovoltaic and photoelectrolysis cells with carrier multiplication absorbers. *Journal of Applied Physics*, 100(7):074510, 2006.

[10] M. K. Gish, N. A. Pace, G. Rumbles, and J. C. Johnson. Emerging design principles for enhanced solar energy utilization with singlet fission. *Journal of Physical Chemistry C*, 123(7):3923–3934, 2 2019.

[11] S. Ito, T. Nagami, and M. Nakano. Molecular design for efficient singlet fission. *Journal of Photochemistry and Photobiology C*, 34:85–120, 3 2018.

[12] A. Rao and R. H. Friend. Harnessing singlet exciton fission to break the Shockley-Queisser limit. *Nature Reviews Materials*, 2(11):17063, 10 2017.

[13] K. Miyata, F. S. Conrad-Burton, F. L. Geyer, and X.-Y. Zhu. Triplet pair states in singlet fission. *Chem. Rev.*, 119(6):4261–4292, 2 2019.

[14] A. J. Musser and J. Clark. Triplet-pair states in organic semiconductors. *Annual Review of Physical Chemistry*, 70:323–351, 2019.

[15] J. Xia, S. N. Sanders, W. Cheng, J. Z. Low, J. Liu, L. M. Campos, and T. Sun. Singlet fission: Progress and prospects in solar cells. *Advanced Materials*, 29(20):1601652, 5 2017.

[16] N. Monahan and X.-Y. Zhu. Charge transfer–mediated singlet fission. *Annual Review of Physical Chemistry*, 66(1):601–618, 2015.

[17] A. J. Musser, M. Liebel, C. Schnedermann, T. Wende, T. B. Kehoe, A. Rao, and P. Kukura. Evidence for conical intersection dynamics mediating ultrafast singlet exciton fission. *Nature Physics*, 11(4):352–357, 4 2015.

[18] E. G. Fuemmeler, S. N. Sanders, A. B. Pun, E. Kumarasamy, T. Zeng, K. Miyata, M. L. Steigerwald, X.-Y. Zhu, M. Y. Sfeir, L. M. Campos, and N. Ananth. A direct mechanism of ultrafast intramolecular singlet fission in pentacene dimers. *ACS Central Science*, 2(5):316–324, 2016.

[19] D. Beljonne, H. Yamagata, J. L. Brédas, F. C. Spano, and Y. Olivier. Charge-transfer excitations steer the davydov splitting and mediate singlet exciton fission in pentacene. *Physical Review Letters*, 110(22):226402, 2013.

[20] D. Guo, L. Ma, Z. Zhou, D. Lin, C. Wang, X. Zhao, F. Zhang, J. Zhang, and Z. Nie. Charge transfer dynamics in a singlet fission organic molecule and

organometal perovskite bilayer structure. *Journal of Materials Chemistry A*, 8(11):5572–5579, 3 2020.

[21] J. Guo, H. Ohkita, H. Benten, and S. Ito. Near-IR femtosecond transient absorption spectroscopy of ultrafast polaron and triplet exciton formation in polythiophene films with different regioregularities. *Journal of the American Chemical Society*, 131(46):16869–16880, 2009.

[22] P. M. Zimmerman, Z. Zhang, and C. B. Musgrave. Singlet fission in pentacene through multi-exciton quantum states. *Nature Chemistry*, 2(8):648–652, 8 2010.

[23] M. Tuan Trinh, A. Pinkard, A. B. Pun, S. N. Sanders, E. Kumarasamy, M. Y. Sfeir, L. M. Campos, X. Roy, and X. Y. Zhu. Distinct properties of the triplet pair state from singlet fission. *Science Advances*, 3(7):e1700241, 7 2017.

[24] I. Breen, R. Tempelaar, L. A. Bizimana, B. Kloss, D. R. Reichman, and D. B. Turner. Triplet separation drives singlet fission after femtosecond correlated triplet pair production in rubrene. *Journal of the American Chemical Society*, 139(34):11745–11751, 8 2017.

[25] N. R. Monahan, D. Sun, H. Tamura, K. W. Williams, B. Xu, Y. Zhong, B. Kumar, C. Nuckolls, A. R. Harutyunyan, G. Chen, H.-L. Dai, D. Beljonne, Y. Rao, and X.-Y. Zhu. Dynamics of the triplet-pair state reveals the likely coexistence of coherent and incoherent singlet fission in crystalline hexacene. *Nature Chemistry*, 9(4):341–346, 4 2017.

[26] W.-L. Chan, M. Ligges, A. Jailaubekov, L. Kaake, L. Miaja-Avila, and X.-Y. Zhu. Observing the multiexciton state in singlet fission and ensuing ultrafast multielectron transfer. *Science*, 334(6062):1541–1545, 12 2011.

[27] B. S. Basel, J. Zirzlmeier, C. Hetzer, B. T. Phelan, M. D. Krzyaniak, S. R. Reddy, P. B. Coto, N. E. Horwitz, R. M. Young, F. J. White, F. Hampel, T. Clark, M. Thoss, R. R. Tykwinski, M. R. Wasielewski, and D. M. Guldi. Unified model for singlet fission within a non-conjugated covalent pentacene dimer. *Nature Communications*, 8:15171, 5 2017.

[28] S. Matsuda, S. Oyama, and Y. Kobori. Electron spin polarization generated by transport of singlet and quintet multiexcitons to spin-correlated triplet pairs during singlet fissions. *Chemical Science*, 11(11):2934–2942, 3 2020.

[29] D. Casanova. Theoretical modeling of singlet fission. *Chemical Reviews*, 118(15):7164–7207, 8 2018.

[30] A. Japahuge and T. Zeng. Theoretical studies of singlet fission: Searching for materials and exploring mechanisms. *ChemPlusChem*, 83(4):146–182, 4 2018.

[31] A. F. Morrison and J. M. Herbert. Evidence for singlet fission driven by vibronic coherence in crystalline tetracene. *Journal of Physical Chemistry Letters*, 8(7):1442–1448, 2017.

[32] K. Shizu, C. Adachi, and H. Kaji. Effect of vibronic coupling on correlated triplet pair formation in the singlet fission process of linked tetracene dimers. *Journal of Physical Chemistry A*, 124(18):3641–3651, 2020.

[33] G. H. Deng, Q. Wei, J. Han, Y. Qian, J. Luo, A. R. Harutyunyan, G. Chen, H. Bian, H. Chen, and Y. Rao. Vibronic fingerprint of singlet fission in hexacene. *Journal of Chemical Physics*, 151(5):054703, 8 2019.

[34] M. Chen, Y. J. Bae, C. M. Mauck, A. Mandal, R. M. Young, and M. R. Wasielewski. Singlet fission in covalent terrylenediimide dimers: Probing the nature of the multiexciton state using femtosecond mid-infrared spectroscopy. *Journal of the American Chemical Society*, 140(29):9184–9192, 7 2018.

[35] E. A. Margulies, N. Kerisit, P. Gawel, C. M. Mauck, L. Ma, C. E. Miller, R. M. Young, N. Trapp, Y.-L. Wu, F. Diederich, and M. R. Wasielewski. Substituent effects on singlet exciton fission in polycrystalline thin films of cyano-substituted diaryltetracenes. *Journal of Physical Chemistry C*, 121(39):21262–21271, 2017.

[36] C. Grieco, E. R. Kennehan, A. Rimshaw, M. M. Payne, J. E. Anthony, and J. B. Asbury. Harnessing molecular vibrations to probe triplet dynamics during singlet fission. *Journal of Physical Chemistry Letters*, 8(23):5700–5706, 12 2017.

[37] C. Grieco, E. R. Kennehan, H. Kim, R. D. Pensack, A. N. Brigeman, A. Rimshaw, M. M. Payne, J. E. Anthony, N. C. Giebink, G. D. Scholes, and J. B. Asbury. Direct observation of correlated triplet pair dynamics during singlet fission using ultrafast mid-ir spectroscopy. *Journal of Physical Chemistry C*, 122(4):2012–2022, 2 2018.

[38] C. Grieco, G. S. Doucette, K. T. Munson, J. R. Swartzfager, J. M. Munro, J. E. Anthony, I. Dabo, and J. B. Asbury. Vibrational probe of the origin of singlet exciton fission in TIPS-pentacene solutions. *Journal of Chemical Physics*, 151(15):154701, 10 2019.

[39] M. Angelella, C. Wang, and M. J. Tauber. Resonance Raman spectra of a perylene bis(dicarboximide) chromophore in ground and lowest triplet states. *Journal of Physical Chemistry A*, 117(38):9196–9204, 2013.

[40] C. Wang, M. Angelella, S. J. Doyle, L. A. Lytwak, P. J. Rossky, B. J. Holliday, and M. J. Tauber. Resonance Raman spectroscopy of the T_1 triplet excited state of oligothiophenes. *Journal of Physical Chemistry Letters*, 6(18):3521–3527, 2015.

[41] M. J. Llansola-Portoles, K. Redeckas, S. Streckaité, C. Ilioaia, A. A. Pascal, A. Telfer, M. Vengris, L. Valkunas, and B. Robert. Lycopene crystalloids exhibit singlet exciton fission in tomatoes. *Physical Chemistry Chemical Physics*, 20(13):8640–8646, 3 2018.

[42] C. Wang and M. J. Tauber. High-yield singlet fission in a zeaxanthin aggregate observed by picosecond resonance Raman spectroscopy. *Journal of the American Chemical Society*, 132(40):13988–13991, 10 2010.

[43] C. Wang, D. E. Schlamadinger, V. Desai, and M. J. Tauber. Triplet excitons of carotenoids formed by singlet fission in a membrane. *ChemPhysChem*, 12(16):2891–2894, 11 2011.

[44] S. Jana, A. L. Yapamanu, and S. Umapathy. Unraveling structural dynamics in isoenergetic excited S_1 and multi-excitonic ^{1}(TT) states of 9,10-bis(phenylethynyl)anthracene (BPEA) in solution: Via ultrafast Raman loss spectroscopy. *Physical Chemistry Chemical Physics*, 21(26):14341–14349, 7 2019.

[45] H. L. Stern, A. Cheminal, S. R. Yost, K. Broch, S. L. Bayliss, K. Chen, M. Tabachnyk, K. Thorley, N. Greenham, J. M. Hodgkiss, J. Anthony, M. Head-Gordon, A. J. Musser, A. Rao, and R. H. Friend. Vibronically coherent ultrafast triplet-pair formation and subsequent thermally activated dissociation control efficient endothermic singlet fission. *Nature Chemistry*, 9(12):1205–1212, 12 2017.

[46] C. Schnedermann, A. M. Alvertis, T. Wende, S. Lukman, J. Feng, F. A. Schröder, D. H. Turban, J. Wu, N. D. Hine, N. C. Greenham, A. W. Chin,

A. Rao, P. Kukura, and A. J. Musser. A molecular movie of ultrafast singlet fission. *Nature Communications*, 10:4207, 12 2019.

[47] S. M. Hart, W. R. Silva, and R. R. Frontiera. Femtosecond stimulated Raman evidence for charge-transfer character in pentacene singlet fission. *Chemical Science*, 9:1242–1250, 2018.

[48] K. Bera, C. J. Douglas, and R. R. Frontiera. Femtosecond Raman microscopy reveals structural dynamics leading to triplet separation in rubrene singlet fission. *The Journal of Physical Chemistry Letters*, 8(23):5929–5934, 12 2017.

[49] K. Bera, C. J. Douglas, and R. R. Frontiera. Femtosecond stimulated Raman spectroscopy – guided screening leads to efficient singlet fission in rubrene derivatives. *Submitted to Chemical Science*, 2020.

[50] M. J. Y. Tayebjee, S. N. Sanders, E. Kumarasamy, L. M. Campos, M. Y. Sfeir, and D. R. McCamey. Quintet multiexciton dynamics in singlet fission. *Nature Physics*, 13(2):182–188, 2 2016.

[51] J. L. Musfeldt, L. I. Vergara, V. T. Brinzari, C. Lee, L. C. Tung, J. Kang, Y. J. Wang, J. A. Schlueter, J. L. Manson, and M. H. Whangbo. Magnetoelastic coupling through the antiferromagnet-to-ferromagnet transition of quasi-two-dimensional $[Cu(HF_2)(pyz)_2]BF_4$ using infrared spectroscopy. *Physical Review Letters*, 103(15):157401, 10 2009.

[52] E. M. Grumstrup, J. C. Johnson, and N. H. Damrauer. Enhanced triplet formation in polycrystalline tetracene films by femtosecond optical-pulse shaping. *Physical Review Letters*, 105:257403, 2010.

[53] M. A. Castellanos and P. Huo. Enhancing singlet fission dynamics by suppressing destructive interference between charge-transfer pathways. *Journal of Physical Chemistry Letters*, 8(11):2480–2488, 2017.

[54] B. C. Paulus, S. L. Adelman, L. L. Jamula, and J. K. McCusker. Leveraging excited-state coherence for synthetic control of ultrafast dynamics. *Nature*, 582(7811):214–218, 6 2020.

[55] A. I. McIntosh, B. Yang, S. M. Goldup, M. Watkinson, and R. S. Donnan. Terahertz spectroscopy: A powerful new tool for the chemical sciences? *Chemical Society Reviews*, 41:2072–2082, 2012.

[56] O. Esenturk, P. A. Lane, J. S. Melinger, and E. J. Heilweil. Ultrafast terahertz spectroscopy for measuring carrier dynamics in nanoscale photovoltaic materials. *Proc. SPIE*, 7600:76000I, 2010.

[57] Y. Lan, X. Tao, X. Kong, Y. He, X. Zheng, M. Sutton, M. G. Kanatzidis, H. Guo, and D. G. Cooke. Coherent charge-phonon correlations and exciton dynamics in orthorhombic $CH_3NH_3PbI_3$ measured by ultrafast multi-thz spectroscopy. *Journal of Chemical Physics*, 151(21):214201, 2019.

[58] G. M. Akselrod, P. B. Deotare, N. J. Thompson, J. Lee, W. A. Tisdale, M. A. Baldo, V. M. Menon, and V. Bulovic. Visualization of exciton transport in ordered and disordered molecular solids. *Nature Communications*, 5:3646, 4 2014.

[59] T. Zhu and L. Huang. Exciton transport in singlet fission materials: A new hare and tortoise story. *Journal of Physical Chemistry Letters*, 9(22):6502–6510, 11 2018.

[60] S. Y. Kwang and R. R. Frontiera. Spatially offset femtosecond stimulated Raman spectroscopy: Observing exciton transport through a vibrational lens. *The Journal of Physical Chemistry Letters*, 11(11):4337–4344, 5 2020.

[61] J. Lee, P. Jadhav, and M. A. Baldo. High efficiency organic multilayer photodetectors based on singlet exciton fission. *Applied Physics Letters*, 95(3):033301, 2009.

[62] G. D. Scholes. Correlated pair states formed by singlet fission and exciton-exciton annihilation. *Journal of Physical Chemistry A*, 119(51):12699–12705, 2015.

[63] S. R. Yost, J. Lee, M. W. B. Wilson, T. Wu, D. P. McMahon, R. R. Parkhurst, N. J. Thompson, D. N. Congreve, A. Rao, K. Johnson, M. Y. Sfeir, M. G. Bawendi, T. M. Swager, R. H. Friend, M. A. Baldo, and T. Van Voorhis. A transferable model for singlet-fission kinetics. *Nature Chemistry*, 6(6):492–497, 2014.

[64] P. M. Zimmerman, F. Bell, D. Casanova, and M. Head-Gordon. Mechanism for singlet fission in pentacene and tetracene: From single exciton to two triplets. *Journal of the American Chemical Society*, 133(49):19944–19952, 2011.

[65] E. A. Margulies, J. L. Logsdon, C. E. Miller, L. Ma, E. Simonoff, R. M. Young, G. C. Schatz, and M. R. Wasielewski. Direct observation of a charge-transfer state preceding high-yield singlet fission in terrylenediimide thin films. *Journal of the American Chemical Society*, 139(2):663–671, 2017.

[66] R. D. Pensack, E. E. Ostroumov, A. J. Tilley, S. Mazza, C. Grieco, K. J. Thorley, J. B. Asbury, D. S. Seferos, J. E. Anthony, and G. D. Scholes. Observation of two triplet-pair intermediates in singlet exciton fission. *Journal of Physical Chemistry Letters*, 7(13):2370–2375, 2016.

[67] K. Miyata, Y. Kurashige, K. Watanabe, T. Sugimoto, S. Takahashi, S. Tanaka, J. Takeya, T. Yanai, and Y. Matsumoto. Coherent singlet fission activated by symmetry breaking. *Nature Chemistry*, 9:983–989, 2017.

[68] M. Wakasa, M. Kaise, T. Yago, R. Katoh, Y. Wakikawa, and T. Ikoma. What can be learned from magnetic field effects on singlet fission: Role of exchange interaction in excited triplet pairs. *Journal of Physical Chemistry C*, 119(46):25840–25844, 2015.

[69] A. Köhler and H. Bässler. Triplet states in organic semiconductors. *Materials Science and Engineering R: Reports*, 66(4-6):71–109, 2009.

[70] A. Ryasnyanskiy and I. Biaggio. Triplet exciton dynamics in rubrene single crystals. *Physical Review B*, 84(19):2–5, 2011.

[71] L. Ma, K. Zhang, C. Kloc, H. Sun, M. E. Michel-Beyerle, and G. G. Gurzadyan. Singlet fission in rubrene single crystal: direct observation by femtosecond pump–probe spectroscopy. *Physical Chemistry Chemical Physics*, 14(23):8307–8312, 2012.

[72] L. Ma, K. Zhang, C. Kloc, H. Sun, C. Soci, M. E. Michel-Beyerle, and G. G. Gurzadyan. Fluorescence from rubrene single crystals: Interplay of singlet fission and energy trapping. *Physical Review B*, 87:201203, 2013.

[73] H. Tsunoyama and A. Nakajima. Anion photoelectron spectroscopy of rubrene: Molecular insights into singlet fission energetics. *The Journal of Physical Chemistry C*, 121(38):20680–20686, 2017.

[74] Y. Chen, B. Lee, D. Fu, and V. Podzorov. The origin of a 650 nm photoluminescence band in rubrene. *Advanced Materials*, 23(45):5370–5375, 2011.

[75] H. Najafov, B. Lee, Q. Zhou, L. C. Feldman, and V. Podzorov. Observation of long-range exciton diffusion in highly ordered organic semiconductors. *Nature materials*, 9(11):938–943, 2010.

[76] L. Ma, G. Galstyan, K. Zhang, C. Kloc, H. Sun, C. Soci, M. E. Michel-Beyerle, and G. G. Gurzadyan. Two-photon-induced singlet fission in rubrene single crystal. *Journal of Chemical Physics*, 138(18):184508, 2013.

[77] P. Irkhin and I. Biaggio. Direct imaging of anisotropic exciton diffusion and triplet diffusion length in rubrene single crystals. *Physical Review Letters*, 107(1):017402, 2011.

[78] I. Biaggio and P. Irkhin. Extremely efficient exciton fission and fusion and its dominant contribution to the photoluminescence yield in rubrene single crystals. *Applied Physics Letters*, 103(26):263301, 2013.

[79] W. R. Silva and R. R. Frontiera. Excited state structural evolution during charge-transfer reactions in betaine-30. *Physical Chemistry Chemical Physics*, 18:20290–20297, 2016.

[80] P. Kukura, D. W. McCamant, and R. A. Mathies. Femtosecond stimulated Raman spectroscopy. *Annual Review of Physical Chemistry*, 58(1):461–488, 5 2007.

[81] P. Kukura, S. Yoon, and R. A. Mathies. Femtosecond stimulated Raman spectroscopy. *Analytical Chemistry*, 78(17):5952–5959, 2006.

[82] D. W. McCamant, P. Kukura, S. Yoon, and R. A. Mathies. Femtosecond broadband stimulated Raman spectroscopy: Apparatus and methods. *Review of Scientific Instruments*, 75(11):4971–4980, 2004.

[83] D. R. Dietze and R. A. Mathies. Femtosecond stimulated Raman spectroscopy. *ChemPhysChem*, 17(9):1224–1251, 2016.

[84] A. E. Bragg, W. Yu, J. Zhou, and T. Magnanelli. Ultrafast Raman spectroscopy as a probe of local structure and dynamics in photoexcited conjugated materials. *Journal of Physical Chemistry Letters*, 7(19):3990–4000, 2016.

[85] F. Provencher, N. Bérubé, A. W. Parker, G. M. Greetham, M. Towrie, C. Hellmann, M. Côté, N. Stingelin, C. Silva, and S. C. Hayes. Direct observation of ultrafast long-range charge separation at polymer–fullerene heterojunctions. *Nature Communications*, 5:4288, 2014.

[86] R. A. Laudise, C. Kloc, P. G. Simpkins, and T. Siegrist. Physical vapor growth of organic semiconductors. *Journal of Crystal Growth*, 187:449–454, 1998.

[87] M. A. Reyes-Martinez, A. Ramasubramaniam, A. L. Briseno, and A. J. Crosby. The intrinsic mechanical properties of rubrene single crystals. *Advanced Materials*, 24(41):5548–5552, 2012.

[88] W. A. Ogden, S. Ghosh, M. J. Bruzek, K. A. McGarry, L. Balhorn, V. Young, L. J. Purvis, S. E. Wegwerth, Z. Zhang, N. A. Serratore, C. J. Cramer, L. Gagliardi, and C. J. Douglas. Partial fluorination as a strategy for crystal engineering of rubrene derivatives. *Crystal Growth and Design*, 17(2):643–658, 2017.

[89] P. Kukura, D. W. McCamant, S. Yoon, D. B. Wandschneider, and R. A. Mathies. Structural observation of the primary isomerization in vision with femtosecond-stimulated Raman. *Science*, 310(5750):1006–1009, 2005.

[90] J. Dasgupta, R. R. Frontiera, K. C. Taylor, J. C. Lagarias, and R. A. Mathies. Ultrafast excited-state isomerization in phytochrome revealed by femtosecond stimulated Raman spectroscopy. *Proceedings of the National Academy of Sciences*, 106(6):1784–1789, 2009.

[91] D. W. McCamant, P. Kukura, and R. A. Mathies. Femtosecond stimulated Raman study of excited-state evolution in bacteriorhodopsin. *Journal of Physical Chemistry B*, 109(20):10449–10457, 2005.

[92] C. Fang, R. R. Frontiera, R. Tran, and R. A. Mathies. Mapping GFP structure evolution during proton transfer with femtosecond Raman spectroscopy. *Nature*, 462(7270):200–204, 2009.

[93] R. R. Frontiera, J. Dasgupta, and R. A. Mathies. Probing interfacial electron transfer in coumarin 343 sensitized TiO_2 nanoparticles with femtosecond stimulated Raman. *Journal of the American Chemical Society*, 131(43):15630–15632, 2009.

[94] J. R. Weinberg-Wolf, L. E. McNeil, S. Liu, and C. Kloc. Evidence of low intermolecular coupling in rubrene single crystals by Raman scattering. *Journal of Physics: Condensed Matter*, 19(27):276204, 2007.

[95] Nist, http://cccbdb.nist.gov/vibscalejust.asp. [Online; accessed 2017-09-19].

[96] K. A. McGarry, W. Xie, C. Sutton, C. Risko, Y. Wu, V. G. Young, J. L. Brédas, C. D. Frisbie, and C. J. Douglas. Rubrene-based single-crystal organic semiconductors: Synthesis, electronic structure, and charge-transport properties. *Chemistry of Materials*, 25(11):2254–2263, 2013.

[97] W. Xie, K. A. McGarry, F. Liu, Y. Wu, P. P. Ruden, C. J. Douglas, and C. D. Frisbie. High-mobility transistors based on single crystals of isotopically substituted rubrene- d_{28}. *Journal of Physical Chemistry C*, 117(22):11522–11529, 2013.

[98] Z. Zhang, W. A. Ogden, V. G. Young, and C. J. Douglas. Synthesis, electrochemical properties, and crystal packing of perfluororubrene. *Chemical Communications*, 52(52):8127–8130, 2016.

[99] X. Ren, M. J. Bruzek, D. A. Hanifi, A. Schulzetenberg, Y. Wu, C. H. Kim, Z. Zhang, J. E. Johns, A. Salleo, S. Fratini, A. Troisi, C. J. Douglas, and C. D. Frisbie. Negative isotope effect on field-effect hole transport in fully substituted ^{13}C-rubrene. *Advanced Electronic Materials*, 3(4):1–7, 2017.

[100] M. A. Green. Commercial progress and challenges for photovoltaics. *Nature Energy*, 1(15015), 1 2016.

[101] O. E. Semonin, J. M. Luther, S. Choi, H. Y. Chen, J. Gao, A. J. Nozik, and M. C. Beard. Peak external photocurrent quantum efficiency exceeding 100% via MEG in a quantum dot solar cell. *Science*, 334(6062):1530–1533, 12 2011.

[102] Q. Ye and C. Chi. Recent highlights and perspectives on acene based molecules and materials. *Chemistry of Materials*, 26(14):4046–4056, 7 2014.

[103] A. A. Bakulin, S. E. Morgan, T. B. Kehoe, M. W. B. Wilson, A. W. Chin, D. Zigmantas, D. Egorova, and A. Rao. Real-time observation of multiexcitonic states in ultrafast singlet fission using coherent 2D electronic spectroscopy. *Nature Chemistry*, 8(1):16–23, 1 2016.

[104] S. N. Sanders, A. B. Pun, K. R. Parenti, E. Kumarasamy, L. M. Yablon, M. Y. Sfeir, and L. M. Campos. Understanding the bound triplet-pair state in singlet fission. *Chem*, 5(8):1988–2005, 2019.

[105] C. K. Yong, A. J. Musser, S. L. Bayliss, S. Lukman, H. Tamura, O. Bubnova, R. K. Hallani, A. Meneau, R. Resel, M. Maruyama, S. Hotta, L. M. Herz, D. Beljonne, J. E. Anthony, J. Clark, and H. Sirringhaus. The entangled

triplet pair state in acene and heteroacene materials. *Nature Communications*, 8(12), 2017.

[106] J. Zheng, Y. Xie, S. Jiang, and Z. Lan. Ultrafast nonadiabatic dynamics of singlet fission: Quantum dynamics with the multilayer multiconfigurational time-dependent hartree (ML-MCTDH) method. *The Journal of Physical Chemistry C*, 120(3):1375–1389, 1 2016.

[107] G. B. Piland, J. J. Burdett, R. J. Dillon, and C. J. Bardeen. Singlet fission : From coherences to kinetics singlet fission : from coherences to kinetics. *Journal of Physical Chemistry Letters*, 5:2312–2319, 2014.

[108] T. Sakuma, H. Sakai, Y. Araki, T. Mori, T. Wada, V. N. Tkachenko, and T. Hasobe. Long-lived triplet excited states of bent-shaped pentacene dimers by intramolecular singlet fission. *Journal of Physical Chemistry A*, 120(11):1867–1875, 2016.

[109] A. B. Kolomeisky, X. Feng, and A. I. Krylov. A simple kinetic model for singlet fission: A role of electronic and entropic contributions to macroscopic rates. *Journal of Physical Chemistry C*, 118(10):5188–5195, 2014.

[110] K. M. Felter and F. C. Grozema. Singlet fission in crystalline organic materials: Recent insights and future directions. *Journal of Physical Chemistry Letters*, 10(22):7208–7214, 11 2019.

[111] K. C. Krishnapriya, A. J. Musser, and S. Patil. Molecular design strategies for efficient intramolecular singlet exciton fission. *ACS Energy Letters*, 4(1):192–202, 1 2019.

[112] A. K. Pandey and J. M. Nunzi. Rubrene/fullerene heterostructures with a half-gap electroluminescence threshold and large photovoltage. *Advanced Materials*, 19(21):3613–3617, 11 2007.

[113] R. Zeis, C. Besnard, T. Siegrist, C. Schlockermann, X. Chi, and C. Kloc. Field effect studies on rubrene and impurities of rubrene. *Chemistry of Materials*, 18(2):244–248, 2006.

[114] M. Ullah, S. D. Yambem, E. G. Moore, E. B. Namdas, and A. K. Pandey. Singlet fission and triplet exciton dynamics in rubrene/fullerene heterojunctions: Implications for electroluminescence. *Advanced Electronic Materials*, 1:1500229–1500238, 2015.

[115] V. Jankus, E. W. Snedden, D. W. Bright, E. Arac, D. Dai, and A. P. Monkman. Competition between polaron pair formation and singlet fission observed in amorphous rubrene films. *Physical Review B*, 87:224202, 2013.

[116] Y. Zhang, Y. Lei, Q. Zhang, and Z. Xiong. Thermally activated singlet exciton fission observed in rubrene doped organic films. *Organic Electronics*, 15(2):577–581, 2014.

[117] A SciFinder search was conducted on May 22, 2020 using rubrene as the starting structure. Ring fusions on the tetracene core were excluded. The search was also refined to exclude metal-containing substances and structures without references. SciFinder - Sign In https://sso.cas.org/as/fCQv5/resume/as/authorization.ping. [Online; accessed 2020-06-01].

[118] J. A. Dodge, J. D. Bain, and A. R. Chamberlin. Regioselective synthesis of substituted rubrenes. *Journal of Organic Chemistry*, 55(13):4190–4198, 1990.

[119] A. S. Paraskar, A. R. Reddy, A. Patra, Y. H. Wijsboom, O. Gidron, L. J. W. Shimon, G. Leitus, and M. Bendikov. Rubrenes: Planar and twisted. *Chemistry - A European Journal*, 14(34):10639–10647, 11 2008.

[120] D. Braga, A. Jaafari, L. Miozzo, M. Moret, S. Rizzato, A. Papagni, and A. Yassar. The rubrenic synthesis: The delicate equilibrium between tetracene and cyclobutene. *European Journal of Organic Chemistry*, 2011(22):4160–4169, 8 2011.

[121] Y. Sakamoto and T. Suzuki. Perfluorinated and half-fluorinated rubrenes: Synthesis and crystal packing arrangements. *Journal of Organic Chemistry*, 82(15):8111–8116, 8 2017.

[122] C. Sutton, N. R. Tummala, D. Beljonne, and J. L. Brédas. Singlet fission in rubrene derivatives: Impact of molecular packing. *Chemistry of Materials*, 29(7):2777–2787, 2017.

[123] T. K. Mullenbach, K. A. McGarry, W. A. Luhman, C. J. Douglas, and R. J. Holmes. Connecting molecular structure and exciton diffusion length in rubrene derivatives. *Advanced Materials*, 25(27):3689–3693, 2013.

[124] A. A. Cassabaum, W. R. Silva, C. C. Rich, and R. R. Frontiera. Orientation and polarization dependence of ground- and excited-state FSRS in

crystalline betaine-30. *The Journal of Physical Chemistry C*, 123(20):12563–12572, 5 2019.

[125] K. Bera, S. Y. Kwang, A. A. Cassabaum, C. C. Rich, and R. R. Frontiera. Facile background discrimination in femtosecond stimulated Raman spectroscopy using a dual-frequency Raman pump technique. *Journal of Physical Chemistry A*, 123(37):7932–7939, 9 2019.

[126] M. J. Frisch, G. W. Trucks, H. B. Schlegel, G. E. Scuseria, M. A. Robb, J. R. Cheeseman, G. Scalmani, V. Barone, G. A. Petersson, H. Nakatsuji, X. Li, M. Caricato, A. V. Marenich, J. Bloino, B. G. Janesko, R. Gomperts, B. Mennucci, H. P. Hratchian, J. V. Ortiz, A. F. Izmaylov, J. L. Sonnenberg, D. Williams-Young, F. Ding, F. Lipparini, F. Egidi, J. Goings, B. Peng, A. Petrone, T. Henderson, D. Ranasinghe, V. G. Zakrzewski, J. Gao, N. Rega, G. Zheng, W. Liang, M. Hada, M. Ehara, K. Toyota, R. Fukuda, J. Hasegawa, M. Ishida, T. Nakajima, Y. Honda, O. Kitao, H. Nakai, T. Vreven, K. Throssell, and D. J. Montgo. Gaussian 16, Revision C.01, 2016. [Online; accessed 2020-03-06].

[127] S. Mukamel and J. D. Biggs. Communication: Comment on the effective temporal and spectral resolution of impulsive stimulated Raman signals. *Journal of Chemical Physics*, 134(16):161101, 4 2011.

[128] D. W. McCamant. Re-evaluation of rhodopsin's relaxation kinetics determined from femtosecond stimulated Raman lineshapes. *Journal of Physical Chemistry B*, 115(29):9299–9305, 7 2011.

[129] H. Kuramochi, S. Takeuchi, K. Yonezawa, H. Kamikubo, M. Kataoka, and T. Tahara. Probing the early stages of photoreception in photoactive yellow protein with ultrafast time-domain Raman spectroscopy. *Nature Chemistry*, 9(7):660–666, 2017.

[130] D. W. McCamant, P. Kukura, and R. A. Mathies. Femtosecond broadband stimulated Raman: A new approach for high-performance vibrational spectroscopy. *Applied Spectroscopy*, 57(11):1317–1323, 2003.

[131] R. R. Frontiera, S. Shim, and R. A. Mathies. Origin of negative and dispersive features in anti-stokes and resonance femtosecond stimulated Raman spectroscopy. *Journal of Chemical Physics*, 129:064507, 2008.

[132] Z. Sun, J. Lu, D. H. Zhang, and S.-Y. Lee. Quantum theory of (femtosecond) time-resolved stimulated Raman scattering. *The Journal of Chemical Physics*, 128(14):144114, 2008.

[133] B. G. Oscar, C. Chen, W. Liu, L. Zhu, and C. Fang. Dynamic Raman line shapes on an evolving excited-state landscape: Insights from tunable femtosecond stimulated Raman spectroscopy. *Journal of Physical Chemistry A*, 121(29):5428–5441, 2017.

[134] S. Shim, J. Dasgupta, and R. A. Mathies. Femtosecond time-resolved stimulated Raman reveals the birth of bacteriorhodopsin's J and K intermediates. *Journal of the American Chemical Society*, 131(22):7592–7597, 2009.

[135] P. Kukura, D. W. McCamant, and R. A. Mathies. Femtosecond time-resolved stimulated Raman spectroscopy of the S_2 ($^1B_u^+$) excited state of beta-carotene. *Journal of Physical Chemistry A*, 108(28):5921–5925, 2004.

[136] A. Weigel, A. Dobryakov, B. Klaumünzer, M. Sajadi, P. Saalfrank, and N. P. Ernsting. Femtosecond stimulated Raman spectroscopy of flavin after optical excitation. *Journal of Physical Chemistry B*, 115(13):3656–3680, 2011.

[137] A. Weigel and N. P. Ernsting. Excited stilbene : Intramolecular vibrational redistribution and solvation studied by femtosecond stimulated Raman spectroscopy. *Journal of Physical Chemistry B*, 114:7879–7893, 2010.

[138] E. M. Grumstrup, Z. Chen, R. P. Vary, A. M. Moran, K. S. Schanze, and J. M. Papanikolas. Frequency modulated femtosecond stimulated Raman spectroscopy of ultrafast energy transfer in a donor-acceptor copolymer. *Journal of Physical Chemistry B*, 117(27):8245–8255, 2013.

[139] M. Kloz, v. R. Grondelle, and J. T. Kennis. Wavelength-modulated femtosecond stimulated Raman spectroscopy—approach towards automatic data processing. *Physical Chemistry Chemical Physics*, 13(40):18123, 2011.

[140] M. Kloz, J. Weißenborn, T. Polívka, H. A. Frank, and J. T. M. Kennis. Spectral watermarking in femtosecond stimulated Raman spectroscopy: resolving the nature of the carotenoid S* state. *Physical Chemistry Chemical Physics*, 18(21):14619–14628, 2016.

[141] S. T. McCain, R. M. Willett, and D. J. Brady. Multi-excitation Raman spectroscopy technique for fluorescence rejection. *Optics Express*, 16(15):10975, 2008.

[142] P. A. Mosier-Boss, S. H. Lieberman, and R. Newbery. Fluorescence rejection in Raman spectroscopy by shifted-spectra, edge detection, and FFT filtering techniques. *Applied Spectroscopy*, 49(5):630–638, 1995.

[143] J. Zhao, M. M. Carrabba, and F. S. Allen. Automated fluorescence rejection using shifted excitation Raman difference spectroscopy. *Applied Spectroscopy*, 56(7):834–845, 2002.

[144] A. P. Shreve, N. J. Cherepy, and R. A. Mathies. Effective rejection of fluorescence interference in Raman spectroscopy using a shifted excitation difference technique. *Applied Spectroscopy*, 46(4):707–711, 1992.

[145] K. Sowoidnich and H. D. Kronfeldt. Fluorescence rejection by shifted excitation Raman difference spectroscopy at multiple wavelengths for the investigation of biological samples. *Applied Physics B: Lasers and Optics*, 108(4):975–982, 2012.

[146] M. T. Gebrekidan, C. Knipfer, F. Stelzle, J. Popp, S. Will, and A. Braeuer. A shifted-excitation Raman difference spectroscopy (SERDS) evaluation strategy for the efficient isolation of Raman spectra from extreme fluorescence interference. *Journal of Raman Spectroscopy*, 47(2):198–209, 2016.

[147] J. B. Cooper, S. Marshall, R. Jones, M. Abdelkader, and K. L. Wise. Spatially compressed dual-wavelength excitation Raman spectrometer. *Applied Optics*, 53(15):3333, 2014.

[148] M. Maiwald, B. Sumpf, and G. Tränkle. Rapid and adjustable shifted excitation Raman difference spectroscopy using a dual-wavelength diode laser at 785 nm. *Journal of Raman Spectroscopy*, 49(11):1765–1775, 2018.

[149] E. Cordero, F. Korinth, C. Stiebing, C. Krafft, I. W. Schie, and J. Popp. Evaluation of shifted excitation Raman difference spectroscopy and comparison to computational background correction methods applied to biochemical Raman spectra. *Sensors*, 17(8):1724, 2017.

[150] M. Maiwald, A. Müller, B. Sumpf, G. Erbert, and G. Tränkle. Capability of shifted excitation Raman difference spectroscopy under ambient daylight. *Applied Optics*, 54(17):5520–5524, 2015.

[151] J. Zhao, H. Lui, Lean, M. David, and H. Zeng. Automated autofluorescence background subtraction algorithm for biomedical Raman spectroscopy. *Applied Spectroscopy*, 61(11):1225–1232, 2007.

[152] P. M. Kearns, Z. Sohrabpour, and A. M. Massari. Frequency comb SFG: a new approach to multiplex detection. *Optics Express*, 24(17):19863–19870, 2016.

[153] P. Matousek, M. Towrie, and A. W. Parker. Fluorescence background suppression in Raman spectroscopy using combined kerr gated and shifted excitation Raman difference techniques. *Journal of Raman Spectroscopy*, 33(4):238–242, 2002.

[154] H. Ahmad. *Gold substrates for SERS and SERS/SERDS measurements in seawater and Raman measurements through long optical fibers, Technische Universitat Berlin*. PhD thesis, 2014.

[155] H. Schmidt, D. P. Kaiser, and M. Maiwald. Method for generating and for detecting a Raman spectrum. *U.S. Patent US8310672*, 2012.

[156] S. Guo, O. Chernavskaia, J. Popp, and T. Bocklitz. Spectral reconstruction for shifted-excitation Raman difference spectroscopy (SERDS). *Talanta*, 186:372–380, 2018.

[157] P. Matousek, M. Towrie, and A. W. Parker. Simple reconstruction algorithm for shifted excitation Raman difference spectroscopy. *Applied Spectroscopy*, 59(6):848–851, 2005.

[158] S. Y. Kwang. GitHub - kwangsiuyi/dual-raman-auto-reconstruction: Igor macro for the auto-reconstruction of a Raman spectrum from SERDS. [Online; accessed 2019-02-11].

[159] H. M. Kim, H. Kim, I. Yang, S. M. Jin, and Y. D. Suh. Time-gated preresonant femtosecond stimulated Raman spectroscopy of diethylthiatricarbocyanine iodide. *Physical Chemistry Chemical Physics*, 16(11):5312–5318, 2 2014.

[160] W. R. Silva, E. L. Keller, and R. R. Frontiera. Determination of resonance Raman cross-sections for use in biological SERS sensing with femtosecond stimulated Raman spectroscopy. *Analytical Chemistry*, 86(15):7782–7787, 8 2014.

[161] R. R. Frontiera, N. L. Gruenke, and R. P. Van Duyne. Fano-like resonances arising from long-lived molecule-plasmon interactions in colloidal nanoantennas. *Nano Letters*, 12(11):5989–5994, 11 2012.

[162] C. Reese and Z. Bao. Organic single-crystal field-effect transistors. *Materials Today*, 10(3):20–27, 2007.

[163] A. L. Briseno, R. J. Tseng, M. M. Ling, E. H. L. Falcao, Y. Yang, F. Wudl, and Z. Bao. High-performance organic single-crystal transistors on flexible substrates. *Advanced Materials*, 18(17):2320–2324, 2006.

[164] V. C. Sundar, J. Zaumseil, V. Podzorov, E. Menard, R. L. Willett, T. Someya, M. E. Gershenson, and J. A. Rogers. Elastomeric transistor stamps: Reversible probing of charge transport in organic crystals. *Science*, 303(5664):1644–1646, 2004.

[165] T. Hasegawa and J. Takeya. Organic field-effect transistors using single crystals. *Science and Technology of Advanced Materials*, 10(2):024314–024331, 2009.

[166] S. Karak, J. A. Lim, S. Ferdous, V. V. Duzhko, and A. L. Briseno. Photovoltaic effect at the Schottky interface with organic single crystal rubrene. *Advanced Functional Materials*, 24(8):1039–1046, 2014.

[167] M. Uchida, C. Adachi, T. Koyama, and Y. Taniguchi. Charge carrier trapping effect by luminescent dopant molecules in single-layer organic light emitting diodes. *Journal of Applied Physics*, 86(3):1680, 1999.

[168] Y. Shao and Y. Yang. White organic light-emitting diodes prepared by a fused organic solid solution method. *Applied Physics Letters*, 86(7):1–3, 2005.

[169] W. Jia, Q. Chen, L. Chen, D. Yuan, J. Xiang, Y. Chen, and Z. Xiong. Molecular spacing modulated conversion of singlet fission to triplet fusion in rubrene-based organic light-emitting diodes at ambient temperature. *The Journal of Physical Chemistry C*, 120(15):8380–8386, 2016.

[170] A. Girlando, M. Masino, A. Brillante, T. Toccoli, and S. Iannotta. Raman identification of polymorphs in pentacene films. *Crystals*, 6(4):41, 4 2016.

[171] I. Marcaida, M. Maguregui, H. Morillas, M. Veneranda, N. Prieto-Taboada, S. Fdez-Ortiz de Vallejuelo, and J. M. Madariaga. Raman microscopy as a tool to discriminate mineral phases of volcanic origin and contaminations on red and yellow ochre raw pigments from pompeii. *Journal of Raman Spectroscopy*, 50(2):143–149, 2 2019.

[172] L. Huang, Q. Liao, Q. Shi, H. Fu, J. Ma, and J. Yao. Rubrene micro-crystals from solution routes: their crystallography, morphology and optical properties. *Journal of Materials Chemistry*, 20(1):159–166, 2010.

[173] S. Bergantin and M. Moret. Rubrene polymorphs and derivatives: The effect of chemical modification on the crystal structure. *Crystal Growth & Design*, 12:6035–6041, 2012.

[174] Z.-P. Fan and H.-L. Zhang. Crystal polymorph control for high-performance organic field-effect transistors. In *Integrated Circuits/Microchips [Working Title]*. IntechOpen, 4 2020.

[175] V. Podzorov, E. Menard, A. Borissov, V. Kiryukhin, J. A. Rogers, and M. E. Gershenson. Intrinsic charge transport on the surface of organic semiconductors. *Physical Review Letters*, 93(8):1–4, 2004.

[176] H. Najafov, B. Lyu, I. Biaggio, and V. Podzorov. Investigating the origin of the high photoconductivity of rubrene single crystals. *Physical Review B*, 77(12):1–12, 2008.

[177] J. E. Anthony. The larger acenes: Versatile organic semiconductors. *Angewandte Chemie - International Edition*, 47(3):452–483, 2008.

[178] X. Wang, T. Garcia, S. Monaco, B. Schatschneider, and N. Marom. Effect of crystal packing on the excitonic properties of rubrene polymorphs. *CrystEngComm*, 18:7353–7362, 2016.

[179] J. Socci, T. Salzillo, R. G. Della Valle, E. Venuti, and A. Brillante. Fast identification of rubrene polymorphs by lattice phonon Raman microscopy. *Solid State Sciences*, 71:146–151, 9 2017.

[180] J. N. Schrauben, J. L. Ryerson, J. Michl, and J. C. Johnson. Mechanism of singlet fission in thin films of 1,3-diphenylisobenzofuran. *Journal of the American Chemical Society*, 136(20):7363–7373, 2014.

[181] J. C. Johnson and J. Michl. 1,3-diphenylisobenzofuran: a model chromophore for singlet fission. *Topics in Current Chemistry*, 375(5), 2017.

[182] J. L. Ryerson, J. N. Schrauben, A. J. Ferguson, S. C. Sahoo, P. Naumov, Z. Havlas, J. Michl, A. J. Nozik, and J. C. Johnson. Two thin film polymorphs of the singlet fission compound 1,3-diphenylisobenzofuran. *Journal of Physical Chemistry C*, 118(23):12121–12132, 2014.

[183] J. C. Johnson, A. J. Nozik, and J. Michl. High triplet yield from singlet fission in a thin film of 1,3-diphenylisobenzofuran. *Journal of the American Chemical Society*, 132(46):16302–16303, 11 2010.

[184] A. F. Schwerin, J. C. Johnson, M. B. Smith, P. Sreearunothai, D. Popović, J. Černý, Z. Havias, I. Paci, A. Akdag, M. K. MacLeod, X. Chen, D. E. David, M. A. Ratner, J. R. Miller, A. J. Nozik, and J. Michl. Toward designed singlet fission: Electronic states and photophysics of 1,3-diphenylisobenzofuran. *Journal of Physical Chemistry A*, 114(3):1457–1473, 1 2010.

[185] E. Venuti, I. Bilotti, D. R. G. Valle, A. Brillante, P. Ranzieri, M. Masino, and A. Girlando. Polarized Raman spectra of a rubrene single crystal. *Journal of Physical Chemistry C*, 112:17416–17422, 2008.

Appendix A

Supporting Information for Chapter 3: Femtosecond Raman Microscopy Reveals Structural Dynamics Leading to Triplet Separation in Rubrene Singlet Fission

A.1 Low frequency Raman spectrum of rubrene crystal

We show the low frequency spontaneous Raman spectrum of the rubrene crystal used for FSRS in Figure A.1. The low frequency Raman modes depicted in the figure correspond to the orthorhombic polymorph of crystalline rubrene. [185] We use the low frequency Raman modes to determine the orientation of the crystal for the spontaneous Raman measurements. Comparing the frequencies and relative intensities of the phonon modes at 72, 104, 116 and 136 cm^{-1} with ref [185], we

determine that the Raman excitation is normal to the *ab* face of the needle for the spontaneous Raman measurements.

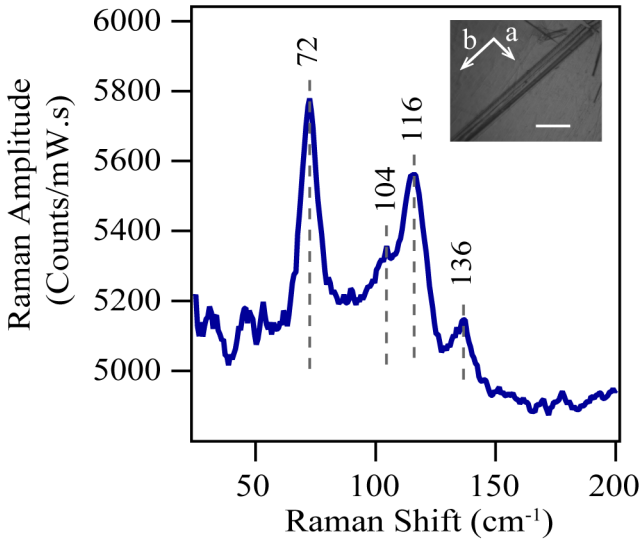

Figure A.1: Low frequency Raman spectrum of a rubrene crystal (inset) with prominent peaks indicated by dashed lines. The scale bar is 0.4 mm in length.

A.2 Photoluminescence Spectrum

We measured PL spectrum of the needle shaped rubrene crystal to verify if the crystal is pristine or not. We obtained the PL spectrum on the same continuous wave Raman set-up as described previously and plot the same in Figure A.2. We collected the PL spectrum in 6 separate detection windows causing a slight overlap as visible in Figure A.2. The absence of the 650 nm peak in our PL spectra indicates that we cannot detect any impurities. [72, 74]

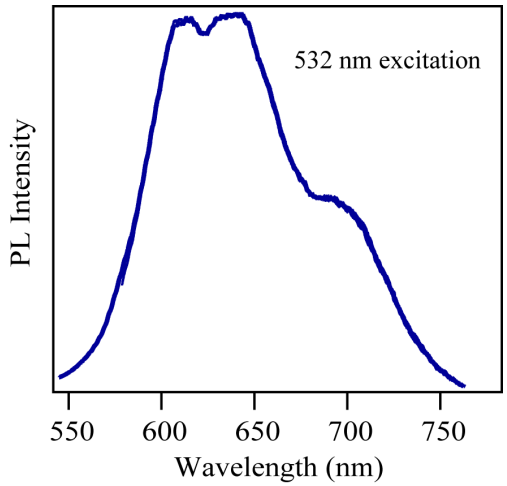

Figure A.2: PL spectrum of the needle shaped crystalline rubrene. Absence of 650 nm peak implies that the crystal is pristine.

A.3 Photoexcitation pump profile

The spectrum of the photoexcitation pump is shown in Figure A.3.

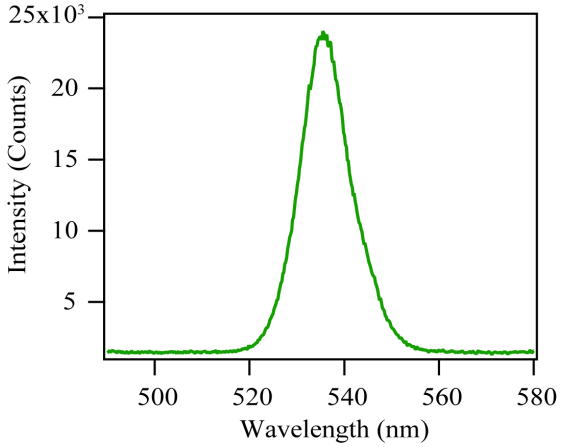

Figure A.3: Spectral profile of the photoexcitation pump.

A.4 Raw FSR data of crystalline rubrene

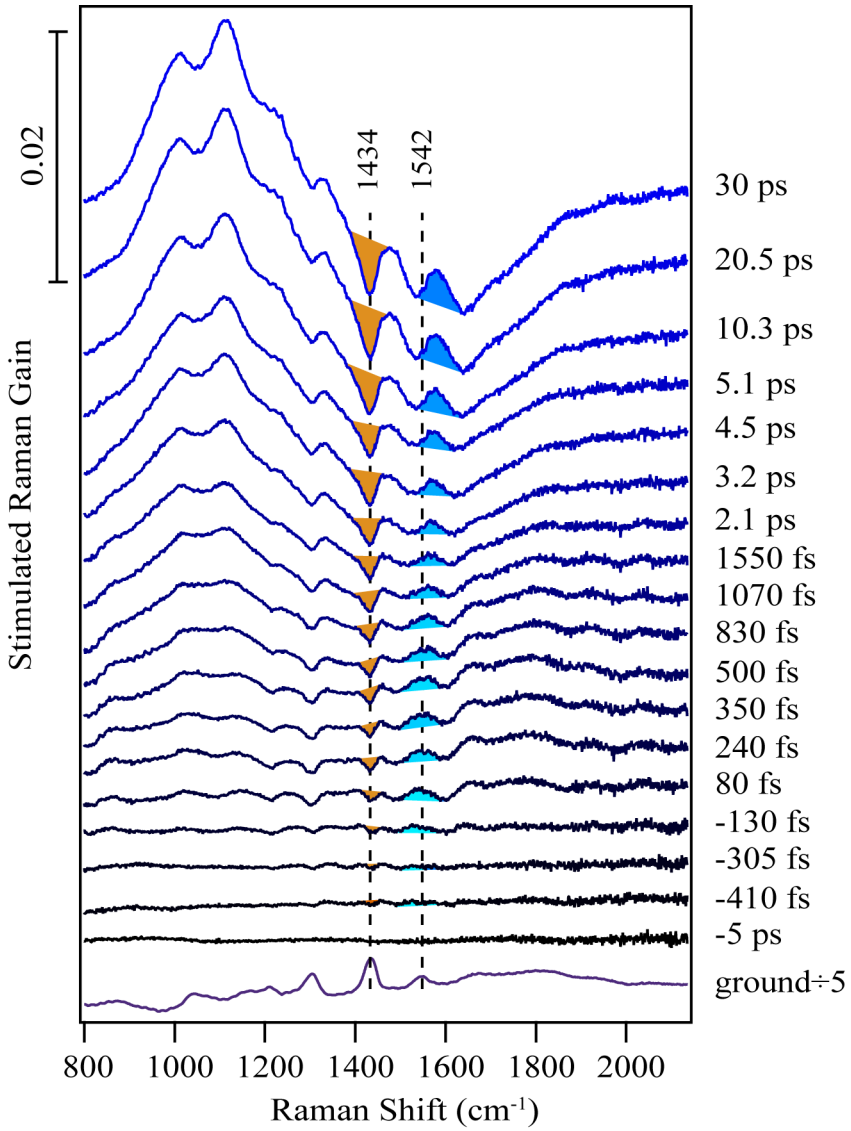

Figure A.4: Raw FSR spectra of crystalline rubrene at various time delays after photoexcitation. The shaded region indicates the ground state depletion (brown) and one of the excited state features (blue).

We plot the FSR data of crystalline rubrene after one to one subtraction of the excited state spectra from the ground state spectrum in Figure A.4. The ground state Raman spectrum of rubrene has peaks at 1210, 1305 and 1434 cm^{-1} corresponding to C–C stretching motions in the tetracene backbone and C–H wagging motions in rubrene molecule according to our DFT calculations, and are depleted in amplitude following photoexcitation.

A.5 Kinetics of ground state addition

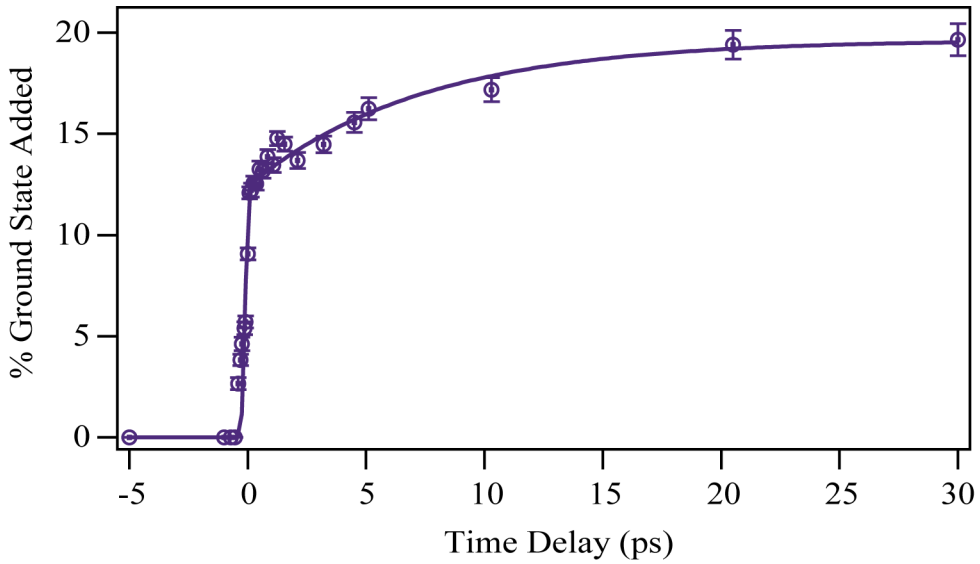

Figure A.5: Time resolved kinetics of the percentage of ground state added back to the excited state spectra with corresponding exponential fit.

The large depletion of the ground state peaks in the excited state spectra demanded the addition of ground state spectrum to unambiguously examine the excited state dynamics. We add the ground state back to the excited state difference spectra until no negative features of any of the ground state peaks are

present. We show the spectra obtained after the addition of ground state to the excited state spectra in Figure 3.2 of the main text. Figure A.5 shows the kinetics of the amount of ground state added back to the excited state spectrum, which is in agreement with the rapid formation of the correlated triplet pair and subsequent long-lived triplet states.

A.6 Transient absorption data of rubrene crystal

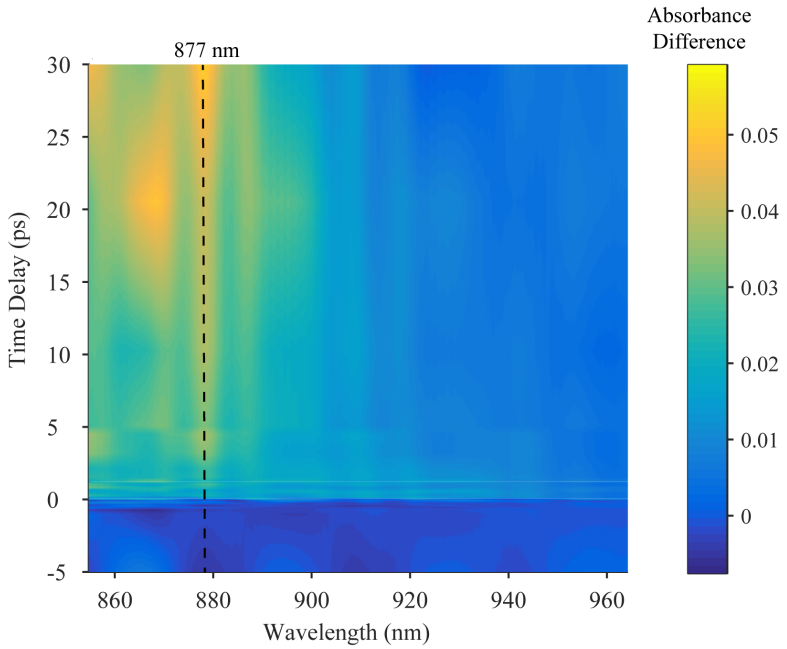

Figure A.6: Transient absorption plot of rubrene crystal. The intensity of the peak at 877 nm increases with time indicating it to be an excited state absorption feature.

We plot the transient absorption spectra with the Raman pump off in Figure A.6. The intensity of the 877 nm peak in the transient absorption increases as a

function of time indicating it to be an excited state absorption feature. This peak in transient absorption corresponds to the 1117 cm^{-1} peak in FSRS from Figure 3.2.

A.7 Excited state vibrational linewidths

We fit the peaks around 1430 and 1542 cm^{-1} in Figure 3.2 from the main text to a single Gaussian with a linear baseline. The linewidths of the fit as a function of time is presented in Figure A.7. We see no trend in the linewidths and thus this discards the possibility of vibrational cooling being the origin of the frequency evolution.

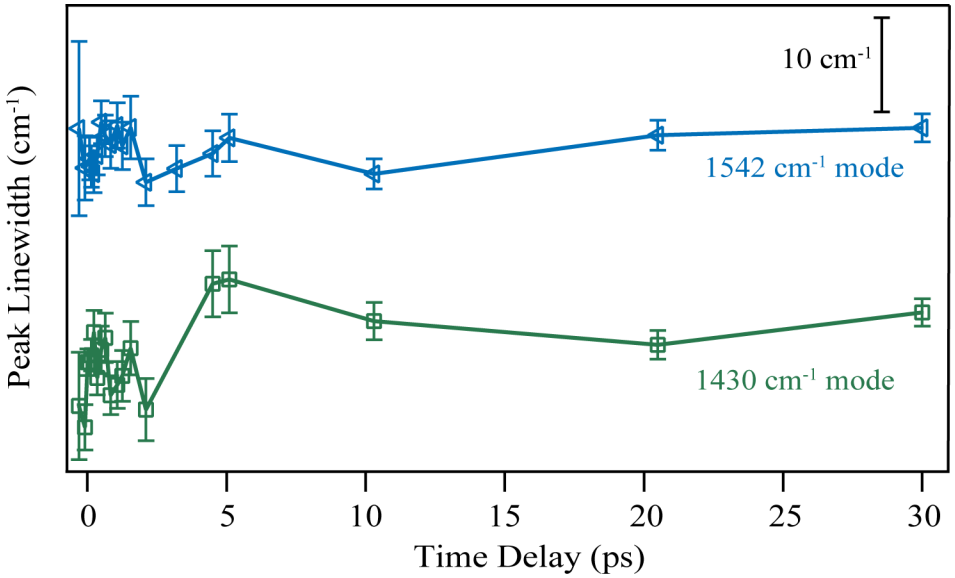

Figure A.7: The linewidths obtained from the fit of the peaks around 1430 and 1542 cm^{-1} as a function of time.

A.8 Raman pump power dependence

We conducted Raman pump power dependence where the photoexcitation pump power in these experiments was 110 µW and the Raman pump power was between 25 – 188 µW. The Raman gain of the peak around 1430 cm^{-1} at time delay of 1070 fs as a function of Raman pump power is plotted in the figure below. The linear fit below has a r^2 value of 0.996 which shows that the excited state peaks are in the linear regime with respect to the Raman pump power.

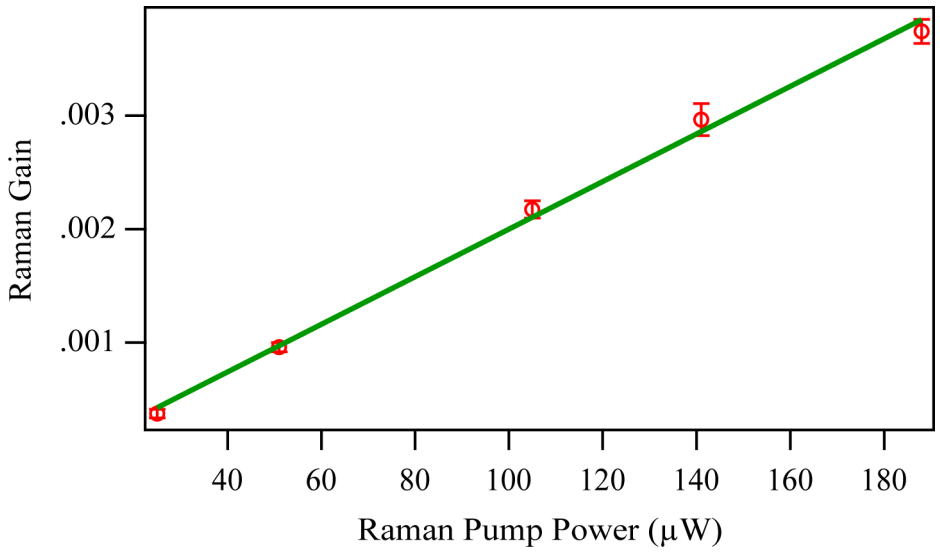

Figure A.8: Raman gain with linear fit of the peak around 1430 cm^{-1} at time delay of 1070 fs.

A.9 Photoexcitation power dependence

We conducted a photoexcitation pump power dependence where the Raman pump power was 110 µW and the power of the photoexcitation pump was between 13.5 – 270 µW. We plot the Raman gain of the peak around 1430 cm^{-1} at time

delay of 1070 fs as a function of photoexcitation pump power in the figure below. The Raman gain shows a power dependence on the photoexcitation pump power, which indicates the presence of exciton-exciton annihilation. The existence of some exciton-exciton annihilation will affect the overall triplet yield, but does not affect the observed structural dynamics that we see for the molecules that do reach the triplet state.

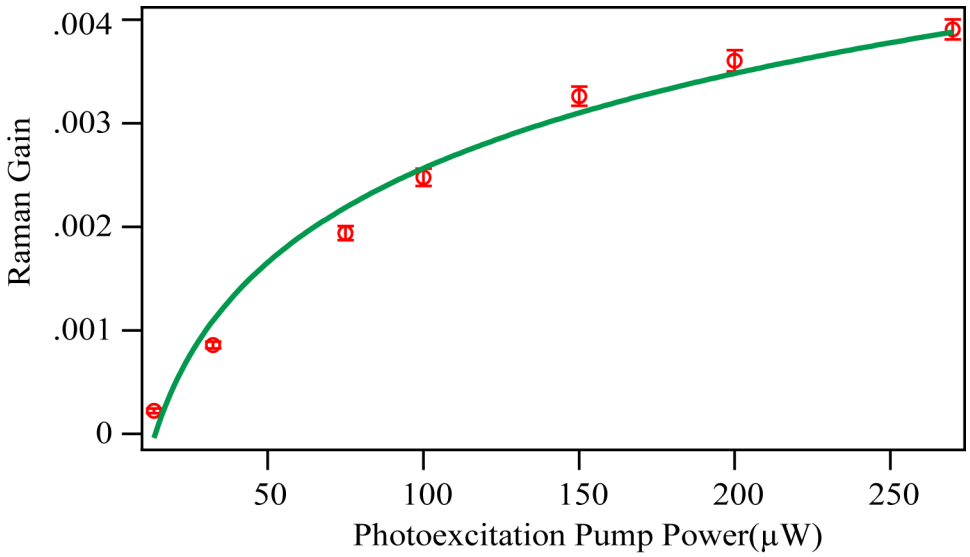

Figure A.9: Raman gain with power law fit of the peak around 1430 cm^{-1} at time delay of 1070 fs.

A.10 Raman spectra of three forms of rubrene

To probe the difference between powder and crystalline states on the fingerprint region vibrational frequencies, we measured the spontaneous Raman spectrum of rubrene single crystal, rubrene powder and rubrene solution in chloroform. From the plot below, we do not see any shift in the frequencies of the high energy

vibrational modes.

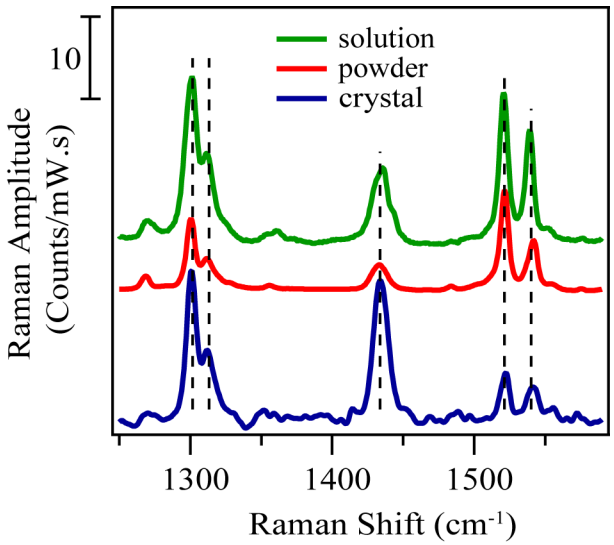

Figure A.10: Spontaneous Raman spectra of rubrene single crystal, rubrene powder and rubrene solution in chloroform demonstrates that the mode frequencies do not change in the fingerprint region.

A.11 FSR data of rubrene solution in chloroform

To verify that the features in the FSR data of crystalline rubrene arises from singlet fission, we performed FSR studies on rubrene solution in chloroform, which is known to not undergo singlet fission. [71] We plot the FSR data after one to one subtraction of the excited state spectra from the ground state spectrum in Figure A.11 and the transient absorption data in Figure A.12. From the FSR and TA data below, we confirm that the interesting transient features visible in the FSR data of the crystalline rubrene arises due to singlet fission process.

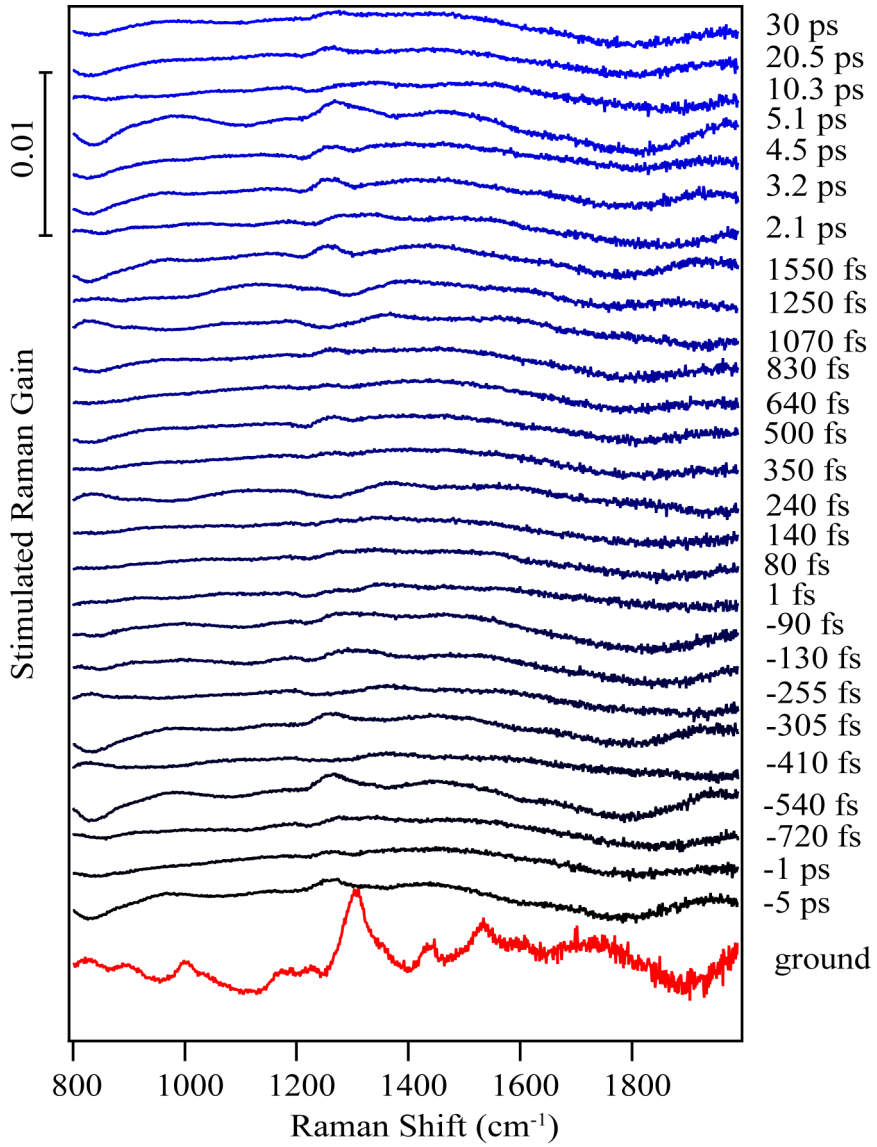

Figure A.11: FSR data of rubrene solution in chloroform after one to one subtraction of the excited state spectra from the ground state spectrum.

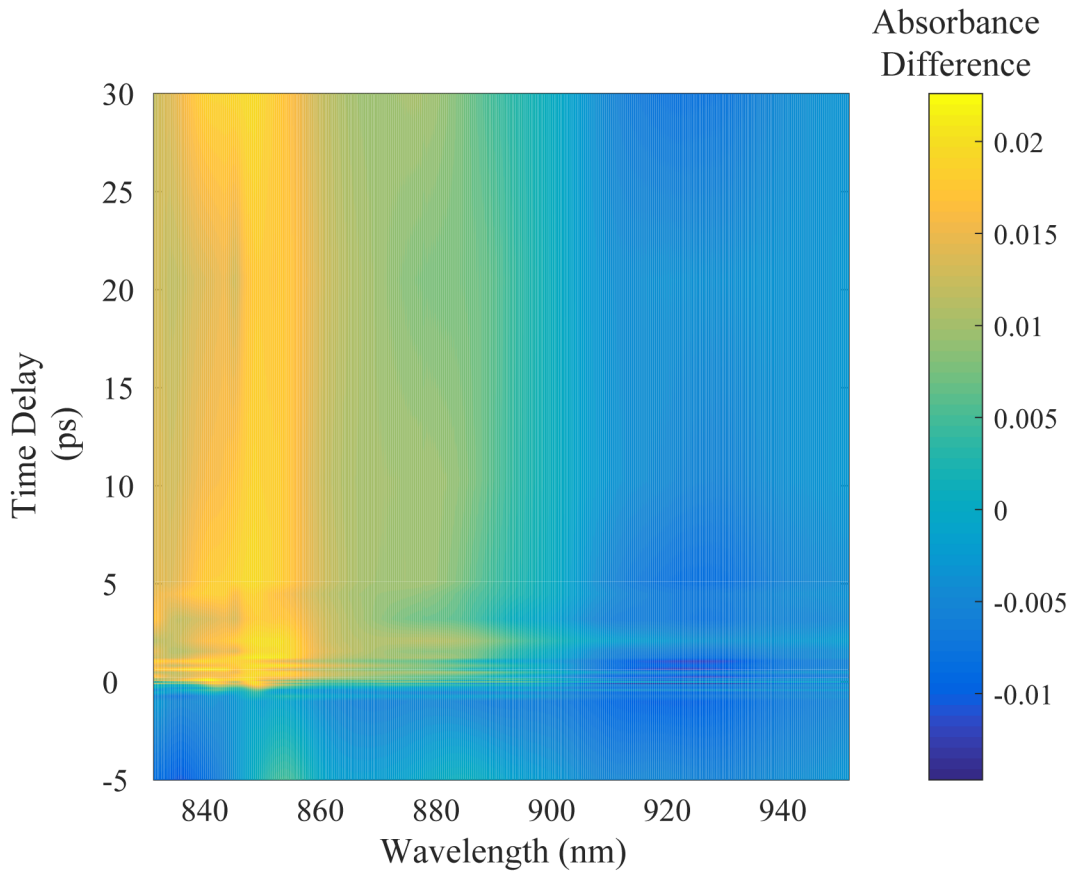

Figure A.12: Transient absorption plot of rubrene solution in chloroform. The absence of 877 nm peak here confirms that the assignment of the crystalline rubrene features in the main text to dynamics resulting from singlet fission are correct.

A.12 DFT calculations

We performed DFT calculations for the geometry optimization and Raman frequencies of neutral, anion and cation states of rubrene. Orthorhombic rubrene crystallizes with a planar tetracene backbone. [96, 119] The scaled vibrational frequencies obtained from the calculations are reported in Table 3.2 in the main text. The converged energy values are listed in Table A.1 and the coordinates of the optimized geometries are present in Tables A2–A4.

Table A.1: Calculated energies.

Rubrene state	Energy (Hartree)
Neutral	-1617.711601
Anion	-1617.763636
Cation	-1617.487549

Table A.2: Optimized geometry of neutral rubrene.

Atom	X	Y	Z
C	0	0	0.73673
C	1.246764	0.103583	1.427113
C	2.431637	0.378387	0.722315
C	3.687371	0.573499	1.396573
C	4.845707	0.790501	0.711274
C	1.413312	-0.26774	2.872973
C	1.609597	0.675259	3.887569
C	1.881834	0.271375	5.192337
C	1.973538	-1.084377	5.504531
C	1.78951	-2.033185	4.500959
C	1.51482	-1.626437	3.197005
H	3.706663	0.555988	2.476286
H	5.772252	0.9516	1.251011
H	1.541614	1.731119	3.653558
H	2.021997	1.017698	5.966467
H	2.189346	-1.397283	6.520023
H	1.866484	-3.090639	4.729875

H	1.385537	-2.368107	2.416154
C	-1.246764	-0.103583	1.427113
C	-2.431637	-0.378387	0.722315
C	-3.687371	-0.573499	1.396573
C	-4.845707	-0.790501	0.711274
C	-1.413312	0.26774	2.872973
C	-1.609597	-0.675259	3.887569
C	-1.881834	-0.271375	5.192337
C	-1.973538	1.084377	5.504531
C	-1.78951	2.033185	4.500959
C	-1.51482	1.626437	3.197005
H	-3.706663	-0.555988	2.476286
H	-5.772252	-0.9516	1.251011
H	-1.541614	-1.731119	3.653558
H	-2.021997	-1.017698	5.966467
H	-2.189346	1.397283	6.520023
H	-1.866484	3.090639	4.729875
H	-1.385537	2.368107	2.416154
C	0	0	-0.73673
C	-1.246764	-0.103583	-1.427113
C	-2.431637	-0.378387	-0.722315
C	-3.687371	-0.573499	-1.396573
C	-4.845707	-0.790501	-0.711274
C	-1.413312	0.26774	-2.872973
C	-1.609597	-0.675259	-3.887569
C	-1.881834	-0.271375	-5.192337
C	-1.973538	1.084377	-5.504531
C	-1.78951	2.033185	-4.500959
C	-1.51482	1.626437	-3.197005
H	-3.706663	-0.555988	-2.476286
H	-5.772252	-0.9516	-1.251011
H	-1.541614	-1.731119	-3.653558
H	-2.021997	-1.017698	-5.966467
H	-2.189346	1.397283	-6.520023
H	-1.866484	3.090639	-4.729875
H	-1.385537	2.368107	-2.416154
C	1.246764	0.103583	-1.427113
C	2.431637	0.378387	-0.722315
C	3.687371	0.573499	-1.396573

C	4.845707	0.790501	-0.711274
C	1.413312	-0.26774	-2.872973
C	1.609597	0.675259	-3.887569
C	1.881834	0.271375	-5.192337
C	1.973538	-1.084377	-5.504531
C	1.78951	-2.033185	-4.500959
C	1.51482	-1.626437	-3.197005
H	3.706663	0.555988	-2.476286
H	5.772252	0.9516	-1.251011
H	1.541614	1.731119	-3.653558
H	2.021997	1.017698	-5.966467
H	2.189346	-1.397283	-6.520023
H	1.866484	-3.090639	-4.729875
H	1.385537	-2.368107	-2.416154

Table A.3: Optimized geometry of rubrene anion.

Atom	X	Y	Z
C	0	0	0.737126
C	1.247514	0.094931	1.42089
C	2.450071	0.408771	0.721439
C	3.690272	0.631481	1.3874
C	4.86427	0.873315	0.70315
C	1.400257	-0.347852	2.844269
C	1.69172	0.521559	3.904526
C	1.927381	0.040781	5.190886
C	1.882566	-1.328282	5.450605
C	1.597194	-2.209349	4.407985
C	1.361399	-1.722399	3.124372
H	3.714825	0.605833	2.467962
H	5.78391	1.048369	1.252885
H	1.719282	1.588674	3.716679
H	2.138937	0.738973	5.994563
H	2.065867	-1.703102	6.452404
H	1.563592	-3.278752	4.59284
H	1.148189	-2.411615	2.314509
C	-1.247514	-0.094931	1.42089
C	-2.450071	-0.408771	0.721439
C	-3.690272	-0.631481	1.3874

C	-4.86427	-0.873315	0.70315
C	-1.400257	0.347852	2.844269
C	-1.69172	-0.521559	3.904526
C	-1.927381	-0.040781	5.190886
C	-1.882566	1.328282	5.450605
C	-1.597194	2.209349	4.407985
C	-1.361399	1.722399	3.124372
H	-3.714825	-0.605833	2.467962
H	-5.78391	-1.048369	1.252885
H	-1.719282	-1.588674	3.716679
H	-2.138937	-0.738973	5.994563
H	-2.065867	1.703102	6.452404
H	-1.563592	3.278752	4.59284
H	-1.148189	2.411615	2.314509
C	0	0	-0.737126
C	-1.247514	-0.094931	-1.42089
C	-2.450071	-0.408771	-0.721439
C	-3.690272	-0.631481	-1.3874
C	-4.86427	-0.873315	-0.70315
C	-1.400257	0.347852	-2.844269
C	-1.69172	-0.521559	-3.904526
C	-1.927381	-0.040781	-5.190886
C	-1.882566	1.328282	-5.450605
C	-1.597194	2.209349	-4.407985
C	-1.361399	1.722399	-3.124372
H	-3.714825	-0.605833	-2.467962
H	-5.78391	-1.048369	-1.252885
H	-1.719282	-1.588674	-3.716679
H	-2.138937	-0.738973	-5.994563
H	-2.065867	1.703102	-6.452404
H	-1.563592	3.278752	-4.59284
H	-1.148189	2.411615	-2.314509
C	1.247514	0.094931	-1.42089
C	2.450071	0.408771	-0.721439
C	3.690272	0.631481	-1.3874
C	4.86427	0.873315	-0.70315
C	1.400257	-0.347852	-2.844269
C	1.69172	0.521559	-3.904526
C	1.927381	0.040781	-5.190886

C	1.882566	-1.328282	-5.450605
C	1.597194	-2.209349	-4.407985
C	1.361399	-1.722399	-3.124372
H	3.714825	0.605833	-2.467962
H	5.78391	1.048369	-1.252885
H	1.719282	1.588674	-3.716679
H	2.138937	0.738973	-5.994563
H	2.065867	-1.703102	-6.452404
H	1.563592	-3.278752	-4.59284
H	1.148189	-2.411615	-2.314509

Table A.4: Optimized geometry of rubrene cation.

Atom	X	Y	Z
C	0	0	0.735228
C	1.241161	0.084971	1.430868
C	2.437196	0.386799	0.718565
C	3.670829	0.598740	1.394359
C	4.832238	0.858891	0.703752
C	1.395687	-0.326314	2.86059
C	1.683841	0.574594	3.892371
C	1.928650	0.111725	5.181906
C	1.913491	-1.256017	5.454083
C	1.642185	-2.160079	4.42996
C	1.380541	-1.699099	3.141884
H	3.695755	0.557730	2.472865
H	5.752641	1.039110	1.246306
H	1.696388	1.639267	3.691015
H	2.133924	0.821111	5.975148
H	2.114966	-1.613163	6.457179
H	1.637712	-3.225482	4.62968
H	1.180507	-2.40892	2.346739
C	-1.241161	-0.084971	1.430868
C	-2.437196	-0.386799	0.718565
C	-3.670829	-0.59874	1.394359
C	-4.832238	-0.858891	0.703752
C	-1.395687	0.326314	2.86059
C	-1.683841	-0.574594	3.892371
C	-1.92865	-0.111725	5.181906

C	-1.913491	1.256017	5.454083
C	-1.642185	2.160079	4.42996
C	-1.380541	1.699099	3.141884
H	-3.695755	-0.55773	2.472865
H	-5.752641	-1.03911	1.246306
H	-1.696388	-1.639267	3.691015
H	-2.133924	-0.821111	5.975148
H	-2.114966	1.613163	6.457179
H	-1.637712	3.225482	4.62968
H	-1.180507	2.408920	2.346739
C	0.000000	0.000000	-0.735228
C	-1.241161	-0.084971	-1.430868
C	-2.437196	-0.386799	-0.718565
C	-3.670829	-0.59874	-1.394359
C	-4.832238	-0.858891	-0.703752
C	-1.395687	0.326314	-2.86059
C	-1.683841	-0.574594	-3.892371
C	-1.92865	-0.111725	-5.181906
C	-1.913491	1.256017	-5.454083
C	-1.642185	2.160079	-4.42996
C	-1.380541	1.699099	-3.141884
H	-3.695755	-0.55773	-2.472865
H	-5.752641	-1.03911	-1.246306
H	-1.696388	-1.639267	-3.691015
H	-2.133924	-0.821111	-5.975148
H	-2.114966	1.613163	-6.457179
H	-1.637712	3.225482	-4.62968
H	-1.180507	2.408920	-2.346739
C	1.241161	0.084971	-1.430868
C	2.437196	0.386799	-0.718565
C	3.670829	0.598740	-1.394359
C	4.832238	0.858891	-0.703752
C	1.395687	-0.326314	-2.86059
C	1.683841	0.574594	-3.892371
C	1.928650	0.111725	-5.181906
C	1.913491	-1.256017	-5.454083
C	1.642185	-2.160079	-4.42996
C	1.380541	-1.699099	-3.141884
H	3.695755	0.557730	-2.472865

H	5.752641	1.039110	-1.246306
H	1.696388	1.639267	-3.691015
H	2.133924	0.821111	-5.975148
H	2.114966	-1.613163	-6.457179
H	1.637712	-3.225482	-4.62968
H	1.180507	-2.40892	-2.346739

Appendix B

Supporting Information for Chapter 4: Femtosecond Stimulated Raman Spectroscopy - Guided Screening Leads to Efficient Singlet Fission in Rubrene Derivatives

B.1 Absorption Spectral Profile

We obtained the absorption spectra of rubrene, FM-rubrene and F-rubrene crystals using UV2600 UV-Vis spectrophotometer by Shimadzu in transmission mode. We plot the normalized steady-state absorption spectra of crystalline rubrene, FM-rubrene and F-rubrene along with the respective crystal image as seen under the microscope for our FSRS studies in Figure B.1. The absorption spectrum of a rubrene single crystal shows four absorbance maximum at 438, 464, 497 and 536 nm, FM-rubrene single crystal shows the absorbance maxima at 442, 468, 500 and 560 nm and F-rubrene crystal peaks at 466, 510, 531 and 557 nm.

The poor resolution of the peaks in F-rubrene crystal is due to the smaller crystallite size. The estimated crystal thickness of rubrene is $\sim$ 1–2 µm, FM-rubrene and F-rubrene are $\sim$ 30–40 µm.

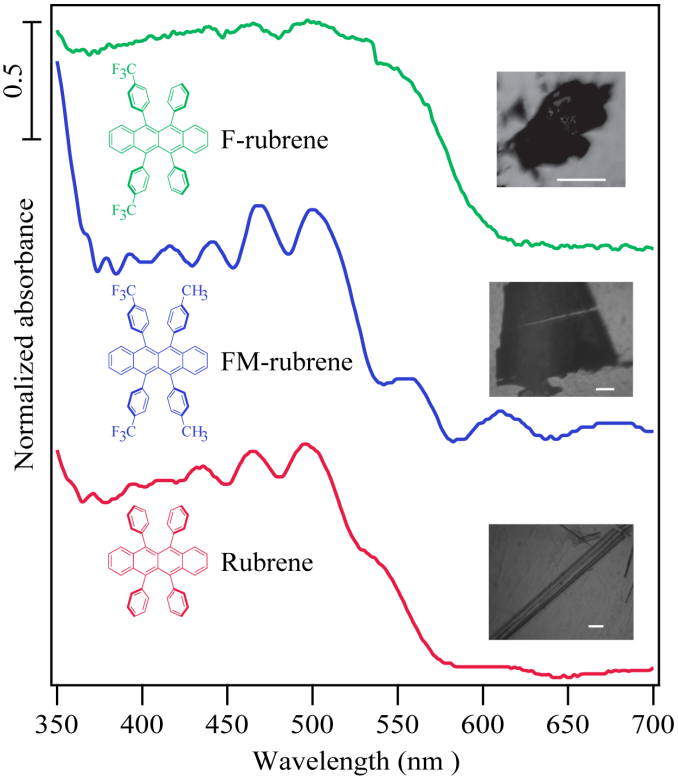

Figure B.1: Molecular structure and the respective crystals of rubrene, FM-rubrene and F-rubrene along with their absorption spectrum. Scale bar is 0.2 mm.

B.2 Actinic pulse profile

We tuned the actinic pump pulse to have a central frequency of 536 nm to collect FSR data for rubrene and 533 nm for FM-rubrene and F-rubrene crystals and plot the spectral profile in Figure B.2.

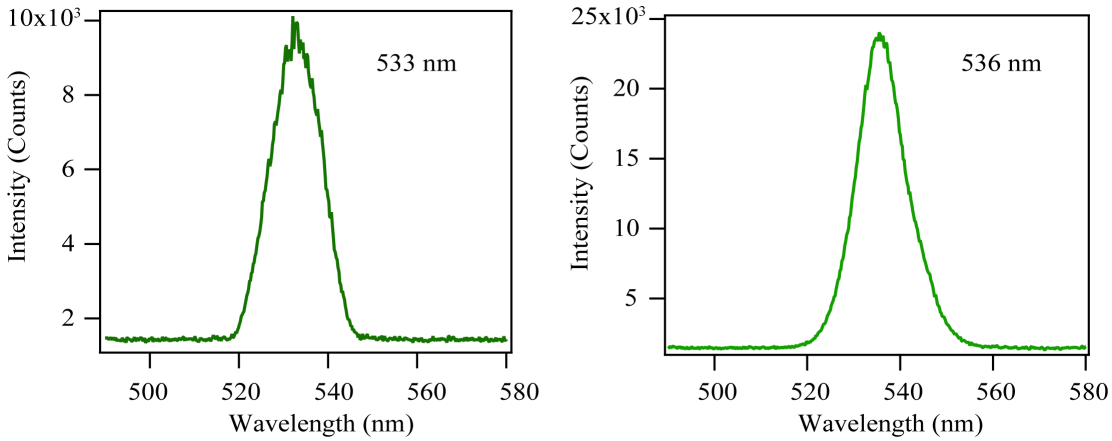

Figure B.2: Spectral profile of the actinic pump pulses used to carry out the FSR experiments. We used the 533 nm as the central frequency of the actinic pump pulse with a FWHM of 10 nm to collect time-resolved data in FM-rubrene and F-rubrene crystals, and 536 nm with a FWHM of 14 nm for crystalline rubrene.

B.3 Raw FSR data of crystalline rubrene, FM-rubrene and F-rubrene

We plot the FSR data after one-to-one subtraction of excited state spectra from the ground state spectrum of crystalline rubrene, FM-rubrene and F-rubrene in Figure B.3. We used a grating filter to generate the Raman pump pulse for the FSR experiments in crystalline rubrene [48] and an etalon to generate the Raman pump pulse for FM-rubrene and F-rubrene FSR experiments. The ground state Raman spectra of rubrene, FM-rubrene and F-rubrene has peaks at 1204, 1304, 1430 and 1541 cm^{-1}. After photoexcitation, we observe ground state bleaching features for all the Raman modes due to decreased population of the ground singlet state, S_0.

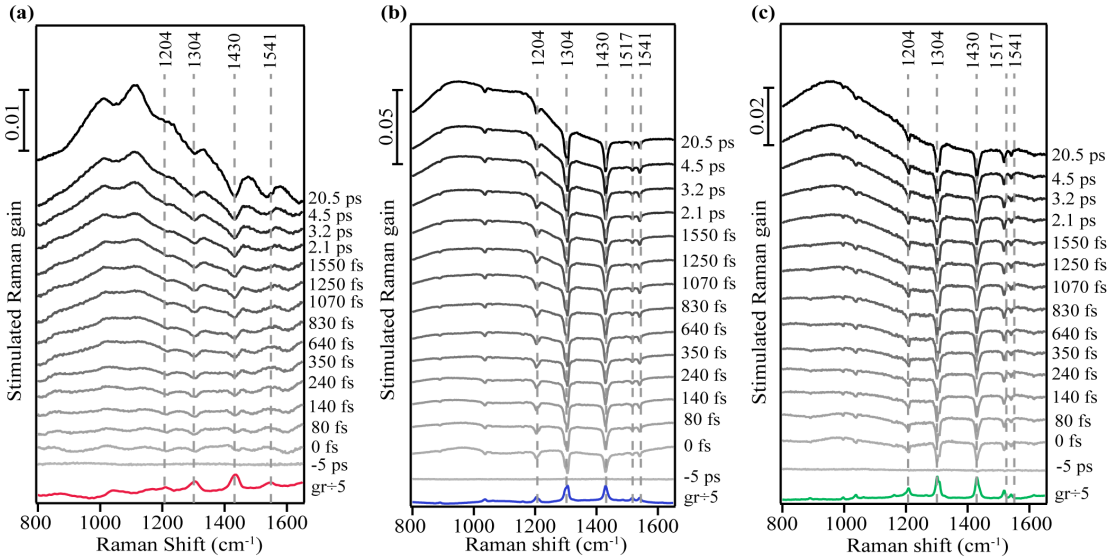

Figure B.3: Raw FSR data of crystalline (a) rubrene (b) FM-rubrene and (c) F-rubrene at various time delays after photoexcitation. The dashed lines represent the ground state Raman modes in the three molecules.

B.4 Kinetics of ground state addition

The large depletion of the ground state peaks in the excited state spectra after photoexcitation necessitated the addition of ground state spectra to examine the dynamics in the excited states. We added a fraction of ground state back into the excited state spectra until no bleaching features were present. We present the spectra obtained after adding back the ground state to the excited state spectra for the three rubrene analogues in Figure 4.2 of the main text. We plot the kinetics of the percentage of the ground state added back to excited state spectra in Figure B.4 which is the same as the kinetics of the ground state depletion.

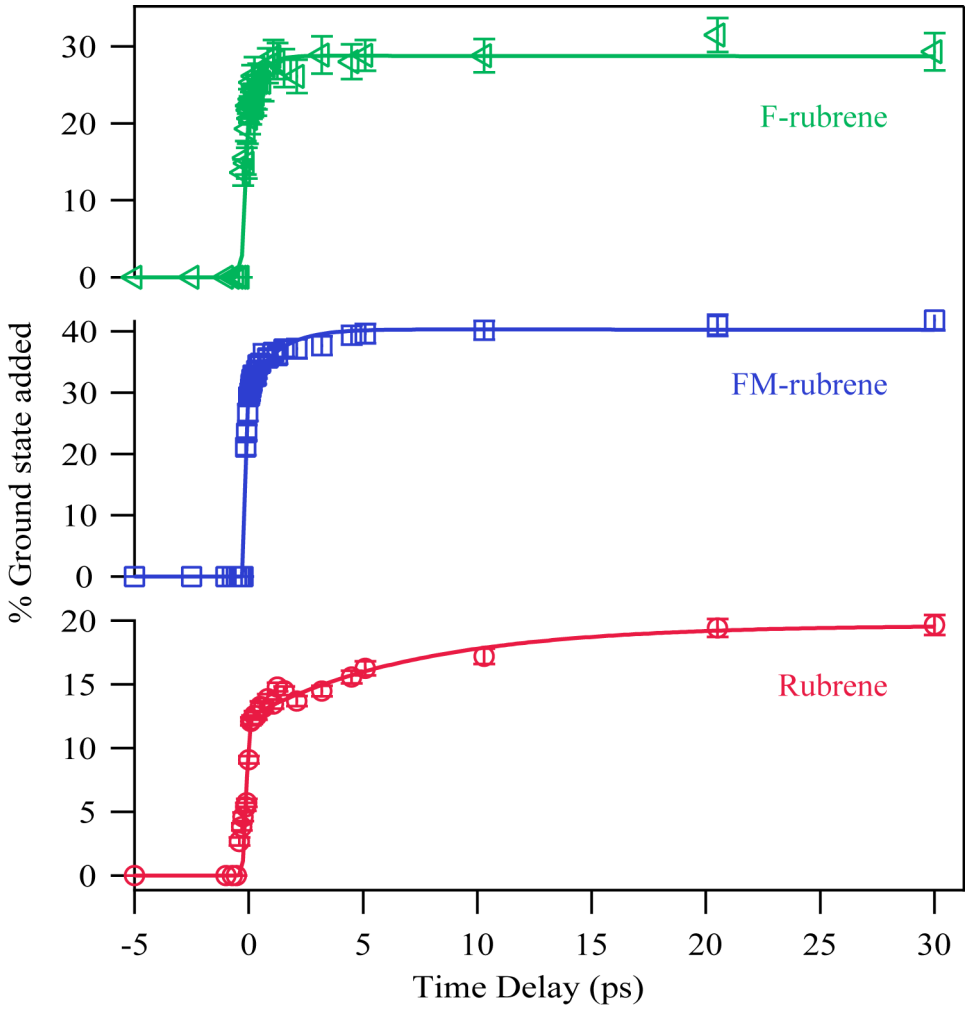

Figure B.4: Time resolved kinetics of percentage of ground state spectra added to excited state spectra at different time delays with corresponding exponential fits for rubrene, FM-rubrene and F-rubrene FSR data.

B.5 FSR data of crystalline FM-rubrene with a grating filter

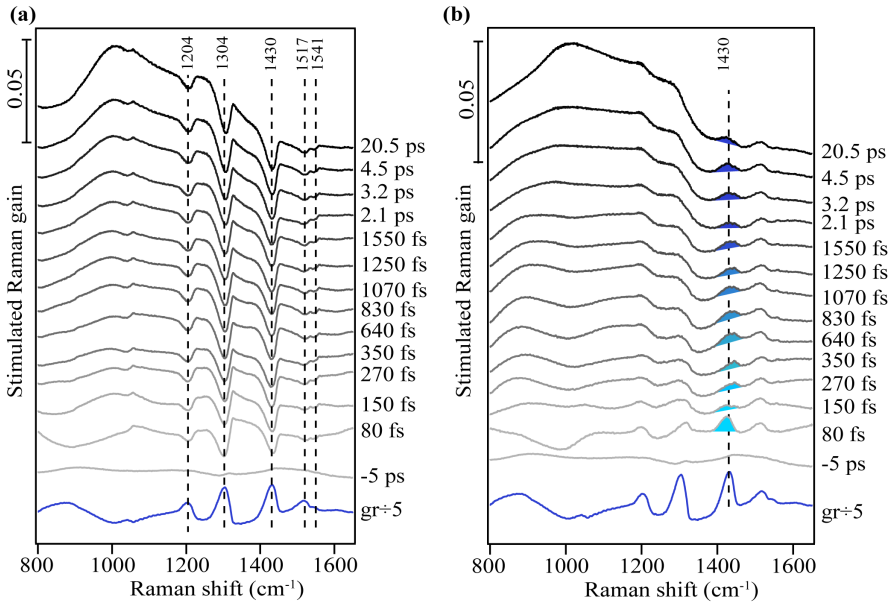

Figure B.5: (a) Raw FSR data of FM-rubrene collected with Raman pump pulses generated with a grating filter as the Raman pump source. (b) Corresponding FSR data after adding back fraction of ground state spectrum to the excited state spectra to remove any ground state bleaching features. The shaded region indicates the excited state Raman feature (blue).

We used a grating filter setup to collect the FSR data of rubrene and an etalon for the FSR data of FM-rubrene and F-rubrene presented in Figure 4.2 of main text. To validate that the dynamics after photoexcitation remains unchanged irrespective of the Raman pump generation method, we obtained time-resolved FSR data of FM-rubrene using a grating filter. We present the raw FSR data of FM-rubrene using the grating filter in Figure B.5a and the FSR spectra obtained after adding partial ground state spectra to the excited state spectra in Figure

B.5b. We present the kinetics of the amount of ground state spectra added back to excited state spectra which is nothing but the dynamics of the ground state depletion in Figure B.6. As a proof, the dynamics remain unchanged between using a grating filter and an etalon to generate the Raman pump pulses.

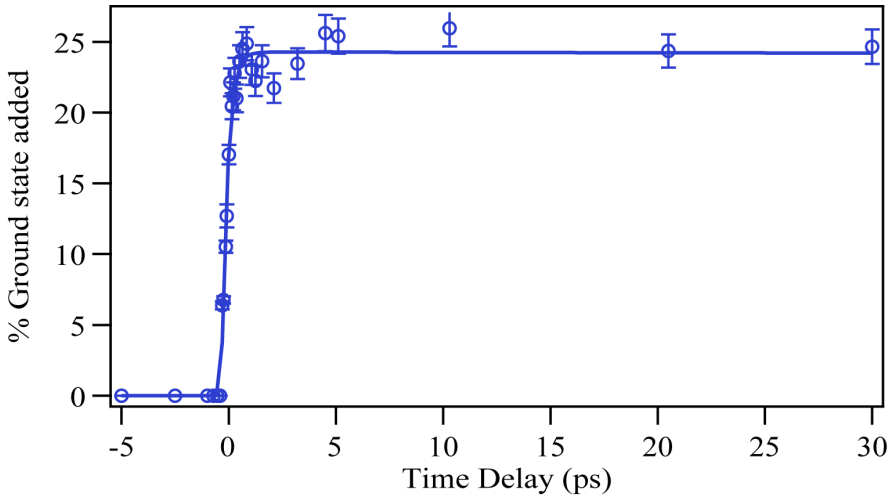

Figure B.6: Time resolved kinetics of percentage of ground state spectra added to excited state spectra at different time delays with exponential fit for FM-rubrene (blue) FSR data collected with Raman pump generated using a grating filter.

To further confirm that the spectral evolution of the 1430 cm^{-1} mode remains unchanged between using an etalon and a grating filter to generate Raman pump pulses, we plot the dynamics of the Raman frequency shift of the 1430 cm^{-1} mode from Figure B.5b with its corresponding exponential fit in Figure B.7. The exponential fit gives a time constant of 140 $\pm$ 30 fs for the frequency shift of the 1430 cm^{-1} mode here using the grating filter, which is in agreement with the time constant of 150 $\pm$ 20 fs obtained with an etalon in the main text.

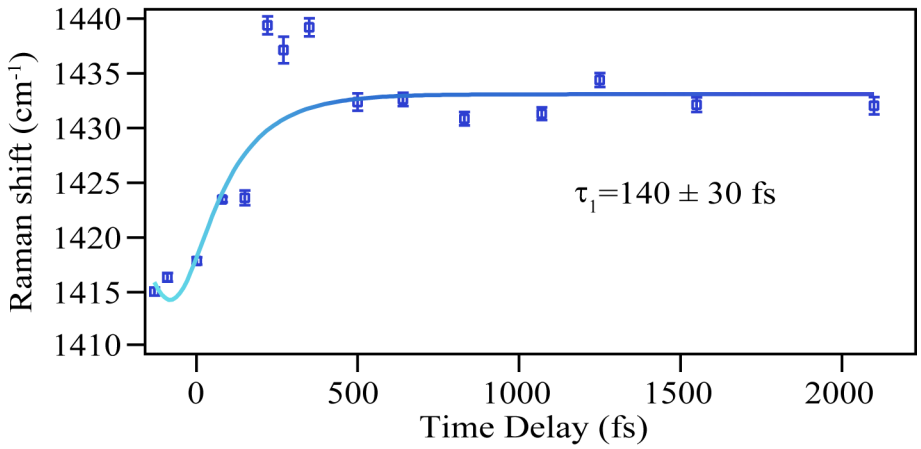

Figure B.7: Transient evolution of the Raman mode around 1430 cm^{-1} in FM-rubrene using a grating filter as the Raman pump pulse generation source.

B.6 Transient absorption in crystalline rubrene, FM-rubrene and F-rubrene

We plot the transient absorption (TA) spectra, which is in the presence of only the actinic pulse and Raman probe pulse, of rubrene, FM-rubrene and F-rubrene in Figure B.8. We observe strong intense positive features below 900 nm in all three molecules, which is indicative of excited state absorption. These features are very long-lived, on the order of the lifetimes of triplet states. The broad features below 1200 cm^{-1} in our FSRS data match those intense features here from the transient absorption by the excited state species.

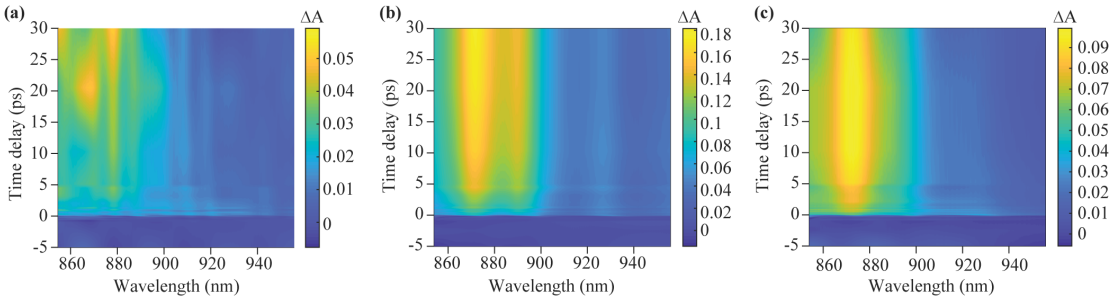

Figure B.8: Transient absorption data in crystalline (a) rubrene (b) FM-rubrene and (c) F-rubrene. The intense positive peaks below 900 nm indicate the presence of excited state absorption features.

B.7 Transient absorption of FM-rubrene solution in chloroform

In order to verify the assignment of the TA features observed in crystalline FM-rubrene, we collected the TA data of solution FM-rubrene. We plot the TA spectra of FM-rubrene in chloroform and crystal form in Figure B.9a and B.9b respectively. Comparing the TA of FM-rubrene in solution and crystal, we notice that the strong long-lived peaks at around 875 nm and 892 nm in crystal are absent in the solution data. This confirms that the strong positive peaks present in the TA data of crystalline FM-rubrene is due to absorption by the excited states which are not accessible in solution FM-rubrene, and the peaks correspond to the long-lived triplet states formed through singlet fission. The absence of positive features in solution TA data and the long lifetime of the intense positive features in crystalline FM-rubrene is a strong evidence for FM-rubrene to undergo singlet fission in crystal form, similar to that observed in rubrene. [71]

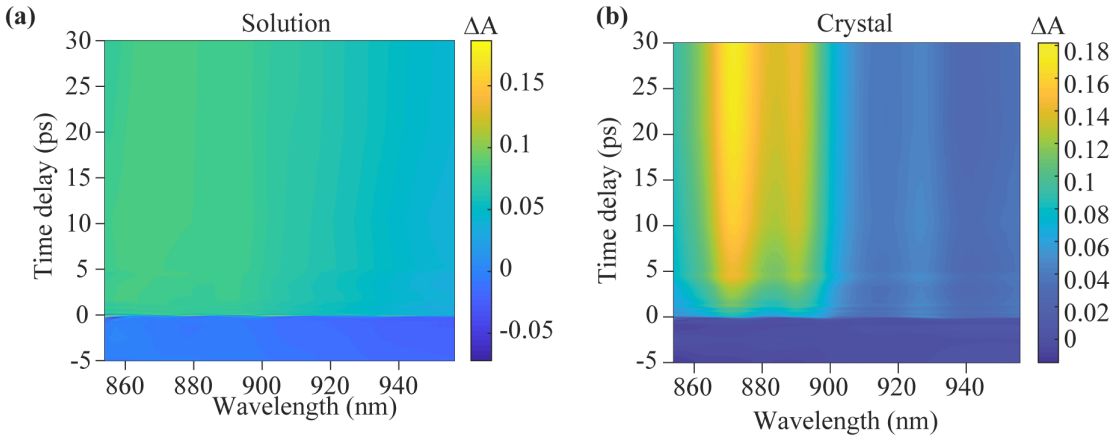

Figure B.9: Transient absorption spectra of (a) FM-rubrene solution in chloroform and (b) crystal. The absence of the intense positive features in the FM-rubrene solution data indicates that there is no absorption from excited states which are in resonance with our probing system.

B.8 Kinetic fit of the broad features in rubrene, FM-rubrene and F-rubrene

The broad features below 1200 cm^{-1} in FSRS data in Figure 2 are electronic features from the transient absorption by the separated triplet states. We fit the amplitude of the broad features to a Gaussian wavefunction and fit the amplitudes to a biexponential function to obtain the kinetics in Figure B.10. The broad features below the 1200 cm^{-1} region grows in on a timescale of 9.9 $\pm$ 0.8 ps in rubrene, 4.9 ps $\pm$ 0.4 ps in FM-rubrene and 4.6 $\pm$ 0.4 ps in F-rubrene. A second time constant of tens of nanoseconds, corresponding to the triplet lifetime, was held constant to fit the amplitude dynamics of these features. These transient absorption signatures of the separated triplet states demonstrate that the separated triplets are formed faster in F-rubrene, followed by FM-rubrene and rubrene.

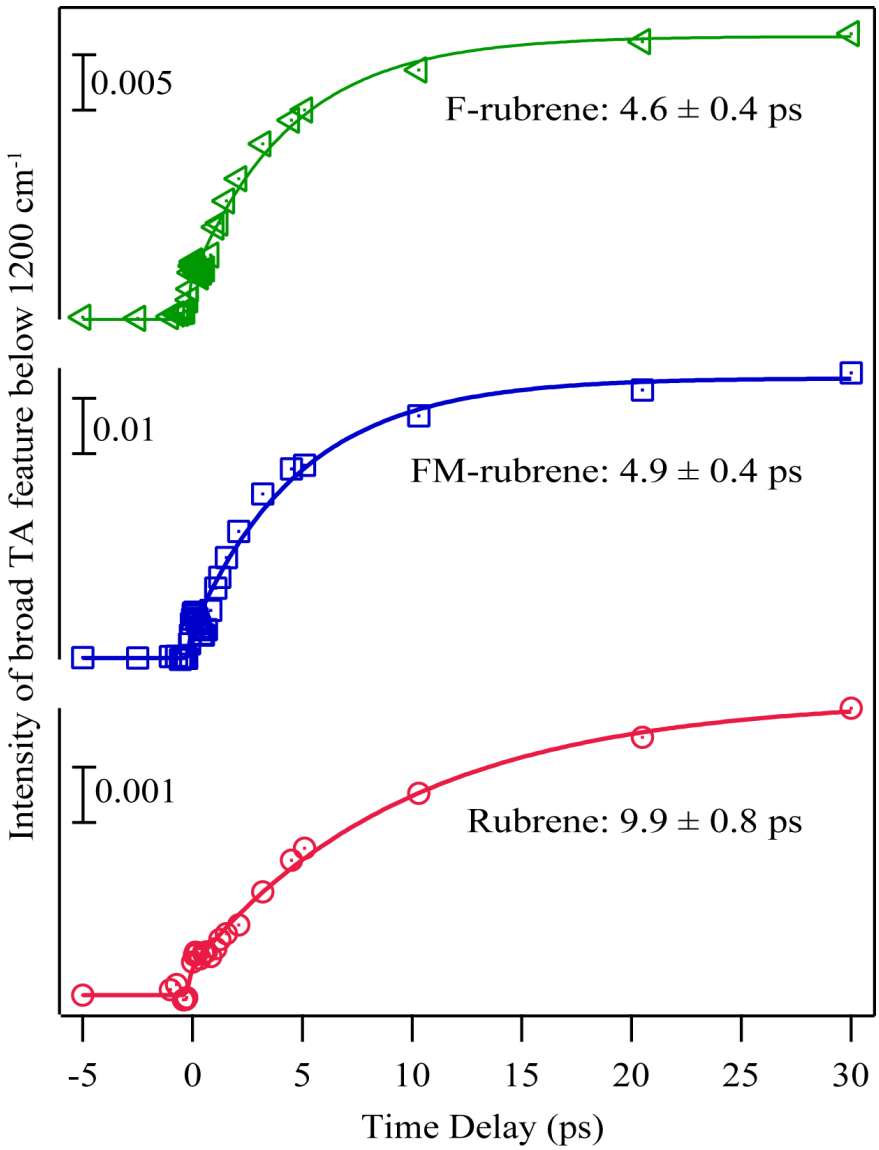

Figure B.10: Amplitude kinetics of the broad features below 1200 cm^{-1} in rubrene, FM-rubrene and F-rubrene FSRS data arising from transient absorption of the excited states.

B.9 Kinetic fits of experimental frequency shifts in FM-rubrene

The time constants (τ_1) associated with the kinetic fits for FM-rubrene and F-rubrene in Figure 3.3a is 150 ± 20 fs and less than 120 ± 40 fs, respectively. Given our instrument response function is 120 ± 3 fs, the kinetic fits are approaching the instrument response function and thus the errors in the time constants become significant. To demonstrate the sensitivity of the overall fit for the completion of the frequency shift on the time constant, we present five fits with varying time constants (110, 130, 150, 170 and 190 fs) to model the dynamic frequency evolution of the 1430 cm^{-1} mode in FM-rubrene in Figure B.11. We observe the problem associated with the fit while using time constants that are outside the uncertainty of the fit presented in the main text. It is not possible to accurately model the early growth dynamics of the Raman mode around 1430 cm^{-1} with time constants that are either shorter or longer than the uncertainty window in 150 ± 20 fs. This demonstrates that the errors associated with the time constants are significant and reliable. The time constants obtained with F-rubrene is much faster than the instrument response function of our experiments, and we have thus considered the instrument response function as the upper bound for the time constant in F-rubrene as mentioned in the main text.

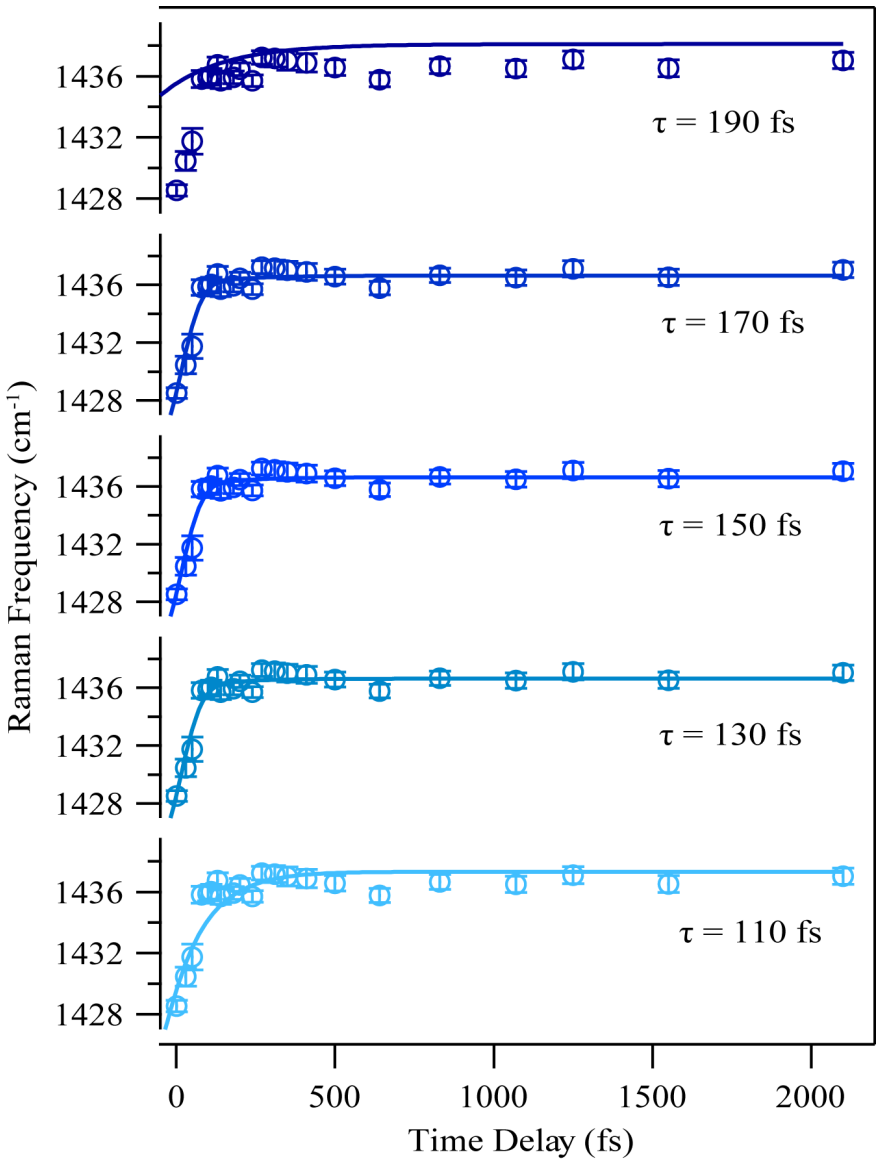

Figure B.11: Best possible fits with time constants 110, 130, 150, 170 and 190 fs for the transient frequency shift of the 1430 cm^{-1} mode.

Appendix C

Supporting Information for Chapter 5: Facile Background Discrimination in Femtosecond Stimulated Raman Spectroscopy using a Dual Frequency Raman Pump Technique

C.1 Reconstruction Methods

We present various methods that we have used for reconstruction of the difference spectrum of cyclohexane.

Here we define the Raman spectra obtained at two frequencies of the Raman pump excitations as R_1 and R_2, and the difference spectra $D_1 = R_1 - R_2$ and $D_2 = R_2 - R_1$.

Table C.1: Various methods and corresponding plots after reconstruction.

Method	Spectra
Stimulated Raman spectrum of cyclohexane *Asterisks* denote non-Raman peaks.	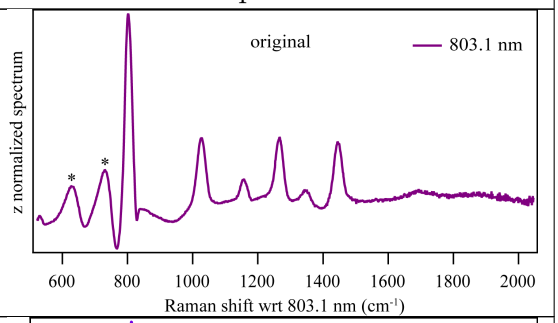
1. Reconstruction based on an established integration algorithm: [148, 154, 155] Step I: $K_{1_n} = D_{1_{n-\frac{\Delta}{2}}} + \lvert D_{1_{n+\frac{\Delta}{2}}} \rvert$ Step II: $K_{2_n} = \lvert D_{2_{n-\frac{\Delta}{2}}} \rvert + D_{2_{n+\frac{\Delta}{2}}}$ Step III: $G = K_1 + K_2$	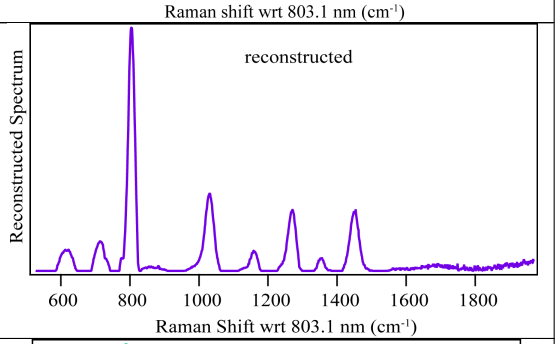
2. $G = G_{n+\Delta} - D_n$ [157]	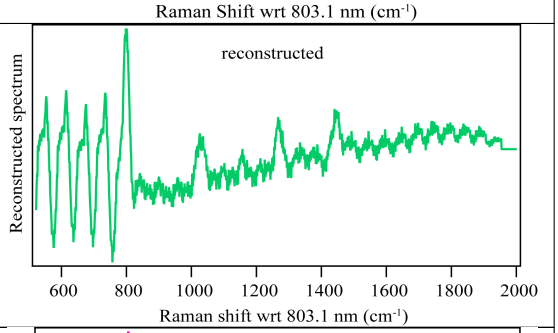
3. $G = \lvert G_{n+\Delta} \rvert - D_n$	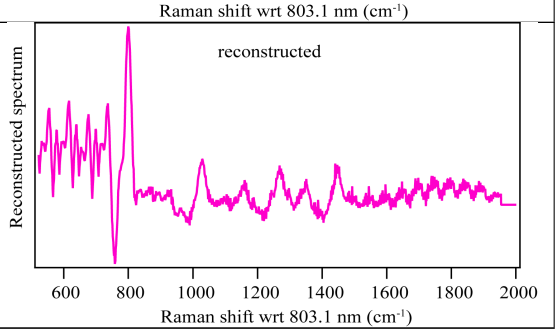

The above-mentioned algorithms use a recursion formula on the difference

spectrum, as described below. Although we are able to reconstruct the cyclohexane peaks from the difference spectrum with methods 2 and 3, the background contains considerable noise. Both methods rely on the perfect elimination of background in the difference spectrum to give a clean reconstruction. However, due to reasons explained in the main article, our obtained difference spectrum has some residual background. Due to the iterative nature of both methods, this non-zero background is propagated in the reconstruction method and results in a noisy periodic background.

C.2 Scheme of the automated reconstruction algorithm

We first subtracted the z-normalized Raman spectra from one another to obtain a difference spectrum $D(\nu)$ and plotted it with respect to the 803.1 nm Raman pump pulse (Figure C.1). If the backgrounds of the 803.1 nm and 806.1 nm Raman spectra are identical, $D(\nu)$ will eliminate the background contribution entirely and leave behind Raman peaks that appear as derivative-like features. However, we see that $D(\nu)$ still bears a non-vanishing background likely derived

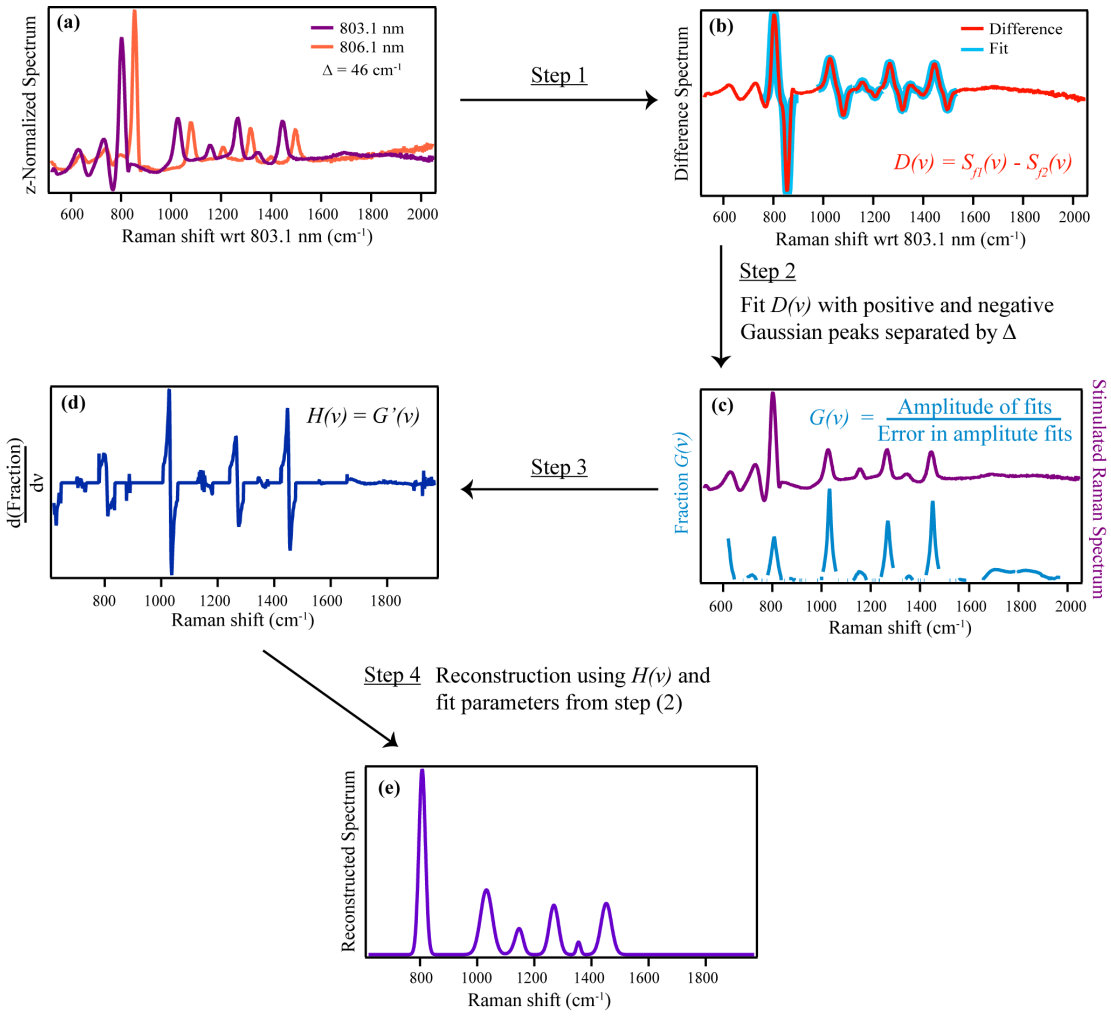

Figure C.1: Scheme of the automated reconstruction algorithm. (a) z-normalized Raman spectra of cyclohexane at Raman pump frequencies of 803.1 nm and 806.1 nm. (b) Fit the difference spectrum $D(\nu)$ to a pair of positive and negative Gaussian peaks. Examples of the fit functions (blue) at the Raman peak positions. (c) Measured the ratio of the amplitude of the fits in (b) to the error in the fits and obtained Fraction $G(\nu)$. (d) Used an algorithm to process $H(\nu)$, the derivative of $G(\nu)$, to identify the Raman peak positions. (e) Reconstructed Raman spectrum from plotting sum of Gaussian functions with the fit parameters corresponding to the peaks identified in (d).

from differences in the cross-phase modulation of the two Raman pump pulses.

Next, we fit the difference spectrum $D(\nu)$ from its i^{th} index point to its $(i+n)^{th}$ index point to a pair of Gaussian functions shifted by Δ:

$$f(\nu) = A_1 \left(\mathrm{e}^{-\frac{(\nu-\nu_0)^2}{2c^2}} - A_0 \mathrm{e}^{-\frac{(\nu-\nu_0-\Delta)^2}{2c^2}} \right) + \nu_1$$

where A_0 is the scaling factor (A_2/A_1), A_1 and A_2 are the amplitudes of the positive and negative Gaussian functions in the difference spectrum, ν is the wavenumber, ν_0 is the peak center of the positive Gaussian peak in wavenumbers, Δ is the SERDS shift, c is the standard deviation and ν_1 is the baseline. The positive and negative Gaussian peaks correspond to peaks in the 803.1 nm and 806.1 nm Raman spectra in this case.

We fit across the entire difference spectrum with $f(\nu)$ using a range of $n = 150$ points and the following constraints: 1) both the positive and negative Gaussian peaks have the same FWHM, 2) the FWHM cannot be higher than 50 cm^{-1}, 3) the peak position ν_0 is fixed at the ν value in the middle of the fitting range, and 4) A_0 and Δ values are determined from experimental conditions and held constant throughout the fit.

A_0 is set as the ratio of the output power of the two Raman pump pulses, while Δ is the difference in frequencies of the two Raman pump pulses. We chose $n = 150$ because its range covers each Raman peak function with little to no overlap with the subsequent Raman peaks in cyclohexane. In our constraints, we assumed that the FWHM of the two peaks are the same because they arise from the same cyclohexane sample under very similar experimental conditions. We set the upper limit of the FWHM to be 50 cm^{-1} because we noted that the FWHM

of the Raman peaks were less than 30 cm^{-1} in the initial Raman spectra shown in Figure C.1a. We fixed ν_0 to the center of the fitting range so that we account for all possible peak positions. As a result, we only needed to extract the amplitude A_1 and FWHM of the Raman peaks from our fitting algorithm.

After we fit the difference spectrum with $f(\nu)$, we obtained the amplitude A_1 of the fits at each point across the entire spectrum. We then divided the amplitude of the fits A_1 by its error at each point in the spectrum, which we denote as fraction $G(\nu)$ and overlaid it with the 803.1 nm Raman spectrum in Figure C.1c. Due to the constraints imposed in our fitting algorithm, we expect good fits only when ν_0 coincides with a Raman peak position. At all other positions with no Raman peaks, the fit amplitudes would have large errors and thus $G(\nu)$ approaches zero. We can see in Figure C.1c that the resulting $G(\nu)$ spikes at regions with Raman signal, very clearly highlighting the Raman peak positions. Next, we took the derivative of fraction $G(\nu)$, referred to as $H(\nu)$, shown in Figure C.1d, and ran the following algorithm to search for the exact positions of the Raman peaks. In order to be considered the position of a Raman peak, the m^{th} point of $H(\nu)$ must meet these two criteria:

(a) $H(m) > 0$ and $H(m+1) < 0$, representing a peak in $G(\nu)$ where its slope changes sign.

(b) $\sum_{m-p}^{m} H(\nu)$ is larger than a threshold value, where p is the number of points prior to the inflection point, to eliminate any oscillatory noise.

For all m that fulfilled these criteria, we retrieved the fit parameters of the difference spectrum $D(\nu)$ and computed the corresponding Gaussian functions.

The reconstructed spectrum is a sum of all of these Gaussian functions, that produces a background free spectrum. We used $p = 10$ and $threshold = 1.4$ for the automated reconstructed cyclohexane Raman spectrum in Figure 5.2d and C.1, and the choice of these parameters are discussed more in depth in the next section.

C.3 In-depth discussion about parameters used in the algorithm

Our main motivation to develop the automated reconstruction method is to improve existing reconstruction methods while minimizing any input bias and reducing residual background. Therefore, it is important that we select parameters for the automated reconstruction method based on experimental conditions or other reasonable assumptions. We discuss the choice of the values of various parameters for our reconstruction algorithm with regards to the reconstruction of crystalline betaine-30 FSR data. The reconstructed FSR spectra in Figure C.9c is with $n = 150$, $p = 10$, and $threshold = 1$.

Step 1 in our reconstruction algorithm involves calculating the difference spectrum by subtracting the two spectra obtained with different Raman pump excitations. Step 2 of our method requires fitting the difference spectrum $D(\nu)$ in a preset range with the fit function $f(\nu)$. The fit function $f(\nu)$ acts on small sections of the spectral range at a time, and then scans the entire difference spectrum. This range n has to be larger than the Raman frequency difference Δ and encompass both positive and negative Raman peaks, and preferably should not

be so large that it encroaches into the fitting range of another Raman peak. We varied this fitting spectral range and plot the reconstructed ground state data of crystalline betaine-30. From Figure C.2, we see that changing n did not change much qualitatively and we chose the n that reproduced a spectrum most similar to the raw non-background subtracted Raman spectrum. We chose the fitting window of 150 pixels for the time-resolved betaine-30 Raman data in the main text because this is the largest range that we could use without losing any spectral features from the final reconstructed data.

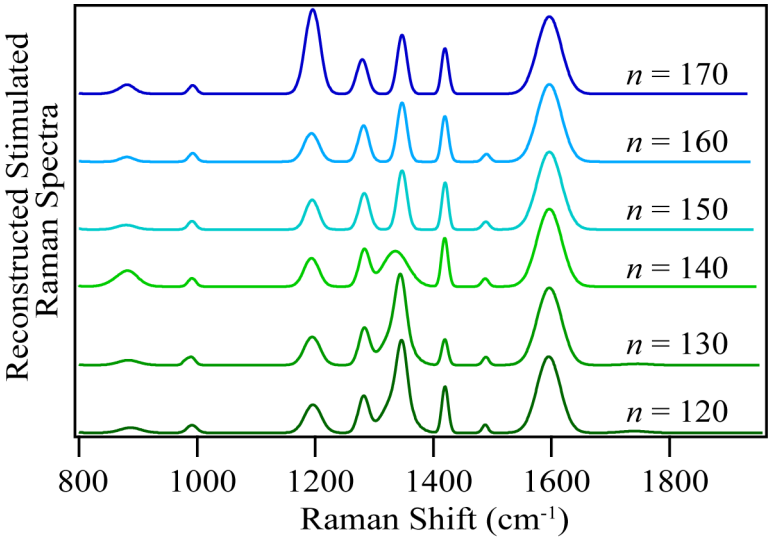

Figure C.2: Ground state stimulated Raman spectra of betaine-30 after reconstruction as a function of n for step 2 in Figure C.1.

Other inputs like the relative amplitude A_0 and frequency shift were based on the spectral profiles of the dual Raman pumps without any trial and error on our part. After we obtained the fit parameters, we used $H(\nu)$, the derivative of the fitted amplitude A_1 over its error, to identify the Raman peak positions. Qualitatively, using the fitted FWHM and its error yield similar results. However,

we chose to use the amplitude A_1 because the FWHM parameter was constrained to be less than 50 cm^{-1} and its error would also be affected if it had to be 'forced' within this constraint and not strictly due to the goodness of fit. From $H(\nu)$, we have two variables that we adjust to obtain the reconstruction spectrum. The first variable, p, is the number of points in $H(\nu)$ to be summed prior to the position of the 'peak' located. The value of p is based on the estimated peak width such that the value of p is approximately half the peak width. This ensures that the 'peak' corresponds to an actual Raman peak, where the slope of $G(\nu)$ would increase steadily before dropping off to a negative value. This would filter out oscillatory noise because the slope of $G(\nu)$ prior to this transition could be a combination of positive and negative ones. For all the reconstruction processes in this article, we have used $p = 10$. From Figure C.3, we see that once p goes above a certain value, the resulting spectrum does not vary significantly.

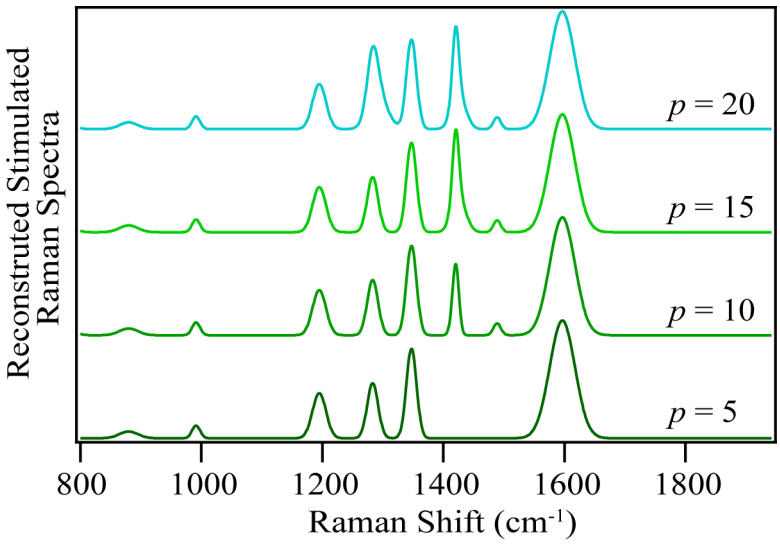

Figure C.3: Betaine-30 ground state spectra as a function of different windows for the slope addition points, p.

The second variable, *threshold*, is the minimum value the sum of p points needs be before a Raman peak is identified. Ideally, a high threshold value ensures that we are dealing with peaks, and not noise. However, using a very high threshold value might result in losing low amplitude peaks as demonstrated in Figure C.4. Therefore, a balanced value of threshold is desired between eliminating non-Raman features and retaining Raman information, which depends on the system under study.

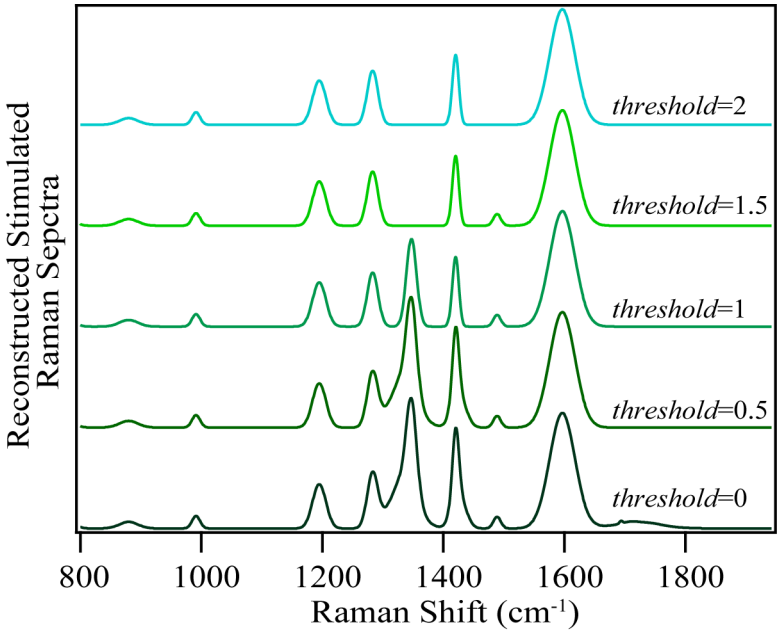

Figure C.4: Reconstructed ground state of crystalline betaine-30 as a function of *threshold* limit.

C.4 Absorption spectrum of 3,3'-diethylthiatricarbocyanine (DTTC) iodide

Figure C.5 shows the absorption spectrum of DTTC iodide in methanol. The Raman pump frequencies of 802.0 and 803.6 nm fall on the red edge of the maximum absorption peak at 758 nm in DTTC iodide.

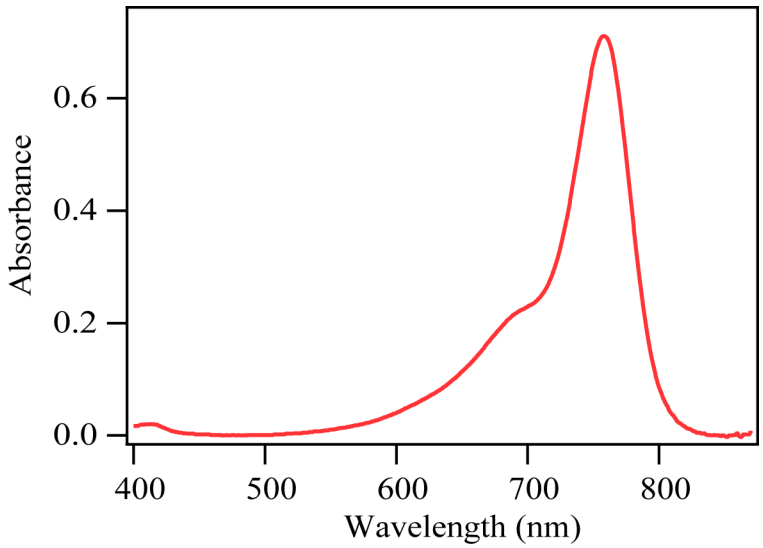

Figure C.5: Absorption spectrum of 3,3′-diethylthiatricarbocyanine (DTTC) iodide in methanol.

C.5 Reconstruction of DTTC iodide with automated algorithm

Instead of a pair of Gaussian functions, we modified $f(\nu)$ to comprise of a pair of positive and negative Fano lineshape [161] functions shifted by Δ:

$$f(\nu) = A_1 \left[\left(\frac{\left(q + \frac{\nu-\nu_0}{\Gamma/2}\right)^2}{1 + \left(\frac{\nu-\nu_0}{\Gamma/2}\right)^2} \right) - A_0 \left(\frac{\left(q + \frac{\nu-\nu_0-\Delta}{\Gamma/2}\right)^2}{1 + \left(\frac{\nu-\nu_0-\Delta}{\Gamma/2}\right)^2} \right) \right] + \nu_1$$

where A_0 is the scaling factor (A_2/A_1), A_1 and A_2 are the amplitudes of the positive and negative Fano functions in the difference spectrum, q is the Fano asymmetry parameter describing the degree to which the peaks are dispersive, ν is the wavenumber, ν_0 is the peak center of the positive Fano peak in wavenumbers, Δ is the SERDS shift (25 cm^{-1}), Γ is the line width and ν_1 is the baseline.

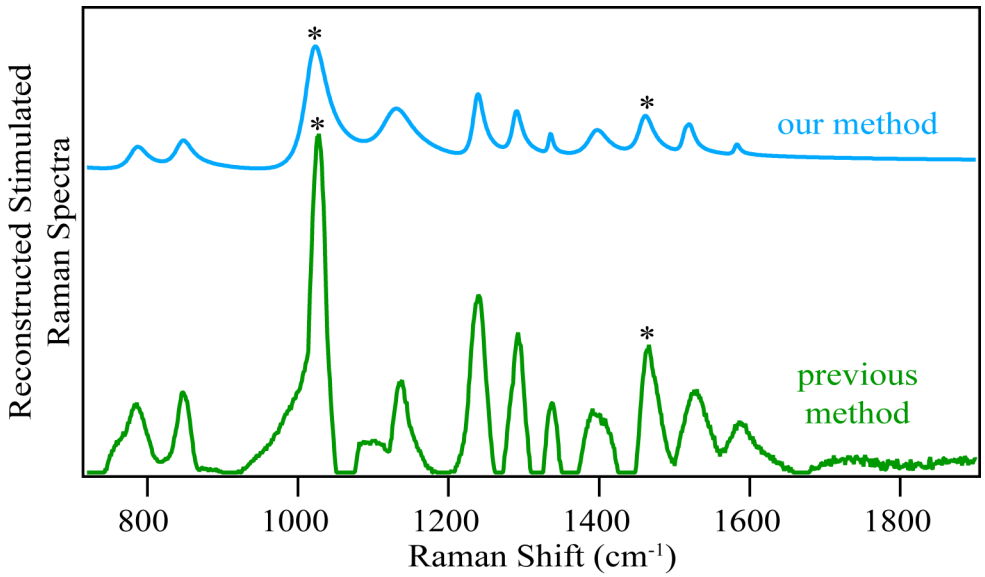

Figure C.6: Reconstructed spectra of DTTC iodide using our algorithm (blue) and with previously established algorithm mentioned in the main text (green). *Asterisks* indicate solvent peaks.

We performed all steps shown in Figure C.1 with $n = 150$, $q = 5$, $p = 10$, and $threshold = 1.4$ to remove the broad background from the Raman spectra and present the reconstructed spectrum of DTTC iodide in Figure 5.3 and Figure C.6 in blue. We held the Fano parameter $q = 5$ during the fitting because it is

representative of the dispersive nature of the Raman peaks in the raw data. This work demonstrates that our algorithm is not limited to only Gaussian lineshapes but can be extended to various lineshapes depending upon the system under study.

We also used the previously established reconstruction algorithm presented in Figure 5.2c to reconstruct the DTTC iodide Raman spectrum and plot it in green in Figure C.6. The reconstructed stimulated Raman spectra obtained from both the reconstruction algorithm are able to remove the broad background that was present in the raw stimulated Raman data. Additionally, both the algorithms are able to identify and reconstruct all the Raman peaks in the raw data set.

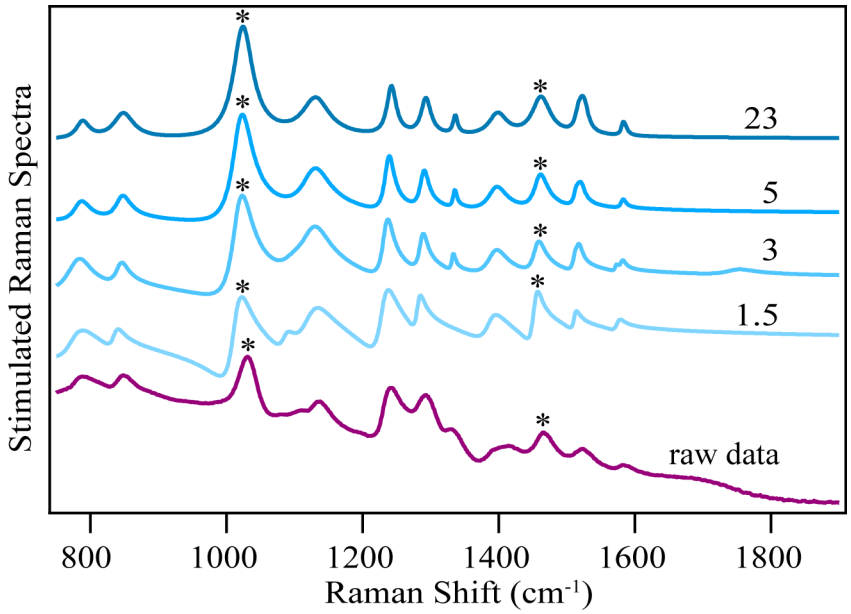

Figure C.7: Raw stimulated Raman spectrum of DTTC in iodide in plotted at the bottom. Plots in gradient of blue shows the reconstructed spectrum for the corresponding Fano parameter in $f(\nu)$. *Asterisks* indicate methanol peaks.

Figure C.7 shows the reconstructed spectra using different Fano parameters in $f(\nu)$. The reconstructed spectra with Fano parameters of 1.5 and 3 look more

dispersive than the raw DTTC iodide spectrum in the bottom panel of Figure C.7. A higher value of the Fano parameter, 23, indicates that the peaks are Lorentzian rather than dispersive. Using a value of 5 for the Fano parameter resulted in best corresponding reconstructed spectrum of the raw data and is included in Figure 5.3 in the main text.

C.6 Reconstruction of time-resolved spectra in β-carotene

Our reconstruction algorithm is written to fit all the peaks in a spectrum with the same fit function $f(\nu)$. We need different fit functions to fit different regions of the spectrum when the peaks do not have the similar properties. In order to reconstruct the bleaching features in the β-carotene time-resolved FSR data, our algorithm needs to be modified slightly compared to original as follows:

1. A_1 is less than zero

2. To identify Raman peak positions, $H(m) < 0$ and $H(m+1) > 0$, representing a peak in $G(\nu)$ where its slope changes sign.

Thus, to obtain background free Raman data, we performed the fitting algorithm twice, one with the amplitude of the fit A_1 constrained to positive values for the growing peaks while the other was constrained to have negative A_1 values for the bleaching features. We then summed the reconstructed spectra from both steps to obtain a spectrum with both positive and negative features and present it in Figure 5.4b in the main text.

C.7 Crystalline betaine-30 orientation with respect to the probe polarization

Figure C.8 shows the betaine-30 crystal under the microscope used for our FSRS studies. The crystal was orientated at an angle of $\sim 60^{\circ}$ with respect to the probe polarization.

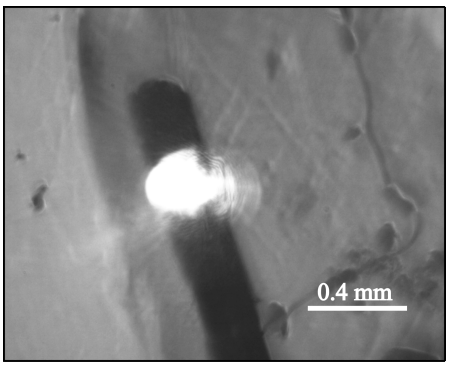

Figure C.8: Orientation of betaine-30 crystal with the probe as seen through the microscope.

C.8 FSR and reconstructed spectra of betaine-30 crystal

We used the same algorithm presented in Figure 5.2c and our newly developed automated method ($n = 150$, $p = 10$, and a *threshold* value of 1) to reconstruct the baseline free time-resolved Raman spectra of betaine-30 in Figure C.9b and C.9c, respectively. Comparing the reconstructed excited state spectra of betaine-30, we see that neither of the reconstruction methods are able to remove all non-Raman features from the raw data, but they aid in assigning vibrational peaks and

associated dynamics. Both methods still reconstructed the peaks around the 1000-1100 cm^{-1} region despite being established as non-Raman features. It is evident that the double Raman peaks around 1600 cm^{-1} in Figure C.9a are reconstructed as a single Raman peak in both Figures C.9b and C.9c. This demonstrates an inherent limitation in algorithmic reconstruction methods; when Raman features are very close in frequency or have a frequency difference of less than Δ, the algorithms are unable to resolve these peaks from one another.

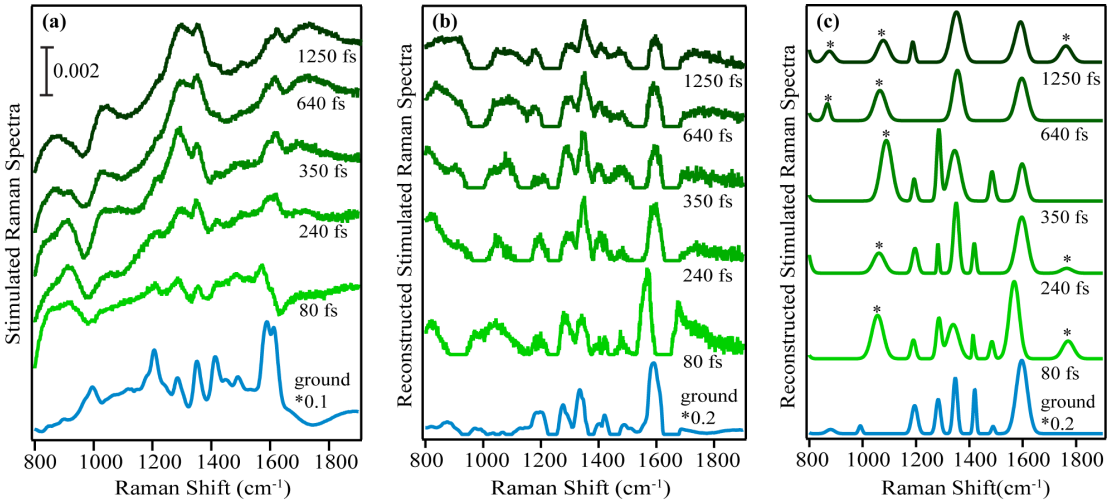

Figure C.9: (a) FSR spectra obtained with 803.1 nm Raman pump excitation of crystalline betaine-30 at various time delays after photoexcitation. The excited state spectra have broad backgrounds in addition to narrowband Raman features. (b) Reconstructed FSR spectra with previously employed reconstruction method.[148,154,155] (c) Baseline free FSR spectra of crystalline betaine-30 obtained using dual frequency Raman pump followed by our automated reconstruction method. Peaks marked with asterisks are likely non-Raman features. The ground state spectra in all 3 graphs are scaled for easier visual comparison.

We used the same algorithm presented in Figure 5.2c and our newly developed automated method ($n = 150$, $p = 10$, and a *threshold* value of 1) to reconstruct the baseline free time-resolved Raman spectra of betaine-30 in Figure C.9b and

C.9c, respectively. Comparing the reconstructed excited state spectra of betaine-30, we see that neither of the reconstruction methods are able to remove all non-Raman features from the raw data, but they aid in assigning vibrational peaks and associated dynamics. Both methods still reconstructed the peaks around the 1000 – 1100 cm^{-1} region despite being established as non-Raman features. It is evident that the double Raman peaks around 1600 cm^{-1} in Figure C.9a are reconstructed as a single Raman peak in both Figures C.9b and C.9c. This demonstrates an inherent limitation in algorithmic reconstruction methods; when Raman features are very close in frequency or have a frequency difference of less than Δ, the algorithms are unable to resolve these peaks from one another.

We notice that the reconstructed spectra in Figure C.9c has inconsistencies in the excited state between 1200 – 1600 cm^{-1}. The peak at 1200 cm^{-1} is present at all time points in Figure C.9c except for the 640 fs reconstructed spectrum. Examining the raw data in Figure C.9a and the spectra reconstructed using previously established method in Figure C.9b suggests that the 1200 cm^{-1} peak should be present at all times. Our algorithm requires setting a threshold so that the peaks must exceed a certain signal to noise ratio in order to be considered in the reconstruction algorithm. The user-defined threshold values sets the cut-off in terms of the signal to noise ratio and thus small peak magnitudes below the set threshold are not included in the algorithm, so as to avoid assigned noise features as peaks. Similarly, the peaks at 1290 cm^{-1} and 1415 cm^{-1} are present over the first 1250 fs from Figure C.9a and C.9b. However, the two peaks disappear in the 640 fs and 1250 fs reconstructed spectra in Figure C.9c. Additionally, the 1290 cm^{-1} peak abruptly narrows at 240 fs and then broadens back at subsequent time

points. These discrepancies in the spectral features between our reconstructed method and the raw and previously established reconstruction method is due to the presence of strong vibronic coupling and non-SRS features which makes the data analysis complex and difficult. We believe that the reconstructed spectra of betaine-30 in Figure C.9c has a large number of non-Raman peaks marked with asterisks. Although by changing the parameters in the algorithm we can remove the non-Raman features with our reconstruction method, we lose quite a few Raman peaks. Therefore, we used above mentioned parameters to retain all the Raman features in the excited state spectra in Figure C.9c.

This shows that while our algorithm works well for some systems, it does not work well with others and we still have to use our judgement to parse the reconstructed spectrum for Raman features. However, if we look at the dynamics of the peak around 1600 cm^{-1}, we see that both Figures C.9b and C.9c show an initial red shift followed by a blue shift within 240 fs. This observation is not as prominent in the raw spectra due to the large transient absorption background. Although both reconstruction methods are not very successful on their own, they qualitatively reproduced the same phenomenon independently. This allows us to assert with confidence the transient changes that the 1600 cm^{-1} peak undergoes after photoexcitation. Although our automated method is unable to fully remove non-Raman signatures, it is effective in background removal and complements existing methods to help us better analyze complex FSRS data.

C.9 Reconstruction of closely spaced peaks in crystalline betaine-30

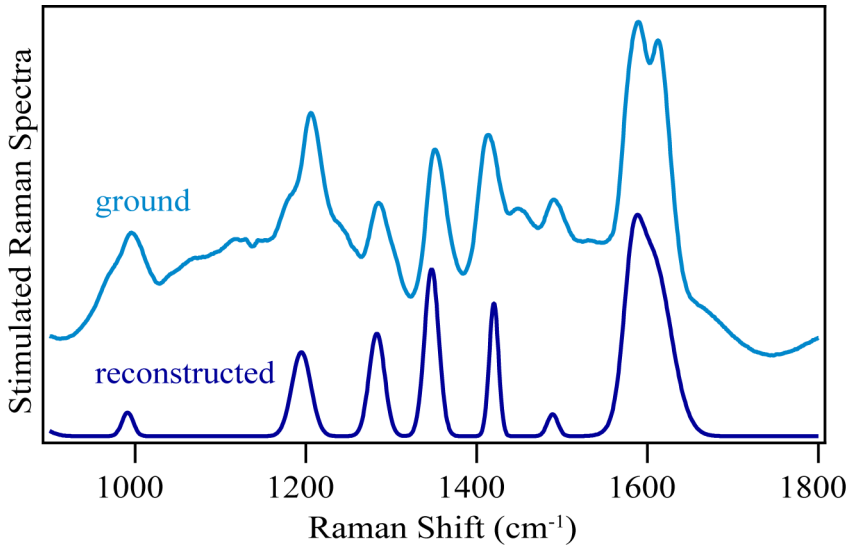

Figure C.10: Raw spectrum and reconstructed spectrum of ground state stimulated Raman spectra of crystalline betaine-30.

As mentioned in Chapter 6, we are unable to resolve the two peaks around 1600 cm^{-1} for crystalline betaine-30. When the Raman features are very close in frequency or have a frequency difference of less than Δ, the algorithms are unable to resolve these peaks from one another. As a result, the fit parameters for the mode around 1600 cm^{-1} have high errors, and the FWHM of the Raman peak in Figure C.9c is broader compared to the raw data. To obtain the two peaks around 1600 cm^{-1} in the reconstructed spectrum, we modified the fit function $f(\nu)$ such that it consisted of two pairs of positive and negative Gaussian functions instead of one. However, in order to reconstruct the double peaks $\sim$ 1600 cm^{-1} region with correct relative amplitudes between the two peaks, we held the relative

peak frequency difference between the two peaks constant. The raw ground state and the reconstructed spectrum with the aforementioned parameters of crystalline betaine-30 is in Figure C.10. Although the reconstructed spectrum has two peaks, one appearing as a shoulder over the other, we still cannot resolve them. It must be noted that this approach involves more human intervention and therefore, we have presented the time-resolved reconstructed spectra in Figure C.9c using only one pair of Gaussians for the fit function $f(\nu)$.

C.10 Polarization dependence on ground state Raman spectra of crystalline betaine-30

Crystalline betaine-30 is known to exhibit different Raman spectra with different crystal orientation and laser polarizations. We show one such example in Figure C.11 where the polarization of the two Raman pumps differ by $\sim 10^{\circ}$ due to imperfect alignment of the back reflection to the D-mirror as a result of physical constraints in the setup. The two plots are graphed with respect to their individual Raman shifts relative to their own Raman pump frequencies for comparison. The relative intensities between the peaks in the 1200 – 1600 cm^{-1} region differ with Raman pump frequency because different laser polarizations probe different sets of molecules in crystalline betaine-30. [124]

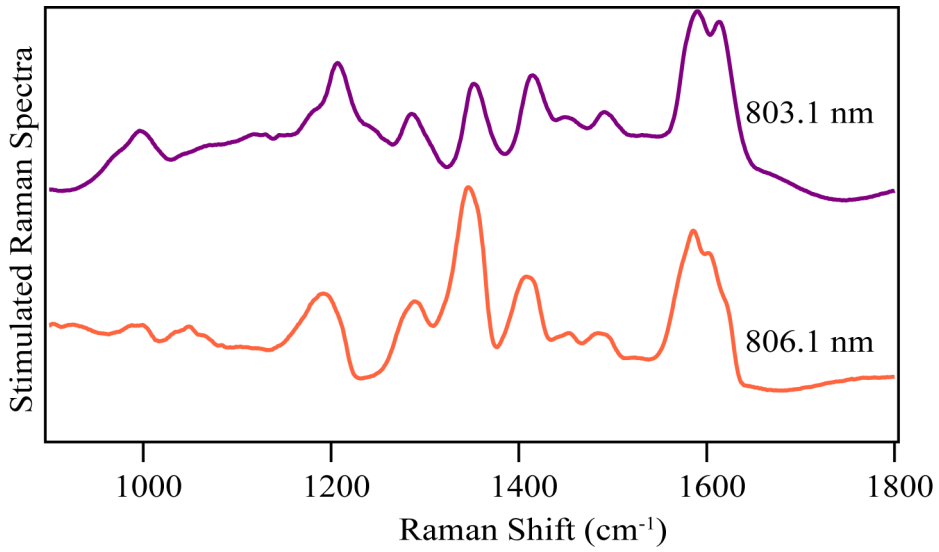

Figure C.11: Ground state stimulated Raman spectra of crystalline betaine-30 with two different Raman pump excitations. The polarization of the two Raman pumps differ by 10°. The plots in the figure are plotted with respect to their individual Raman shift axes for better comparison of relative intensities between the peaks across different excitations.

C.11 Different polarization of the two Raman pump pulses

We plot the power of the two Raman pump pulses as a function of polarization in Figure C.12. The two Raman pump pulses differ in their polarization by $\sim 10°$. This difference in the polarization could arise due to imperfect alignment of the back reflected pulses into the grating of the two Raman pump wavelengths. Thus, this difference in polarization of the two Raman pump pulses explains the discrepancy in the relative intensities in the ground state stimulated Raman spectra of betaine-30 in Figure C.11.

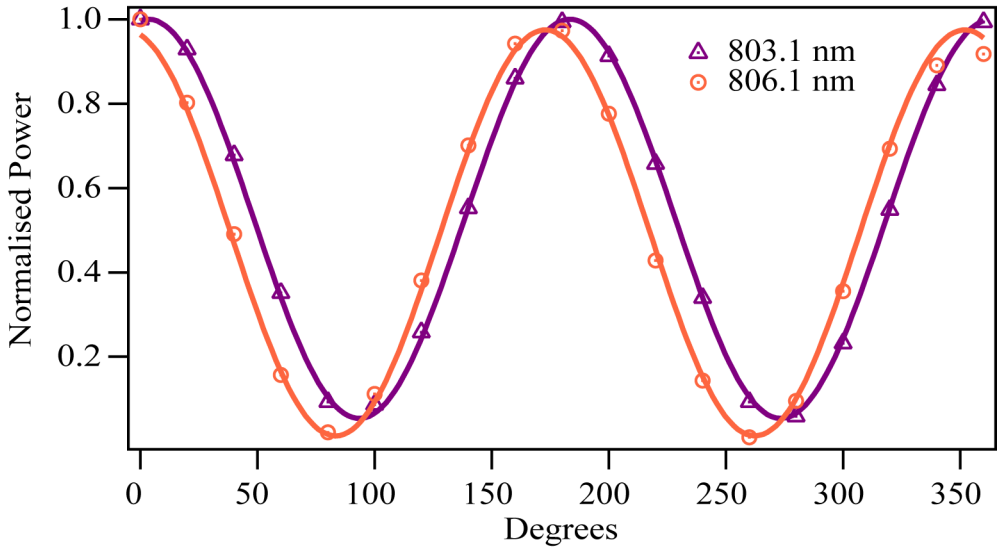

Figure C.12: Power transmission profile through an analyzer as a function of different polarizations in the two Raman pump and Raman probe pulses. The two Raman pump pulses differ in their polarizations by $\sim 10°$.